DEVELOPMENT OF OPTICAL SENSOR PLATFORMS FOR EXOSOME DETECTION

A Thesis Submitted to
the Graduate School of Engineering and Sciences of
İzmir Institute of Technology
in Partial Fulfillment of the Requirements for the Degree of

DOCTOR OF PHILOSOPHY

in Bioengineering

by
Alper Baran SÖZMEN

July 2024

İZMİR

We approve the thesis of **Alper Baran SÖZMEN**

Examining Committee Members:

Assoc. Dr. Ahu ARSLAN YILDIZ
Department of Bioengineering, İzmir Institute of Technology

Prof. Dr. Erdal BEDİR
Department of Bioengineering, İzmir Institute of Technology

Prof. Dr. Ayşe Semra KOÇTÜRK
Department of Medical Biochemistry, Dokuz Eylül University

Prof. Dr. Yasemin BAŞBINAR
Institute of Oncology, Dokuz Eylül University

Asst. Prof. Dr. Arzu UYAR
Department of Bioengineering, İzmir Institute of Technology

20 May 2024

Assoc. Prof. Dr. Ahu ARSLAN YILDIZ
Supervisor, Department of Bioengineering,
İzmir Institute of Technology

Prof. Dr. Pınar AKAN
Co-advisor, Department of Medical
Biochemistry, Dokuz Eylül
University

Assoc. Prof. Dr. Ali Oğuz BÜYÜKKİLECİ
Head of Biotechnology Department
İzmir Institute of Technology

Prof. Dr. Mehtap EANES
Dean of the Graduate School of
Engineering and Sciences

ACKNOWLEDGMENTS

First and foremost, I want to extend my heartfelt gratitude to my supervisor, Dr. Ahu Arslan Yıldız, for her unwavering guidance and mentorship throughout my PhD journey. Her support made the Bioengineering Department feel like a second home to me.

I am also deeply thankful to my thesis committee members, Semra Koçtürk and Erdal Bedir, for their perseverance and kindness over the years. A special acknowledgment goes to my co-advisor, Pınar Akan. I was also supported by TÜBİTAK Directorate of Science Fellowships and Grant Programmes 2211- National PhD Scholarship Programs during my studies for PhD, I’m grateful for this support.

To the brilliant minds in the Biomimetics Research group and the Department of Bioengineering, I owe a huge thank you. Ece Özmen and Özüm Yıldırım, your help brought magic and order to what could have been utter chaos. My gratitude also goes to Arda Pişirici, Başak Çoban, and Zeynep Altan for their camaraderie, assistance during tough times, and unwavering support. You’ve turned what could have been a grueling process into a much smoother experience. I cannot forget my friends who stood by me through this entire journey. Özge Yıldız, your endless support and knack for navigating life's twists and turns have been a true blessing. I’m ever grateful to have had you as my partner in crime, especially at the very end of this journey. To all my friends from in and out of IZTECH, your unwavering support, early Friday evenings, game nights, jam sessions, late-night pep talks, and endless laughter have kept me grounded and motivated. Your presence has been like having a trusty towel in the face of the vast unknown, making this journey not just bearable, but truly memorable. I couldn’t have asked for a better support system, and I am forever thankful for each one of you.

Finally, to my incredible family—my mom and dad, who have been my guiding lights not only in this study and college life but throughout my entire life. To my sister, whose support and love have always been a source of strength, who has always been there for me when things were impossible and until they were not. I am eternally grateful.

This thesis would not have been possible without you all. Thanks for making this story a good one.

ABSTRACT

DEVELOPMENT OF OPTICAL SENSOR PLATFORMS FOR EXOSOME DETECTION

This thesis proposes a novel approach for early detection and monitoring of cancer through utilization of optical sensor platforms for exosome detection. Current technologies for cancer prognosis, diagnosis, and monitoring face significant limitations, particularly in their efficiency at early stages and their invasiveness. In order to address these challenges, this study focuses on developing biosensor platforms for future liquid biopsy applications that are capable of detecting cancerous exosomal membrane proteins, with an emphasis on Non-Small Cell Lung Cancer (NSCLC) due to its well-defined membrane protein profile.

The research involved the fabrication, optimization, and characterization of two optical biosensor platforms utilizing localized surface plasmon resonance (LSPR) and magnetic levitation (MagLev) principles. The biosensor platforms were initially tested with a model protein, Bovine Serum Albumin (BSA); and solubilized Exosomal Membrane Proteins (ExoMPs); including EpCAM, CD151, and CD81. These ExoMPs were chosen as targets hence they are widely recognized as exosomal cancer biomarkers, exosomal NSCLC biomarkers, and exosomal biomarkers, respectively. A549 NSCLC and MRC5 healthy lung fibroblast cell lines were utilized as sources of *in-vitro* exosomes for testing the exosome detection, recognition, and quantification capabilities of the developed optical biosensor platforms. Both platforms were able to successfully distinguish cancer derived exosomes from the healthy exosomes with statistical significance.

Overall, this research contributes to advancement of cancer diagnostics and personalized medicine by providing a promising approach for early detection and monitoring through liquid biopsy techniques. The developed platforms have the potential to contribute to cancer prognosis and diagnosis with further development and investigation.

ÖZET

EKSOZOM TESPİTİ İÇİN OPTİK SENSÖR PLATFORMLARI GELİŞTİRİLMESİ

Bu tez, eksozom tespiti için optik sensör platformlarının kullanılması yoluyla kanserin erken teşhisi ve izlenmesi için yeni bir yaklaşım önermektedir. Kanser prognozu, teşhisi ve izlenmesine yönelik mevcut teknolojiler, özellikle erken evrelerdeki etkinlikleri ve invazivlikleri açısından önemli sınırlamalarla karşı karşıyadır. Bu zorlukların üstesinden gelmek için bu çalışma, iyi tanımlanmış membran protein profili nedeniyle Küçük Hücreli Dışı Akciğer Kanserine (NSCLC) vurgu yaparak, kanserli ekzozomal membran proteinlerini tespit edebilen gelecekteki sıvı biyopsi uygulamaları için biyosensör platformları geliştirmeye odaklanmaktadır.

Araştırma, lokalize yüzey plazmon rezonansı (LSPR) ve manyetik kaldırma (MagLev) prensiplerini kullanan iki optik biyosensör platformunun üretimini, optimizasyonunu ve karakterizasyonunu içermektedir. Biyosensör platformları başlangıçta bir model protein olan Bovine Serum Albumin (BSA) ve sonrasında EpCAM, CD151 ve CD81 Eksozomal Membran Proteinleri (ExoMP'ler) ile test edilmiştir. Bu Sırasıyla eksozomal kanser biyobelirteçleri, eksozomal NSCLC biyobelirteçleri ve eksozomal biyobelirteçler olarak yaygın şekilde kullanıldıkları için bu ExoMP’ler hedef olarak seçilmiştir. A549 NSCLC ve MRC5 sağlıklı akciğer fibroblast hücre hatları, geliştirilen optik biyosensör platformlarının eksozom algılama, tanıma ve miktar belirleme yeteneklerini analiz etmek için *in-vitro* eksozom kaynakları olarak kullanılmıştır. Her iki platform da kanserden türetilen eksozomları sağlıklı eksozomlardan istatistiksel anlamlılıkla başarılı bir şekilde ayırt edebilmiştir.

Genel olarak, bu araştırma, sıvı biyopsi teknikleri yoluyla erken teşhis ve izleme için umut verici bir yaklaşım sağlayarak kanser teşhisi ve kişiselleştirilmiş tıbbın ilerlemesine katkıda bulunmaktadır. Geliştirilen platformlar, daha fazla geliştirme ve araştırma ile kanser prognozu ve teşhisine katkıda bulunma potansiyeline sahiptir.

TABLE OF CONTENTS

LIST OF FIGURES

Figure **Page**

Figure **Page**

Figure **Page**

Figure **Page**

LIST OF TABLES

CHAPTER 1

INTRODUCTION

1.1 Cancer

Since the start of the 21st century, noncommunicable diseases are one of the leading causes of death in the world and cancer is the first leading cause among these diseases according to the report of World Health Organization (WHO) in 2015. Both incidence and mortality rate of cancer are increasing rapidly(Bray et al. 2018). WHO pointed out that in 2015 8.8 million people died of cancer that is one sixth of all global death in that year, the toll increased to 9.6 million in 2018(Shandilya et al. 2019). Despite high mortality rate, 40% of cancer cases are curable when diagnosed at an early stage (X. Li et al. 2019a). This motivation led field of cancer research to invest in providing the much-needed methodologies for early diagnosis of cancer. Current gold standard of cancer diagnosis is tissue biopsy which bears disadvantages; mainly inadequacy of informativeness in early stages of the disease. Also used techniques are not always applicable to all patients due to their invasiveness and the risk of trauma on cancerous tissue, which might lead to metastasis (X. Li et al. 2019b; Zarei 2017).

Diagnosis of any disease can be accomplished by detecting one or more of four indicators: biomarkers, human cells, bacteria, and viruses depending on nature of the malignancy. In specific case of cancer these can be limited to two indicators: cancerous human cells and biomarkers. The latter essentially is a broad category that includes any measurable substance, structure, or process that can be linked to the existence of a specific disease (Campbell et al. 2018; Strimbu and Tavel 2010). Biomarkers of cancer are the components that are born or derived from cancerous tissue and circulate through body; cancer cells release circulating tumor DNA (ctDNA), and extracellular vesicles (EVs) which contain proteins and nucleic acids that can be utilized to trace the origin, stage, and location of the disease (Palmirotta et al. 2018). EVs are also released by healthy cells and participate in a variety of physiological processes; but also in pathological processes such as progression of neurodegenerative diseases and inflammatory responses, invasion, metastasis, and immune suppression in cancer (Valkonen et al. 2017; Xu et al. 2018). This revealed the great potential of exosomes as disease markers, in particular, cancer biomarkers. Isolation and detection of these markers from blood or any other bodily fluid is called liquid biopsy. Liquid biopsy may hold the key to eliminate invasive procedures such as tissue biopsy and carry cancer tests to casual check-up routines (Palmirotta et al. 2018).

1.2 Exosomes

EVs range between 20 to 1000 nm in diameter, having various cellular origins and biochemical compositions. This hinders a generalized definition of EVs and also a distinct categorization, Figure 1 demonstrates the differences in synthesis of extracellular vesicles. Exosomes are a subcategory of EVs which are generally defined as membrane vesicles with endocytic origin that are between 30-100 nm in diameter (M He and Zeng 2016; van der Pol et al. 2012). They exhibit a multivesicular membrane body assembly and are released from the cell via exocytosis. Furthermore, exosomes carry codes of their parent cells, i.e. microRNA (miRNA), proteins, and DNA (Halvaei et al. 2018). Their main purpose is thought to be cell-cell communication in long distances (Cocucci and Meldolesi 2015).

Their role in initiation and progression of cancer indicates they are excellent candidates as biomarkers for cancer. A generalized detection methodology has not been designated yet due to the complexity and variation of their cargo and their release mechanisms (Barteneva et al. 2013; Jalalian et al. 2019). This variety and complexity arises from their heterogeneous nature and composition that may include any known molecular constituent of a cell. It is also not clear how the content is composed; whether is it an organized mechanism or randomly happening process. Although, there are lots of uncertainties, it is well accepted that exosome count increases in cancer patients' blood (Kalluri 2016). Moreover, they are more reliable targets as biomarkers compared to other sources such as circulating tumor cells (CTCs) or apoptotic bodies; due to developed isolation and characterization protocols, specific markers, and abundance in circulatory system.

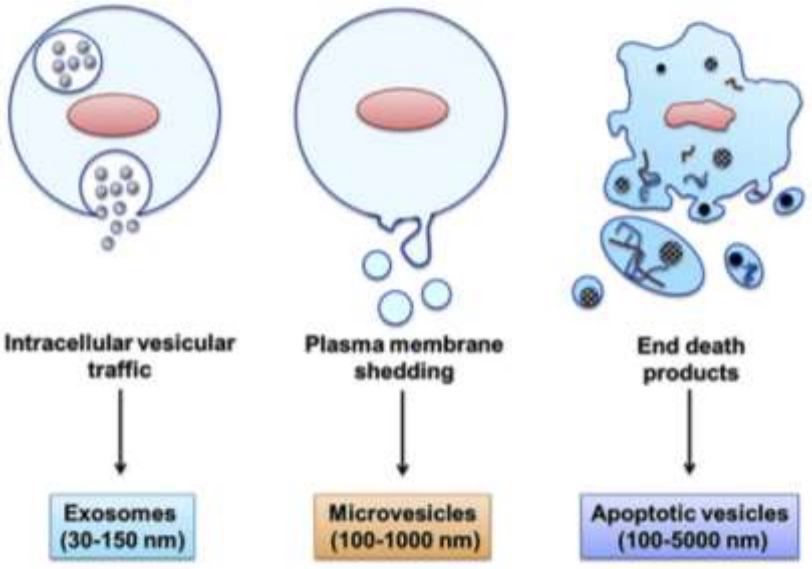

Figure 1. Cell derived extracellular vesicles(Devhare and Ray 2018).

1.2.1 Clinical Significance of Exosomes

One of the main reciprocities on utilization of exosomes is either to use them as therapeutic agents, or to target them as biomarkers of cancer. Although the decision on effectivity of each path cannot be made with current knowledge on exosomes; both ideas require a deeper understanding about the role of exosome in general, and specifically in cancer which leads to need of further studies on cancer derived exosomes (Bastos et al. 2018). Inadequacy of traditional diagnostic methods for cancer such as computed tomography, endoscopy, or tissue biopsy pushed the field to explore newly discovered diagnostic potential of exosomes. The most important challenge of developing an exosome-based cancer diagnostic methodology is isolation step. Current conventional approach in exosome isolation for further analysis is series of centrifugation, ultracentrifugation, and ultrafiltration processes (Farooqi et al. 2018; Greening et al. 2015; Mignot et al. 2006; Pavlova 2016; Perez-Callejo et al. 2016).

Exosome analyses is mostly carried out focusing on RNA and DNA fragments carried by them in recent studies on cancer diagnosis utilizing exosomes (L. Huang et al., 2015; S. H. Huang et al., 2013; Tamura & Yin, 2017; Taverna et al., 2016; Taylor & Gercel-Taylor, 2008),however this approach brings out challenges of isolation of exosomes and subsequent genetic materials (Cheng et al. 2019; Cheol Kim et al. 2017; Gholizadeh et al. 2017; Jakobsen et al. 2015; Kanwar et al. 2014; Yuki Konakade Takeshi Yanagida Noritada Kaji Yong He Masaki Kanai Kazuki Nagashima Hiroshi Yukaw2 Tomoji Kawai Yoshinobu Baba 2014; Pavlova 2016; Sandfeld-Paulsen, Aggerholm-Pedersen, et al. 2016; Sandfeld-Paulsen, Jakobsen, et al. 2016; Tamura and Yin 2017; Z. Zhao et al. 2016).

1.2.2 Exosomal Membrane Proteins as Prognostic Biomarkers in Cancer

Table 1 summarizes recent literature on exosome isolation and exosomal membrane protein detection methods used through studies and related diseases. Exosomes reflect the status of corresponding parent cell; this reflection is not only monitored via genetic material carried, but also through protein content of exosome. Hence, surface proteins of exosomes are easy to reach potential biomarkers for cancer diagnosis (W. Li et al. 2017). Tetraspanins are membrane proteins that are found in exosomes; the members of this family such as CD9, CD36 CD44, CD63, CD81, and CD151 are investigated as potential biomarkers for various types of cancer with the anticipation of enabling early diagnosis (Hemler 2005; Jalalian et al. 2019; W. Li et al. 2017; Shen et al. 2011).

The most commonly utilized cancerous exosomal membrane protein detection methodology is enzyme linked immune-sorbent assay (ELISA), Xiao et al., searched for exosomal tumor markers of colorectal cancer (CRC) via ELISA analysis where they utilized both cell culture supernatant and clinical samples. The isolation of exosomes was carried out by several steps of centrifugation, ultracentrifugation, and filtration. ELISA analysis was supplemented by Western Blot analysis concluding that CK19, TAG72, and CA125 were markers for CRC, which could be used for diagnosis and monitoring (Xiao et al. 2019).

Table 1. Studies on Exosomal Membrane Proteins; isolation and detection.

Disease	**Membrane Proteins**	**Isolation Method**	**Detection Method**	**Reference**
Colorectal Cancer	CK19, TAG72, and CA125	Ultracentrifugation and filtration	ELISA	(Xiao et al. 2019)
Colorectal Cancer	CD147	None after blood fractionation	ExoScreen, immunofluorescent assay	(Yoshioka et al. 2014)
N/A	CD9, CD63, and CD81	Centrifugation	EV Array, immunofluorescent assay	(Jorgensen et al. 2013)
Ovarian Cancer	CA-125, EpCAM, and CD24	Microfluidics	ExoSearch, microfluidic chip with integrated immunomagnetic beads	(Z. Zhao et al. 2016)
Lung Cancer	CD9, and C91	Antibody coated tips	LC/MSMS analysis	(Ueda et al. 2014)
N/A	CD63	Patterned ZnO nanowire device	Fluorescent assay, AleaxaFluor488	(Konakade et al., 2014)
Ovarian Cancer	CD24, and EPCAM	Filtration	nPLEX, nanoplasmonic sensor	(Im et al. 2014)
N/A	CD9, CD63, CD81, CD41b, and EPCAM	Filtration and immunoaffinity	SPRi	(L. Zhu et al. 2014)
NSCLC	CD151, CD146, and Tspan8	None after blood fractionation	Antibody printed epoxy-coated microarrays	(Sandfeld-Paulsen, Aggerholm-Pedersen, et al. 2016)

Another study on CRC proposed an alternative methodology to ELISA with no need of exosome isolation and lowered amount of sample. Proposed methodology is called as ExoScreen (Figure 2) by Yoshioka et al. The method essentially utilizes an immunofluorescent assay directly in the serum, where researchers prepared two types of beads; one streptavidin coated biotinylated antibodies (donor beads) and other one conjugated with second type of antibody (acceptor beads). A laser at 680 nm is used to excite the donor bead; which leads to release of a singlet oxygen, if the beads are within 200 nm of analyte, this oxygen species excites the acceptor bead emitting a signal at 615 nm. In this report anti-CD147 and anti-CD9 antibodies were used, and double positive exosomes were captured successfully with high sensitivity and without any pretreatment (Yoshioka et al., 2014).

Zhang, He, & Zeng have developed another alternative methodology to ELISA; they combined a graphene oxide/ polydopamine (GO/PDA) layer with ELISA assay to reach higher sensitivity by increasing immune-capture efficiency and eliminating non-specific exosome binding. The designed device, namely nano-IMEX chip (Figure 3); was used to successfully differentiate individuals with ovarian cancer from healthy individuals as a proof of concept (P. Zhang, He, and Zeng 2016).

The simultaneous expression of more than one membrane protein in exosomes during or prior to a disease called for a methodology that would allow multiplexed analysis. EV arrays for capturing and phenotyping exosomes were proposed in a recent study. An EV array of 21 antibodies is used to phenotype exosomes; with a cocktail of antibodies anti-CD9, anti-CD63, and antiCD81 to detect exosomes. The device has a lower detection limit of 2.4×10^4 exosomes, and it successfully detected exosomes in serum and cell supernatants. Although, only the samples from healthy individuals were tested, the researchers proposed that the methodology can be applied to diagnose diseases if relevant biomarkers are determined, details can be seen in Figure 4 (Jorgensen et al. 2013).

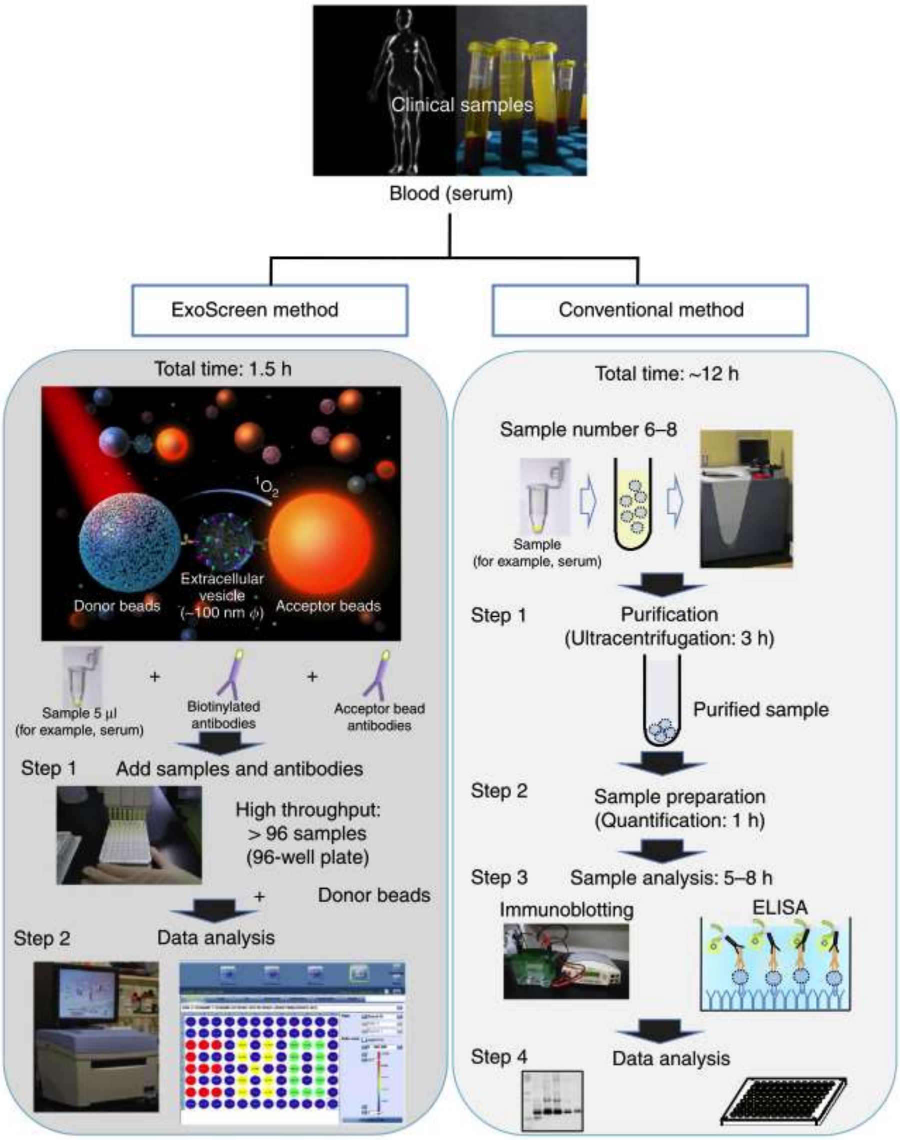

Figure 2. A comparison of conventional exosome detection methodology and the ExoSCreen method (Yoshioka et al., 2014).

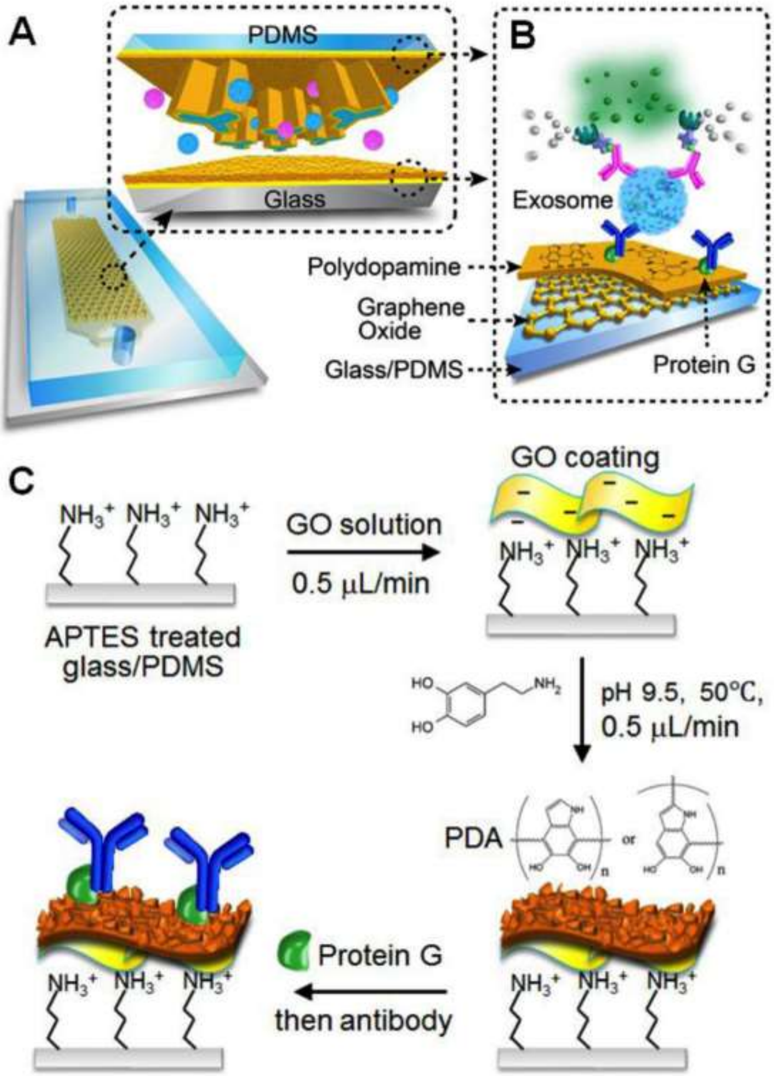

Figure 3. nano-IMEX; the combined GO/PDA complex and surface chemistry of exosome detection(P. Zhang, He, and Zeng 2016).

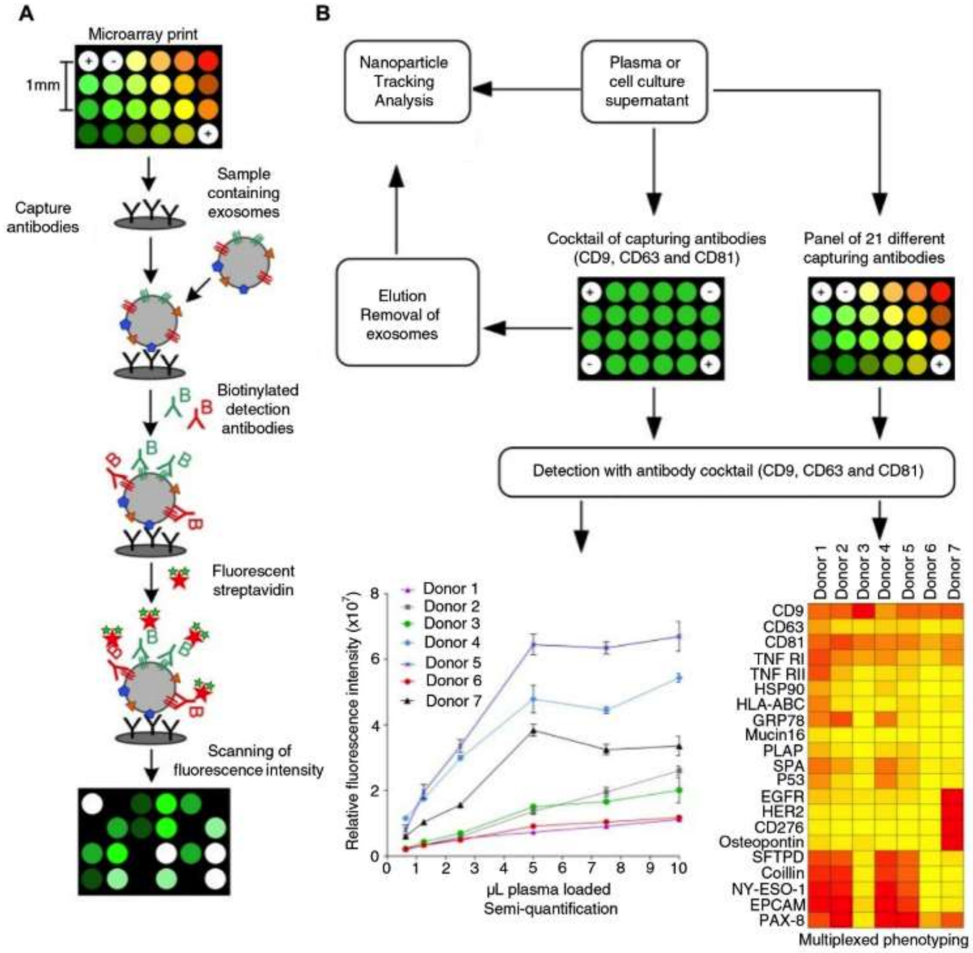

Figure 4. A study by Jorgensen et al., an EV Array was utilized to capture exosomes and a cocktail of biotinylated antibodies against the tetraspanins CD9, CD63 and CD81 was used to detect exosome with help of fluorescence-labelled streptavidin (Jorgensen et al., 2013).

Two studies were consummated to determine exosomal membrane proteins that may be used as biomarkers for lung cancer and non-small cell lung cancer (NSCLC); both utilized 49 different antibodies to capture and differentiate samples from a total of 857 individuals (cohorts of 581 and 276 individuals respectively). Biotin-conjugated antibodies of the exosome surface proteins CD9, C81, and CD63 were used to monitor the captured exosomes. CD151, CD171, and Tetraspanin8 were shown to be the most abundant differentiators of lung cancer, where CD171, CD276, Tetraspanin8, Flotilin1, and NY-ESO-1 were the same for NSCLC. The studies continued with survival rate analysis with which previously obtained results were supported. The comprehensive studies provide a strong basis for future research on diagnosis of NSCLC and lung cancer via exosome membrane proteins (Sandfeld-Paulsen, Aggerholm-Pedersen, et al., 2016; Sandfeld-Paulsen, Jakobsen, et al., 2016).

In another study, an automated centrifugal microfluidic disc system integrated with functionalized membranes (Exo-CMDS) is proposed for the isolation and enrichment of exosomes. The system is summarized in Figure 5. Subsequently, these exosomes are processed using a novel aptamer fluorescence system (Exo-AFS) to effectively detect surface proteins on exosomes. Exo-CMDS demonstrates high yields, achieving an optimal exosomal concentration of 5.1×10^9 particles/mL from trace amounts of blood samples (<300 μL) in just 8 minutes. This accomplishes one-step exosome isolation and purification. The limit of detection (LoD) for PD-L1 in Exo-AFS is as low as 1.58×10^5 particles/mL (S. Zhao et al. 2022). In clinical sample trials, the diagnostic accuracy of lung cancer using Exo-CMDS and Exo-AFS reaches 91% (95% CI: 79%–96%), surpassing ELISA results (area under the curve: 0.9378 versus 0.8733; 30 patients). Exo-CMDS and Exo-AFS exhibit advantages in terms of cost-effectiveness, speed, purity, sensitivity, and specificity when compared to traditional techniques. These assays hold promise as practical means for early cancer detection and guiding immunotherapy in clinical settings.

In a study that is depicted in Figure 6, a dual-antibody assay was employed to enhance specificity in the detection of exosomes associated with lung cancer. Given that exosomes are secreted under both physiological and pathological conditions, the objective was to selectively capture exosomes originating from lung cancer cells and quantitatively assess the fluorescence signal disparity between plasma samples from lung cancer patients and healthy individuals. The assay utilized horseradish peroxidase (HRP)-based signal amplification to achieve heightened sensitivity in exosome detection. This dual-antibody assay, coupled with HRP-based signal amplification, provided a highly sensitive and specific method for the detection of lung cancer-associated exosomes. The findings, underscore the potential of this approach in improving early diagnosis and monitoring of lung cancer, offering a promising tool for clinical applications and advancing personalized medicine.

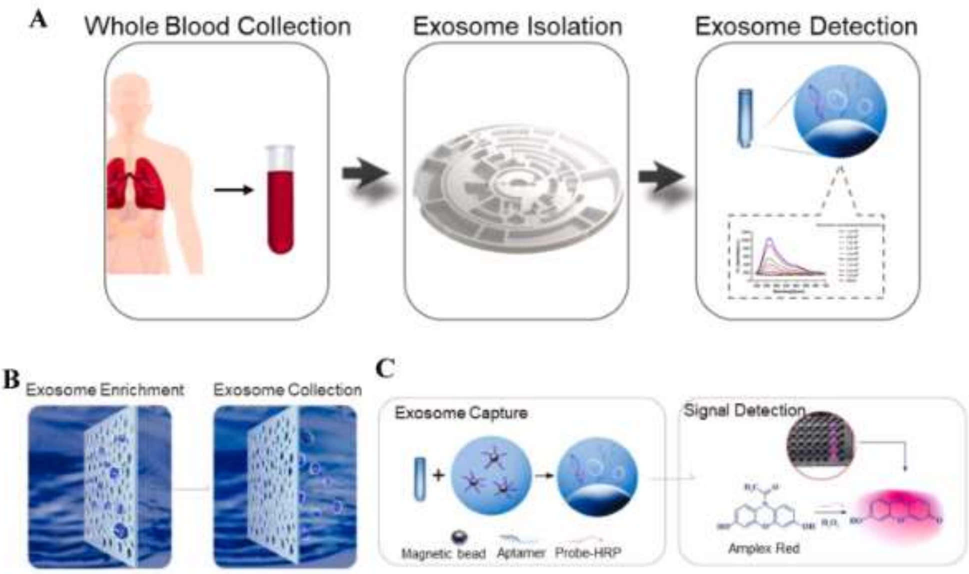

Figure 5. The schematic of the exosome isolation and detection. A, Study design, including whole blood collection, exosome isolation and exosome detection. B, The principle of exosomes enrichment and elution. C, The principle of exosomes capture and detection (S. Zhao et al. 2022).

In another study, in order to enhance sensitivity, two surface proteins enriched in lung-derived exosomes were identified for targeting, which is demonstrated in Figure 6. CD81, a characteristic tetraspanin membrane protein enriched on the surface of lung-derived exosomes (Mei He et al. 2014), and CD151, recognized as a cancer-associated protein (Sandfeld-Paulsen, Aggerholm-Pedersen, et al. 2016). Magnetic nanoparticle (MNP)-conjugated CD151 was employed for capturing lung cancer-associated exosomes, while HRP-conjugated CD81 was used for detection via fluorescence signals. The combination of MNP and HRP conjugates in plasma formed a sandwich structure "MNP-Exosome-HRP," as depicted in Figure 6 fluorogenic substrate, AUR/H2O2, was utilized for HRP catalysis. Following the immunomagnetic capture of lung-derived exosomes, the substrate was introduced into the solution. The hydrogen peroxide (H_2O_2) reacted with the fluorogenic substrate in the presence of exosome-bound peroxidase enzyme in a 1:1 stoichiometry, generating a bright fluorescent product (AmplexR UltroxRed) detected at λex/λem 480/595 nm (Singh et al. 2022).

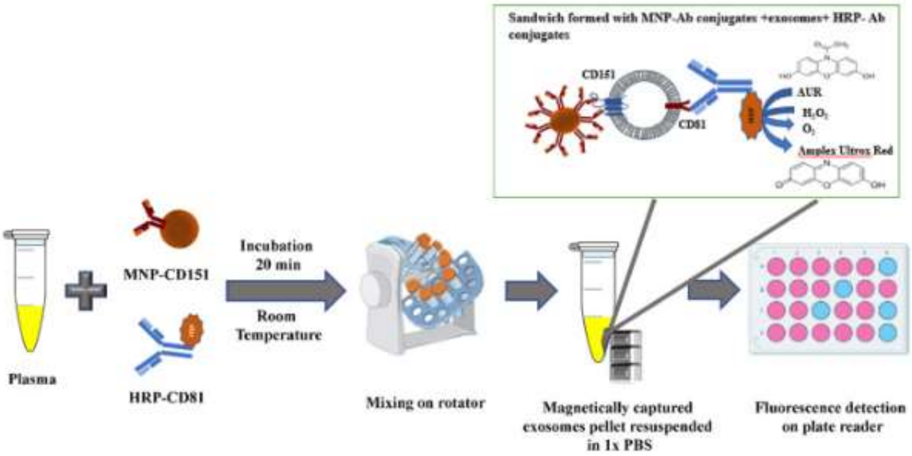

Figure 6. Schematic of the co-capture assay. This assay relied on immunomagnetic capture and HRP-based enzymatic signal amplification for lung-derived exosome detection from plasma samples (Singh et al. 2022).

In conclusion, liquid biopsy and methodologies that has been utilized for such purposes are being investigated in depth. However, current methodologies either lack the required sensitivity or are not suitable for usual check-up procedures. Recent studies show a promising convergence to a point where sensitive point of care applications will be possible and applicable. Two of the optical detection principles for sensitive and rapid point of care applications are discussed in detail in the following sections.

1.3 Plasmon Based Biosensors

Plasmonic methods eliminate the need of labeling, and offer real-time monitoring, and can work with relatively small amounts of samples. These advantages provided a new area of development for methodologies that are more practical compared to conventional methods such as ELISA and western blotting. Plasmons can be described as plasma oscillations that are fixed to an ion generally a metal. Optical properties of metals are largely affected by plasmons; light below a specific frequency (plasma frequency) is reflected by the metal surfaces while light above that frequency is transmitted. Metals such as gold have a plasma frequency in visible range, differentiating their absorbance characteristics. This property is utilized by taking advantage of the electromagnetic field (evanescent wave field) that extends away from metal surface. In summary; light that is not confined within the metal might be used for sensor purposes (Prasad 2003). When a single wavelength is applied the evanescent waves can change the reflectivity characteristics of a fixed field; decaying from the surface. Hence a total internal reflection on the metal layer generates a plasmonic field at its specific wavelength of the incident light, which determines the reflectivity conditions(Schasfoort 2017).

1.3.1 Surface Plasmon Resonance (SPR)

The excitation of surface plasmon waves was first described in early twentieth century (Wood 1902) but it was not a focus of study until Otto and Kretschmann developed relatively simple setup to excite plasmons via attenuated total reflection (ATR),(Haxha et al. 2015; Otto 1968). Surface plasmon resonance exists in between two media with opposite signed dielectric constants. As described in Figure 7, as the incident light is transmitted and reflected; the angle of incident light and reflected light are equal. If the light has a lower wavelength than plasmon frequency this leads to an interaction between metal electrons and the light transmitted. This phenomenon excites the electrons and causes a perpendicular electromagnetic field, which decays hastily and is called an evanescent field. Resonance between the incident light and the evanescent field is then achieved by tuning the angle of incident light. When the resonance between the incident light and electromagnetic field is reached; there is no reflected light; in other words there is an immediate decrease in reflectivity. This phenomenon provides a sensitive and label-free reflectivity measurement methodology, which can be utilized in various biochemical assays (Raether, 1988; Suto et al., 1989; Tilley, 1983).

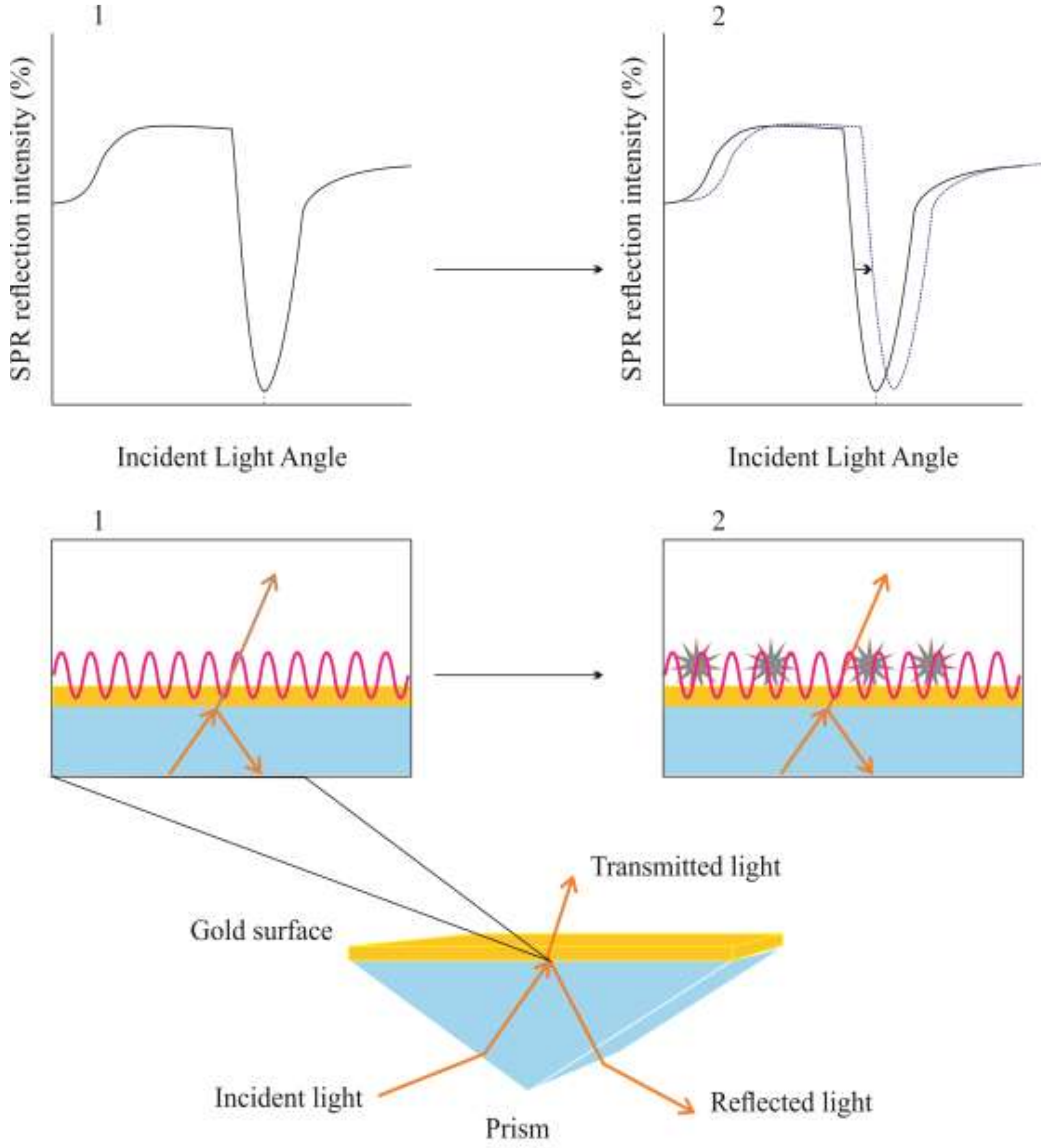

Figure 7. Surface plasmon resonance in Kretschmann configuration and transduction of a surface interaction.

1.3.2 Localized Surface Plasmon Resonance (LSPR)

Even though infinite films of metal surfaces are utilized for SPR applications, other geometries of metals also show plasmon resonance. Same as SPR, when incident light interacts with conductive particles, the electromagnetic field of light causes a collective oscillation of conduction band electrons. This phenomenon is called localized surface plasmons resonance (LSPR); and the resonance characteristics are highly dependent on particle properties such as size, geometry, composition, and concentration. LSPR induces highly localized electromagnetic fields around the particles, which brings particles to be fine sensors of local refractive index. Also the particles' optical absorption becomes maximum at plasmon resonance frequency, which is in the visible light wavelengths. The maximum absorption peak (λ_{max}) is highly dependent on refractive index of medium surrounding the particles; this is the basis for sensor applications. The resonance frequency is relatively easy to measure, which makes LSPR applications favorable for nanoscale sensor utilizations and that can easily be transduced by spectrophotometric methods (Mayer and Hafner 2011; Petryayeva and Krull 2011; Willets and Van Duyne 2007). Gold nanoparticles (GNPs) are the first and most common geometry that was used for LSPR applications. The colorimetric properties of colloidal gold nanoparticles enables selective detection of various components without the requirement of agglutination or aggregation of particles, and it provides an SPR shift detection in liquid phase, which details can be seen in Figure 8 (Englebienne 1998).

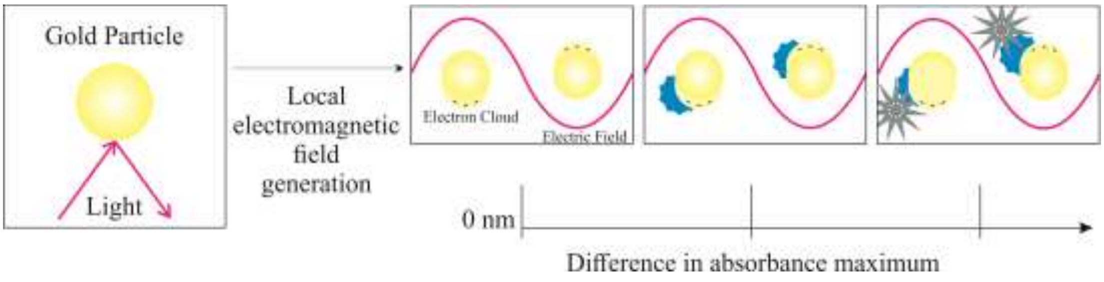

Figure 8. Simplified LSPR transduction mechanism.

Localized Surface Plasmon Resonance (LSPR)-based biosensors, while offering unique advantages, present certain drawbacks too. One notable limitation lies in the inherent sensitivity of LSPR to changes in the immediate vicinity of the metallic nanostructures, rendering them susceptible to variations in local refractive indices (Bingham, Hall, and Van Duyne 2012). This localized sensitivity restricts the dynamic range of LSPR-based sensors, leading to challenges in precisely quantifying analyte concentrations over a broad spectrum. Furthermore, LSPR biosensors often grapple with issues of reproducibility and standardization due to the intricate fabrication processes involved in generating precisely controlled nanostructures. The inherent variability in these fabrication methods may result in non-uniform sensor responses, impeding the reliability and comparability of LSPR-based measurements across different platforms and laboratories. In contrast to conventional SPR biosensors, which exhibit a more extended sensing area, LSPR biosensors are limited by their localized nature and –conventionally- liquid medium. This hinders the simultaneous investigation of multiple interactions, potentially compromising the throughput and efficiency of biomolecular binding studies . In summary, while LSPR-based biosensors offer unique advantages in terms of miniaturization and simpler detection, their drawbacks, including limited dynamic range, reproducibility issues, and constrained sensing areas, underscore the importance of enhancing the sensitivity of sensor platforms. There are various strategies such as utilizing bimetal alloys, growing particles in size, using particles with different morphologies, and core-shell type particle employment (Brown and Natan 1998; Brown, Walter, and Natan 2000; Brown et al. 2000; Kumar, Gandhi, and Kumar 2007; Sau et al. 2011; P. Zhao, Li, and Astruc 2013; Dikkumbura et al. 2021; Steinbrück et al. 2011; Borah and Verbruggen 2020; J. He, Wu, and Sun 2019; Lu et al. 2013; Selvakannan et al. 2004; Hamidi-Asl et al. 2016; Loiseau et al. 2019). Nonetheless, a limitation exists in the correlation between optical sensitivity and enhancement methodology, attributable to the adverse effects of colloidal stability deterioration resulting from size and subsequent particle aggregation in solution. Therefore, maintaining precise control over particle morphology and other modifications is imperative.

Recently, a plasmonic system (nPLEX), which combines isolation and detection of exosomes was proposed. Proposed microfluidic system offers easy isolation step and surface plasmon-based analysis step to achieve label-free exosome detection. For this purpose a gold film with periodic nanohole arrays on it were fabricated and nanoholes were optimized to match the size of exosomes (~100nm in diameter). Excitation of the array by a single wavelength caused surface plasmon field to be excited while ensuring high sensitivity for refractive index differentiations. The nanohole surface was then coated by different antibodies against certain exosomal membrane proteins for molecular specificity. Captured protein levels were comparable with results of ELISA (matched by $R^2>98\%$). In addition, correlation between exosomes and their parental cells were monitored that both EpCAM and CD24 proteins were elevated in samples from individuals with ovarian cancer (Im et al. 2014; 2015).

Another study was conducted with same motivation utilizing surface plasmon resonance imaging (SPRi) methodology to detect exosomal proteins. Antibody functionalized (antibodies against exosomal surface proteins such as tetraspanins (e.g. CD9), glycoprotein CD41b, and tyrosine kinase receptor MET) gold-coated glass chip was used as sensor interface. Human hepatoma cells lines and mouse melanoma cell lines were used as model organisms, and cell culture supernatants (CCS) were used with and without isolation steps. One of the very first results of this study is that the developed methodology does not require any pretreatment of CCS. Exosome levels of MHCC97H and MHCC97L cell lines (former is highly more metastatic) were compared to determine any correlation between metastatic potential of cell lines and exosome levels, which showed a positive correlation. It is concluded that the developed methodology provides a potential test for cancer metastasis, and furthermore with the future use of specific antibody microarrays it is possible to differentiate and even diagnose cancer (L. Zhu et al. 2014).

A recent work presents an aptamer-based Surface Plasmon Resonance (SPR) sensor designed for the direct and sensitive detection of exosomes. The results in Figure 9 illustrate the detection of target exosomes through direct measurement, a single gold nanoparticle (AuNP) amplified SPR aptasensor, and a dual AuNP amplified SPR aptasensor. Initially, the Au film was functionalized with capture DNA, and the target exosomes were directly measured. Subsequently, aptamer/T30-linked AuNPs were introduced, amplifying the signal in the single AuNP-amplified SPR aptasensor for detecting target exosomes. Finally, A30-coated AuNPs, through the hybridization of complementary sequences T30 and A30, were captured on the aptamer/T30-linked AuNPs, enabling the detection of target exosomes in the dual AuNP-amplified SPR aptasensor.

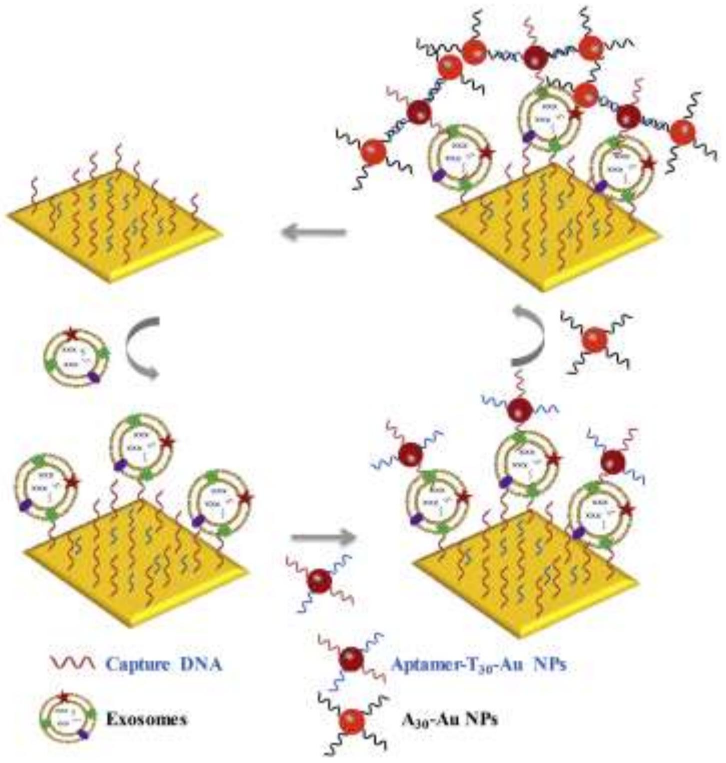

Figure 9. Dual AuNP-assisted signal amplification for determination of exosomes (Wang et al. 2019).

By employing dual AuNP-assisted signal amplification, the method achieved the detection of exosomes at low concentrations. This approach offers an effective means for sensitive exosome detection and holds promise for applications in biological and clinical studies (Wang et al. 2019).

Glioblastoma (GBM) is a deadly brain tumor where secreted lactate increases the expression of CD44 and the release of exosomes. Researchers discovered that lactate-driven CD44 upregulation in malignant glioblastoma cells (GMs) enhances the release of CD44-rich exosomes. These exosomes, in turn, boost the migration of GBM cells and the formation of tubes in endothelial cells. The study used advanced techniques to detect CD44 in these exosomes. The “capture and sensing” Titanium Nitride (TiN) - Nanoholes (NH) - discs immunocapture (TIC) - atomic force microscopy (AFM) and the highly sensitive TiN–NH-localized surface plasmon resonance (LSPR) biosensors were employed. The detection limits for exosomal CD44 were 5.29 × 10^{-1} µg/ml with TIC-AFM and 3.46 × 10^{-3} µg/ml with TiN–NH-LSPR. Significantly, this research demonstrated for the first time that the label-free sensitive TiN–NH-LSPR biosensor can detect and quantify elevated levels of CD44 and CD133 in immunocaptured GBM cell-derived exosomes found in the blood and cerebrospinal fluid of a GBM mouse model. These findings suggest the potential use of biosensors for minimally invasive molecular diagnostics through liquid biopsy (Thakur et al. 2021).

Another recent study utilized LSPR to detect GBM associated exosomes. GBM has cells that under low oxygen conditions (hypoxia) increase the release of exosomes. Researchers have developed an LSPR sensor chip to detect minute quantities of these exosomal biomarkers. This sensor chip uses self-assembled silver nanoparticles on gold nano-islands (Ag@AuNIs) to create a platform for biotinylated antibodies that target exosomal surface markers. The biotinylated antibody functionalized (BAF) Ag@AuNIs LSPR biosensor can sensitively detect the exosome marker CD63 and the GBM progression biomarker monocarboxylate transporter 4 (MCT4) in malignant GBM cell-derived exosomes. It demonstrated detection ranges from as low as 0.38 ng/ml for one marker and 1.4 ng/ml for the other. The biosensor also was able to quantify MCT4 in exosomes isolated from the blood of GBM mice using epidermal growth factor receptor variant III-based immunocapture, highlighting its potential for non-invasive monitoring of GBM progression via liquid biopsy (Liu et al. 2022).

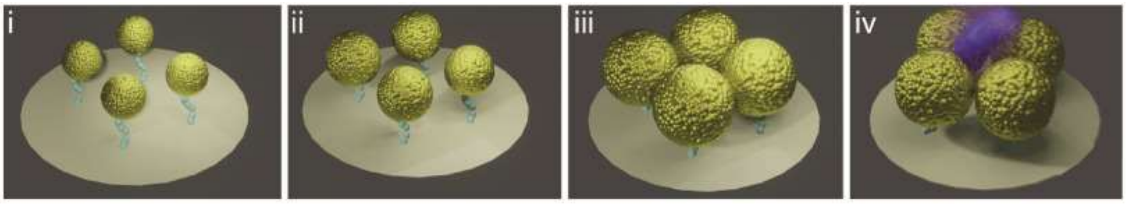

Figure 10. Schematic of GNP immobilization, i-GNP growth, and bacteria capturing with LSPR based chrono-spectral gold growth biosensor (Sözmen et al. 2024).

A study that was carried out in our laboratory presents a novel methodology aimed at enhancing the sensitivity of LSPR based sensor platforms. The technique involves the time-dependent growth of GNPs, referred to as chrono-growth, on a solid support. The developed sensor platform was employed for the detection of model microorganisms as part of a validation study. To achieve this, 20 nm GNPs were immobilized onto a solid support, and controlled growth of the immobilized GNPs (i-GNPs) was executed. Chrono-growth of i-GNPs led to a significant reduction in inter-particular distance, thereby enhancing the plasmonic sensitivity of the grown GNPs (g-GNP). The growth of i-GNPs was primarily controlled by reaction time, enabling the fabrication of tunable plasmonic nanostructures. Structures were optimized in terms of sensitivity enhancement by utilizing reaction time as a parameter. The optimized nanostructures were then employed for the detection of model microorganisms. Through the application of artificial neural networks (ANN), the sensor platform successfully differentiated between low (10^2–10^4 CFU/ml) and high (above 10^5 CFU/ml) *E.coli* concentrations. This work demonstrates the effectiveness of the time-dependent growth and sensor enhancement technique in detecting *E.coli* at concentrations as low as 10^2 CFU/ml (Sözmen et al. 2024).

Overall, plasmonic sensor systems are still in need of further development to be applicable for cancer diagnosis and prognosis. Main short comings of the systems are sensitivity, resolution, and reproducibility as described above and seen in the current literature survey. This calls for enhancement studies for betterment of said characteristics. The principle in its core holds the key to surpassing the necessity of complex devices and specific expertise of personnel, and with elaborative work it would benefit the liquid biopsy technique greatly.

1.4 Magnetic Levitation Based Sensors

Magnetic levitation (MagLev) provides a density-based measurement method which is considerably sensitive and versatile. The fundamental of the technique is the usage of magnetic force to overcome gravitational force; and imitate a field without gravitational effects (Bloxham et al. 2015; Laithwaite 1975). This phenomenon is generally reached by utilizing magnets, and simplest form is two dipole magnets oriented facing each other's same poles; so called anti-Helmholtz configuration. A paramagnetic medium is used to suspend objects or samples within the created magnetic field; this procures a method without complexity and with high sensitivity, which is used to resolve finitely small differences in density of the levitated object or objects. As an object is levitated at a fixed height in medium, based on its density; if or when it’s density increases it’s levitation height decreases and vice versa (Nemiroski et al. 2016). Systems generally compose of two identical static magnets to generate a constant magnetic field, a paramagnetic agent in the medium between the two which positions the object based on their densities, and an imaging device such as a microscope (Turker and Arslan-Yildiz 2018).

The base approach is to use standard beads or microspheres with known densities and measure their levitation heights in the MagLev sensor platform. Then a calibration curve with Y axis as density and X axis as height or vertical position is drawn with acquired data. Lastly the analyte is introduced to the system and levitated, its levitation height is implemented into the calibration curve to determine its density based on previous data provided by standard beads. A summary of the procedure can be seen in Figure 11 (Ashkarran & Mahmoudi, 2021).

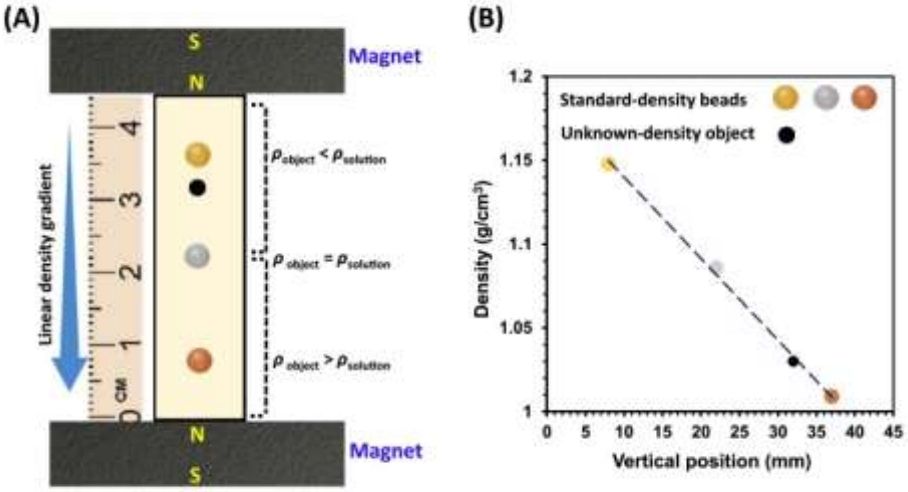

Figure 11. Density measurement in a MagLev sensor platform A) levitation heights of standard beads and an analyte, B) calibration curve with standard beads and analyte marked on (Ashkarran and Mahmoudi 2021).

One of the pioneering sensor technologies utilizing magnetic levitation was developed by Mirica et al., the sensor platform was designed to monitor density change during chemical reactions that are carried on a solid support. They described a straightforward benchtop method which involved usage of polystyrene beads that are levitated in paramagnetic solution (Mn^{2+} or Gd^{3+}) between two magnets. The platform succeeded to determine density differences as small as 0.01 g/cm^3 (Katherine A Mirica et al. 2008). In next year the same research group improved the accuracy of the platform down to 0.002 g/cm^3. Also, they showed that the same platform can be used to measure the density of liquids by levitating a droplet of organic liquids in the paramagnetic solution. Although they used a rather large platform which caused an unreliability in measurements of particles smaller than 2 μm in diameter and the detection range of said platform was in between densities of 0.8-3 g/cm^3, it was a promising study and showed that magnetic levitation is a well-suited method to measure relative difference in density and chemical compositions (Mirica et al., 2009, 2010).

One of the recent biosensor applications of these systems were used to separate a mixture of two species of cells. The study was carried out by Zhu et al., and successfully separated a mixture of live *E. coli* and *S. cerevisiae* cells. Standard soft-lithography was utilized to produce microfluidic magnetic levitation devices out of polydimethylsiloxane (PDMS). Figure 12 represents technical drawing and prototype of the device (T. Zhu et al. 2012).

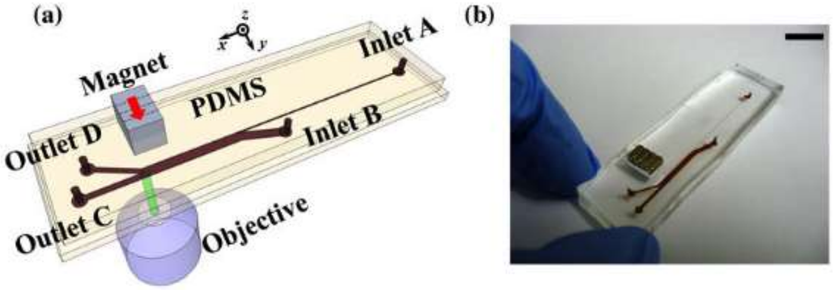

Figure 12. Schematic of the developed device 1) permanent magnets and microfludidic channel. b) Prototype device (scale bar: 10mm) (T. Zhu et al. 2012).

Then the samples from both outlets were analyzed and it was revealed that the device works with ~100% efficiency. In conclusion a label-free and simple to use device was developed that is able to sort cells with ~100% efficiency at a rate of 10^7

cells/h (T. Zhu et al. 2012). Another study reported by Amin et al., utilized a similar sensor platform to construct flow-assisted magnetic levitation sensor platform which procures applications on larger volumes. Analyte is pumped into the platform via a micro-pump and a highly laminar flow is ensured. Samples levitate in the capillary and flow through; imaging is carried out by a smartphone which is attached to a magnifying lens (Amin et al. 2016). Zhang et al. had taken a more theoretical approach on the field and developed a linear relationship description between density and magnetic levitation height. COMSOL software was utilized for this purpose. A numerical simulation was generated in COMSOL and removed the need of the standard density analysis with glass or polymer beads. This provided a convenient method of simulation which simplifies experimentation process (Chengqian Zhang et al. 2018). MagLev was utilized to distinguish unique differences in levitation and density blueprints between breast, esophageal, colorectal, and NSCL cancer cell lines, as well as heterogeneity within these seemingly homogenous cell populations. Furthermore, a resolution of 1 x 10^{-4} g/mL was demonstrated bu the developed methodology. Figure 13 summarizes the utilized setup, and it was shown that MagLev technique was adequate to monitor minor changes in cellular density that may be caused by several cancers and moreover, heterogeneities within a single cancer (Durmus et al. 2015).

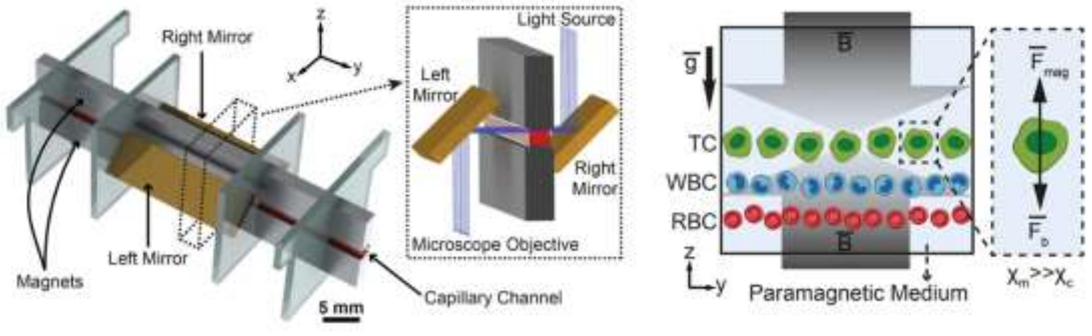

Figure 13. The procedure that has been carried out to vary cell’s densities and measurement of densities of cells (Durmus et al., 2015).

Another study suggests a PoC detection method based on MagLev technique. A MagLev based assay was developed demonstrating *Hepatitis C* (HCV) detection; the assay utilizes a MagLev setup and a smart phone for imaging. Antibody functionalized microspheres are suspended in the setup and they were used to capture HCV antigen and with the change in their density. First the levitation height of microspheres was measured in absence of any antibody or antigen Then step by step levitation heights of microspheres were recorded; after antibody functionalization and after introduction of HCV antigen to the medium, the results were shown as in Figure 14 and it showed an LoD value of 50 µg/ml. The assay proves that MagLev based sensors are sensitive enough for even protein assays and they provide several advantages as no need of external mechanism or devices except for a smart phone, adaptability, and simple usage (Ozefe & Arslan Yildiz, 2020).

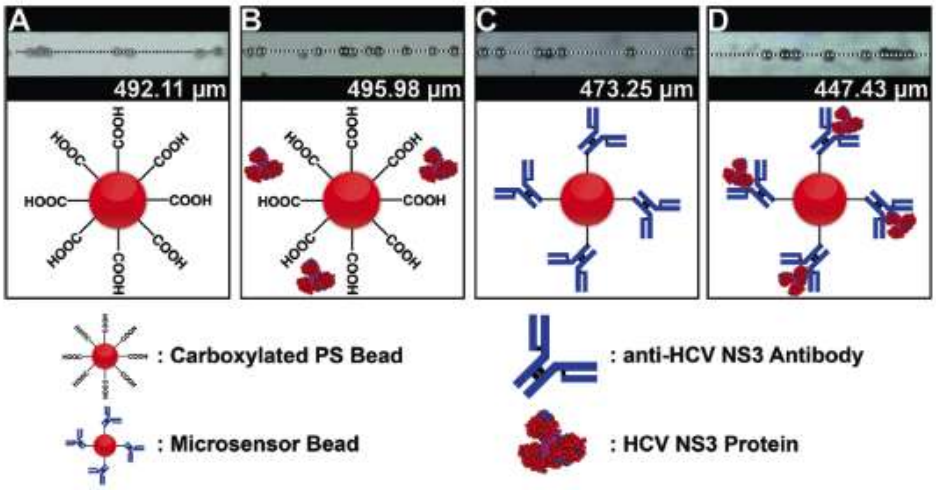

Figure 14. Procedure of HCV detection on MagLev sensor platform A) Carboxyl functionalized polystyrene beads, B) Polystyrene bead in presence of Hep-C antigen, C) Antibody functionalized polystyrene beads, D) Antibody functionalized beads in presence of Hep-C antibody (Ozefe and Arslan Yildiz 2020).

Motivated by the significant importance of MagLev technology, the issue of describing and modeling the MagLev technique from a first-principle perspective is addressed in a recent study. Specifically, the focus of the investigation is on establishing the relation that expresses the mutual interaction between the magnetic fields emanating from a solenoid and a passive object. The object's magnetization is exclusively induced by the applied magnetic field. Consequently, a force equation is derived to depict the impact of the magnetic field along the solenoid axis on a small ferromagnetic object, such as a ball. Additionally, the approach introduced in the study results in a relationship illustrating the dependence of the inductance on the distance from the solenoid. To experimentally validate the derived equations, a laboratory device known as the 'Magnetic Levitation CE152' module was employed. A simplified nonlinear dynamic model was constructed, where all parameters possess physical meaning and are represented by appropriate physical quantities. The values of the inductance parameters, based on the distance from the solenoid, were determined from the measured courses of the control voltage of the current amplifier of the solenoid and the voltage of the ball position sensor. Through a comparison of the calculated parameters with the expected values and an assessment of the model's error concerning the object's distance from the coil, the study then discusses the validity and correctness of the relations describing the magnetic field strength of the solenoid acting on the small ball object which resolves the linear relationship between the levitation height of a particle with the force exerted on that particle (Dušek et al., 2023).

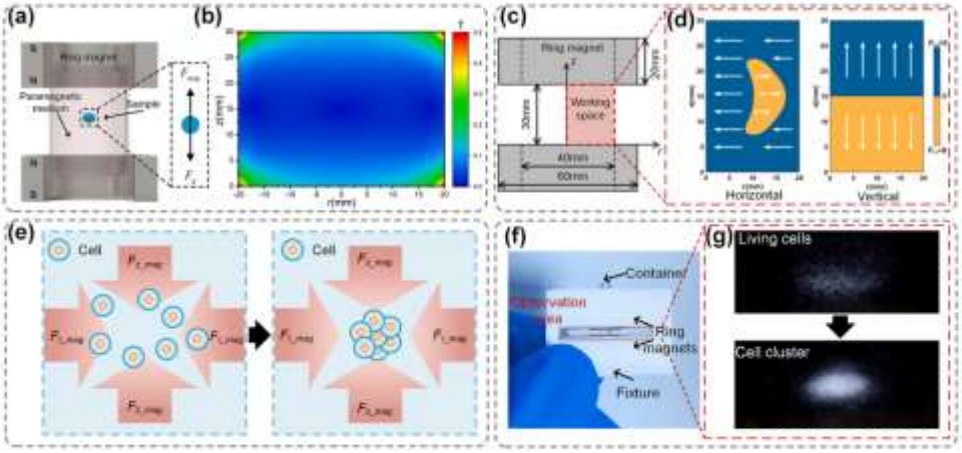

Figure 15. Diagram of the magnetic levitation method; (a) Configuration of the magnetic levitation device with a pair of H20 magnets (b) Magnetic field between two facing H20 magnets (c) Diagram of the working space between two facing H20 magnets for analysis. (d) Nephogram of horizontal and vertical components of magnetic force (e) Illustration of the aggregation of cells during the magnetic levitation (f) Diagram of the

magnetic levitation device with two H3 ring magnets (g) The levitation and aggregation process of cells (Lyu et al. 2023).

A configuration of magnetic levitation based on two ring magnets is introduced in a recent work. The proposed setup has the capability to achieve cohesive levitation of cells for three-dimensional tissue culture and distinguish between cell types and conditions based on their densities. Specifically, a unified mathematical model of the configuration is established to facilitate the understanding of three-dimensional distributions and gradients of the magnetic field throughout the entire working space. The established mathematical model offers several advantages: (i) enabling magnetic levitation and manipulation of samples in the three-dimensional space, not limited to the axial region of the device; (ii) breaking through size and separation distance restrictions, making it applicable to various samples ranging in size from microns to centimeters; (iii) allowing adjustment of manipulating spaces and ranges based on the mathematical model, thereby enhancing method accuracy and feasibility. Utilizing the theoretical model, a magnetic levitation device was designed for levitating cells. Experimental results confirmed the feasibility of magnetic levitation for cell manipulation and measurement of cell densities. The average densities of four types of cells were successfully measured. Furthermore, magnetic levitation demonstrated its capability to detect dead cells and living cells based on density differences (Lyu et al., 2023).

Herewith, MagLev based sensor technologies bear great potential for density-based detection and quantification systems. Although, the technique was never employed for exosome detection due to its recent emergence; it is highly feasible for this utilization. In conclusion, MagLev-based sensors have the potential to be used in liquid biopsy, thus providing a new frontier for innovative methodologies for cancer diagnosis.

1.5 Purpose of Thesis

Current technologies to prognose, diagnose or monitor cancer are not effective at early-stages of cancer; they are either not reliable, or too invasive for casual check-up procedures. To overcome above-mentioned obstacles, this work has started with the inspiration to develop optical sensor platforms for prognosis, diagnosis, and monitoring of cancer while employing cancerous exosomal membrane proteins as biomarkers. Throughout this study novel optical detection methodologies and related biosensor with the purpose of being employed in future liquid biopsy techniques will be designed and developed.

Non-Small Cell Lung Cancer (NSCLC) is selected as the model for this purpose due to it is well defined membrane protein profile and also the lack of early diagnosis with current methodologies. The vision that was followed here was to produce microfluidic platforms that are sensitive, selective, and precise, where at the same time portable, cheap, and easy to use. It was aimed to contribute to develop microfluidic biosensor platforms where it would be possible to be used at resource limited settings, without sophisticated instrumentation, even by non-expert individuals.

Main goal of the thesis is to fabricate optical biosensor platforms that are capable of selectively and sensitively detect exosomes with specific membrane protein or proteins. For this purpose CD proteins that are known to be or suspected to be linked with NSCLC disease will be made use of. CD81 will be targeted as an exosomal biomarker, EpCAM as an exosomal cancer biomarker, and CD151 as a NSCLC exosomal biomarker. The detection will be carried out via LSPR and Magnetic Levitation methodologies. The sensor platforms for both methods will be fabricated during this study. First, design, fabrication, and optimization of the biosensor platforms will be carried out using a model protein, Bovine Serum Albumin. Then these platforms will be tested by detecting said membrane protein standards in solubilized forms. This test will also include the intention of characterizing the biosensor platforms in terms of sensory characteristics such as detection limit, sensitivity, and dynamic detection range. After the platforms prove to be able to satisfactorily detect and quantify determined exosomal membrane proteins. They will be utilized for exosome detection studies.

Exosome detection applications will include detection of exosomes that are cell culture derived. Cell lines A549, MRC5, and WI38 are determined as model cell lines for this purpose, A549 as a NSCLC fibroblast cell line and both MRC5 and WI38 as healthy lung fibroblast cell lines. Each cell line is going to be cultured to confluency, then cell culture supernatants will be retracted, and exosome isolation will be carried out via use of a commercial cell culture exosome isolation kit. Samples from each cell line will be subjected to the detection studies for each of the aforementioned membrane proteins with no pretreatment other than exosome isolation. Each sample will be diluted with various dilution factors to compare if there is a relation between exosome concentration and signal generation by the biosensor platforms. Statistical tools will be utilized to compare the results both between healthy and cancerous samples and with concentration variations.

In conclusion, two biosensor platforms with separate detection principles will be developed, optimized, characterized, and utilized for exosome detection with the aim of reaching a promising applicability for future liquid biopsy applications that would hopefully pave the road for cancer diagnosis and prognosis applications in the future with following studies and investigations.

CHAPTER 2

MATERIALS AND METHODS

2.1 Cell Culture for *in-vitro* Exosome Acquisition and Characterization

2.1.1 Cell Culturing of Cell Line A549, MRC5, and WI38

A549 (CCL-185), MRC5 (CCL-171), and WI38 (CCL-75) cell lines were separately cultured in DMEM cell culture medium and supplemented with fetal bovine serum (FBS) and 1% Pen/Strep at 5% CO_2 concentration and 37^{o}C. Cell culture supernatants (CCS) were used as exosome sources for further analysis after acquiring, they were used for exosome isolation.

2.1.2 Exosome Isolation

A tandem of centrifugation step and exosome isolation kit was used for separation of *in-vitro* exosomes form CCS; first centrifugation was done at 500g for 5 minutes, and supernatant was separated and used in further steps. Next Cell Culture Exosome Isolation kit (Norgen, Canada) was used. After utilization of the exosome isolation kit, isolated exosomes were directly used. Storage time of the isolated exosomes were always kept under a week, and they were stored at 4 ^{o}C to prevent undesired freeze and thawing, keeping isolated exosomes intact.

2.1.3 Size analyses

NanoPlus DLS Nano Particle Size and Zeta Potential Analyzer was used to determine sizes of isolated exosomes. Mean zeta value will be measured and exosome sizes was calculated utilizing the equation below.

$$\mathrm{D_z} = \frac{\sum \mathrm{S_i}}{\sum \frac{\mathrm{S_i}}{\mathrm{D_i}}}$$

2.1.4 Exosome Count Calculation

A theoretical calculation was carried out for exosomes, for this purpose following method was deduced and applied. Lipid vesicles were prepared as a standard for this measurement and further calculations. First, lipid vesicles that are similar to exosomes in size were prepared via extrusion. For this purpose, a working solution was prepared beforehand via solving PC in chloroform then evaporating chloroform via N_2 gas flow; leaving thin film of PC on the container walls. As the last step the PC thin film was solved in PBS via freeze thaw method. A syringe extruder was utilized, and 4 different pore sized membranes were used for the procedure; 50, 100, 200, and 400nm (Ong et al. 2016).

Following equation set was deduced and used, utilizing DLS analyses results of both prepared liposomes and isolated exosome samples (Mehdiani et al. 2015; Mozafari, Mazaheri, and Dormiani 2021)

N(liposomes) = [M_a (Molecular mass of PC) x N (Avogadro Number)] / [N(tot) x 1000]

Where N (liposomes) is liposomes per liter and N (tot) is number of lipid molecules per liposome.

$N(tot) = [4\pi R^2 + 4\pi(R-h)^2]/A$

R = radius of vesicles

h = thickness of bilayer (about 5 nm for PC)

A= cross sectional area of head group ($0.71nm^2$)

2.1.5 Immunostaining

Rhodamine conjugated secondary antibodies (Thermo, 31685) were used to stain exosomes. Fixation of isolated exosomes was carried out via 15 min incubation of 4% Paraformaldehyde (PFA). After removal of PFA via rinsing with PBS, 50 µl primary antibody (Ab185684; Ab71916; Ab155760; Abcam) (1:40 dilution) was added to the wells and incubated for an hour. After washing away the excess antibody (Ab), 50µl secondary Ab (1:100 dilution) was added to the well and incubated for two hours. After rinsing fluorescent microscopy was utilized to capture images with 10x, 20x, and 40x magnification.

2.2 LSPR Sensor Platform Development and Validation

2.2.1 Gold Nanoparticle Synthesis

Turkevich method was utilized to synthesize citrate capped GNPs with the size of 20 nm. Synthesis started with the heating of an auric chloride ($HAuCl_4$) solution of 0.5mM, and 60ml to boil and let cool down to 70^{o}C; then a trisodium citrate dehydrate ($Na_3C_6H_5O_7$) solution of 38.8 mM and was added and stirred until a red color appeared. The GNP solution was stored at 4^{o}C until usage (Turkevich et al., 1951). The GNP solution was centrifuged at 12000 for 10 min before usage, then precipitated GNPs were resuspended with ultra-pure water.

2.2.2 LSPR Sensor Platform Fabrication

LSPR sensor fabrication consisted of the following steps: *(i)* nanoparticle immobilization into well of 96 well-plates, *(ii)* functionalization of said NPs with 11-mercaptoundecanoic acid (MUA; Thermo) to provide a carboxyl functional group for further surface modifications, and *(iii)* functionalization of NPs with antibodies via

EDC/NHS coupling. The immobilization process was started with the Poly-L-lysine (Sigma-Aldrich) incubation in each well of a flat bottomed, 96-well plate (Corning, Costar); 100 μL of 50 ppm PLL was incubated overnight in wells, the excess was rinsed from the surface via MQ water (Elveren and Yıldız 2018; Chang et al. 2018; Cataldi et al. 2014). Afterwards, 50 μL of synthesized GNP solution was added to each well and incubated overnight. Next, GNP immobilized wells were incubated in 0.1 μM MUA solution overnight. This process provided a carboxylic acid functional group that is available for EDC (Sigma Aldrich) to bind to. After the incubation EDC-NHS protocol was followed. 0.4M EDC and 0.1M NHS (Sigma Aldrich) solutions were mixed equivolumetrically and added to wells, then incubated for 30 minutes. Afterwards, Ab solution was added to wells and incubated for an hour. Then, excess Ab was removed via PBS wash.

2.2.3 LSPR Sensor Platform Optimization

An absorbance peak (λ_{max}) is observed through LSPR that is in UV–Vis range. Herein, several methods for enhancing LSPR sensor sensitivity and utility were investigated. For this purpose, NPs with various sizes, morphologies, and compositions were synthesized. Syntheses were carried out via well-established, modified, and novel methods for tuning of NPs during the study. The synthesized NPs were characterized via SEM imaging (Quanta 250), EDX analyses (Quanta 250), UV-Vis spectrum (*Thermo Scientific Multiscan GO*), and DLS measurements (Horiba Partica LA-960V2) and optimization was done with reaction time, reactant concentration and ratios as parameters. Effectivity of the sensitivity enhancement was then tested via a model protein and then exosomal membrane proteins of interest. Moreover, various tuning applications were carried out for several NPs such as in-situ size growth and coating for further tuning.

2.2.4 Silver Nanoparticle Synthesis

A modified Turkevich method was utilized to synthesize citrate capped Silver Nanoparticles (SNPs) with the size of 20 nm (Kimling et al. 2006). Synthesis started with the heating of a Silver Nitrate ($AgNO_3$, Sigma Aldrich) solution of 0.5mM, and 60ml to boil and let cool down to 70^{o}C; then a tri-sodium citrate dehydrate ($Na_3C_6H_5O_7$, Sigma Aldrich) solution of 38.8 mM and was added and stirred until a yellow color appeared. The SNP solution was stored at 4^{o}C until usage.

2.2.5 Nanoparticle Growth and Coating

After the immobilization of the GNPs, the excess GNP solution was washed away by MQ water. 20 µL of 5 mM $HAuCl_4$ and 80 µL of 6 mM NH_2OH (Sigma Aldrich) solutions were added simultaneously and incubated up to 15 minutes for GNP growth. Then, the reaction was ceased by addition of MQ water. Prior to and after each step of the process absorbance spectrum measurements were carried out in 100 µL MQ water to monitor immobilization and growth. Same procedure was followed for silver growth on immobilized SNPs, instead of $HAuCl_4$, $AgNO_3$ was used, and instead of NH_2OH, L-Ascorbate (Sigma Aldrich) was utilized. Growth took 20-30 minutes unlike Gold growth.

Silver and Gold coating on immobilized GNP and SNPs were carried out as described above, respectively.

2.2.6 Core-Shell Nanoparticle Synthesis

After GNP synthesis, GNPs were centrifugated and removed from the medium, then resuspended in MQ water with various dilution factor. Subsequently, $AgNO_3$ and L-ascorbic acid solution were added to GNP solution in this order. 1 mg/mL $AgNO_3$ and 4 mg/mL L-ascorbic acid solution were prepared for this purpose. Into 5 mL GNP solution various amounts of $AgNO_3$ and L-ascorbic acid solution were added; between 30-75% of silver to gold ratio and 1.6:1 ratio of silver to ascorbate. Reaction took 2 hours at room temperature, afterwards core-shell gold-silver NPs were stored at +4^{o}C.

2.2.7 Nanoparticle Characterization

Characterization of NPs was carried out via SEM imaging, EDX analyses, UV-Vis spectrum measurement, DLS size measurement and Zeta potential analyses (Roy and Mohanta 2019).

SEM and EDX characterizations were obtained on an aluminum surface. For this purpose, *Scanning Electron Microscope (SEM) (FEI Quanta 250 FEG) and Energy Dispersive X-ray Spectroscopy (EDX) (FEI Quanta 250 FEG)* were used. Obtained results were analyzed in terms of nanoparticle’s geometric shapes, atom constitutions and molecule analysis.

UV-Vis Absorbance Spectrum characterizations were used during the optimization process for understanding the reaction kinetics *(Thermo Scientific Multiscan GO).* Also, the shapes and sizes of the synthesized gold nanoparticles were investigated indirectly. For this purpose absorption spectrum of nanoparticles were measured utilizing the plate reader. Peak intensity and locations were analyzed to indirectly investigate nanoparticle morphology

Dynamic Light Scattering (DLS) measurements were done on Dynamic Light Scattering Analysis Instrument (Horiba Partica LA-960V2). Potential measurements were used for the charges of the nanoparticles whilst size measurements were done to analyze the size and dispersity of the particles. The size data acquired here was used to verify the indirect measurements by UV-Vis.

Zeta Potential Analyses NanoPlus DLS Nano Particle Size and Zeta Potential Analyzer were used to determine zeta potential of exosomes. Zeta potential measurement was carried out by the determination of electrokinetic potential of colloidal dispersion. (Elveren and Yıldız 2018).

2.2.8 Protein Detection via Developed LSPR Sensor Platform

LSPR analysis of BSA were carried out as a model protein. For this purpose, 96 well-plate was functionalized with GNPs and then EDC-NHS protocol was carried out as described before. After activation of surface, without a washing step, 50 µl of Ab was added with 4% dilution in PBS. After half an hour of incubation, excess Ab was removed via rinsing by PBS. Sample BSA protein solutions with decreasing dilutions (1nM, 5nM, 10nM, 50nM, 100nM) were introduced into wells. In order to allow Ab-antigen interaction another 30 min of incubation was carried out. After another step of rinsing with PBS, results were read by plate-reader in the range between 400-800 nm. Each experiment was carried out in six replications. The same procedure was carried out for the membrane proteins EPCAM, CD81, and CD151 with varied concentration ranges depending on the sensor platforms initial response to each protein sample.

2.3 MagLev Sensor Platform Development and Validation

2.3.1 MagLev Sensor Platform Fabrication

Fabrication of MagLev sensor platform began with fabrication of the structural frame out of PMMA layers via Laser Printer (Epilog Zing 16 Laser). Saddles for four mirrors, two magnets and one capillary were fabricated from PMMA sheets via laser ablation. Two permanent N52-grade Neodymium (NdFeB) magnets are arranged in an anti-Helmholtz configuration; same poles oriented towards each other. Four mirrors were positioned such as they would provide an image of the lateral section of capillaries. The assembled platform can be seen in Figure 16.

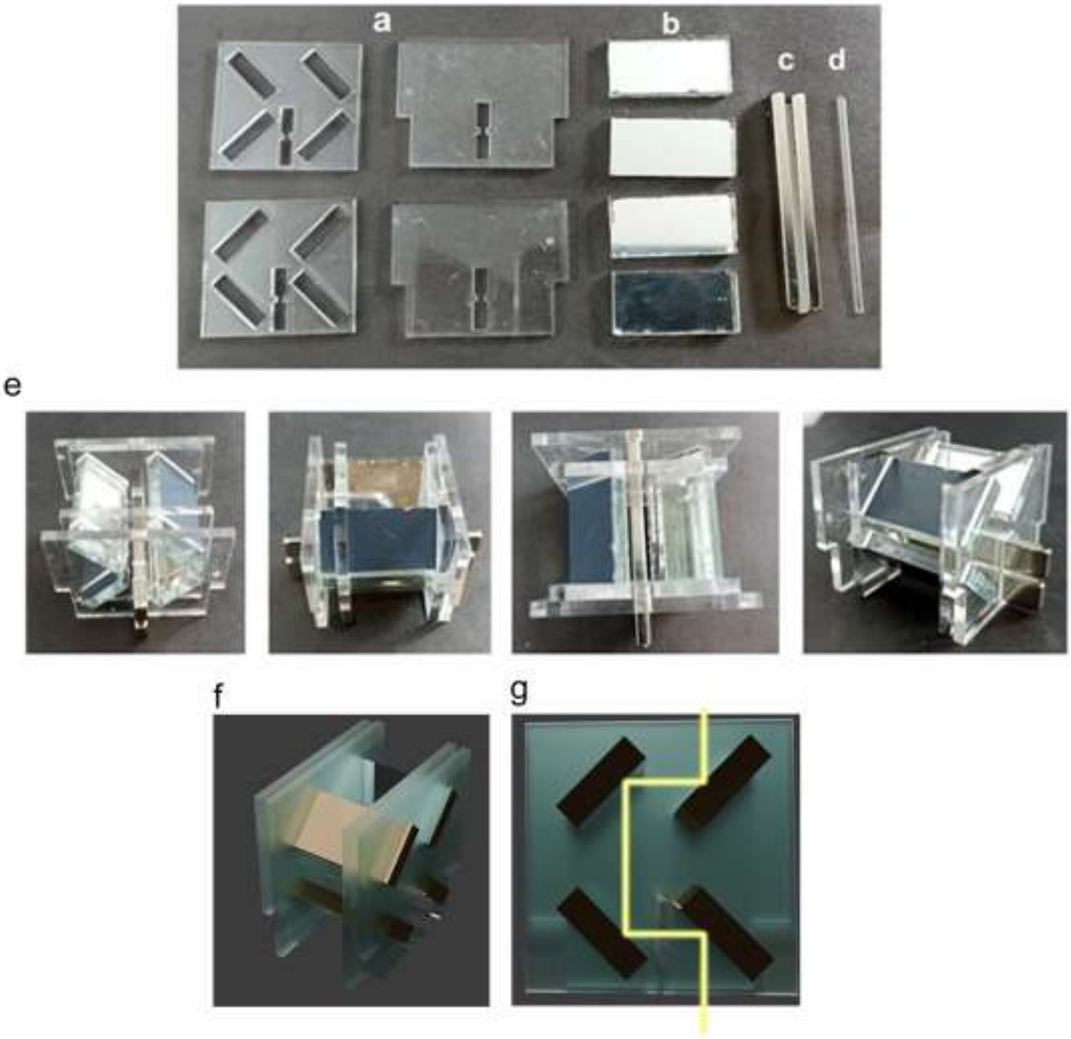

Figure 16. Assembled MagLev Platform, consisting of 4 PMMA layers with saddles (a) for 4 mirrors (b), 2 N-52 magnets (c), and a capillary (d), 3d modelling of the platform (f), light path passing through the platform, reflecting on mirrors for microscopy imaging (g).

2.3.2 Analyses of Acquired MagLev Images

Measurements of magnetic levitation heights were carried out by a code written in MATLAB 2018b software. For this purpose, first, the acquired microscopy images were converted to black and white as the first step of code (Figure 17a), afterwards Sobel method was applied to identify microspheres and the images were converted to

DICOM format, rest of the steps were applied on this format. Structural element addition method was used to clarify the borders of each microsphere (Figure17b) and constituted shapes were filled (Figure17c). Weighted centroid of each shape was determined. Removal of artifacts and noise is carried out by clearing of lines and shapes with unlikely structures were cleared (Figure17d). Lastly distance between each microsphere centroid and bottom line of the capillary was measured (Figure17e). Each of the described steps has been carried out by the code written solely for this purpose; steps are demonstrated in Figure 17.

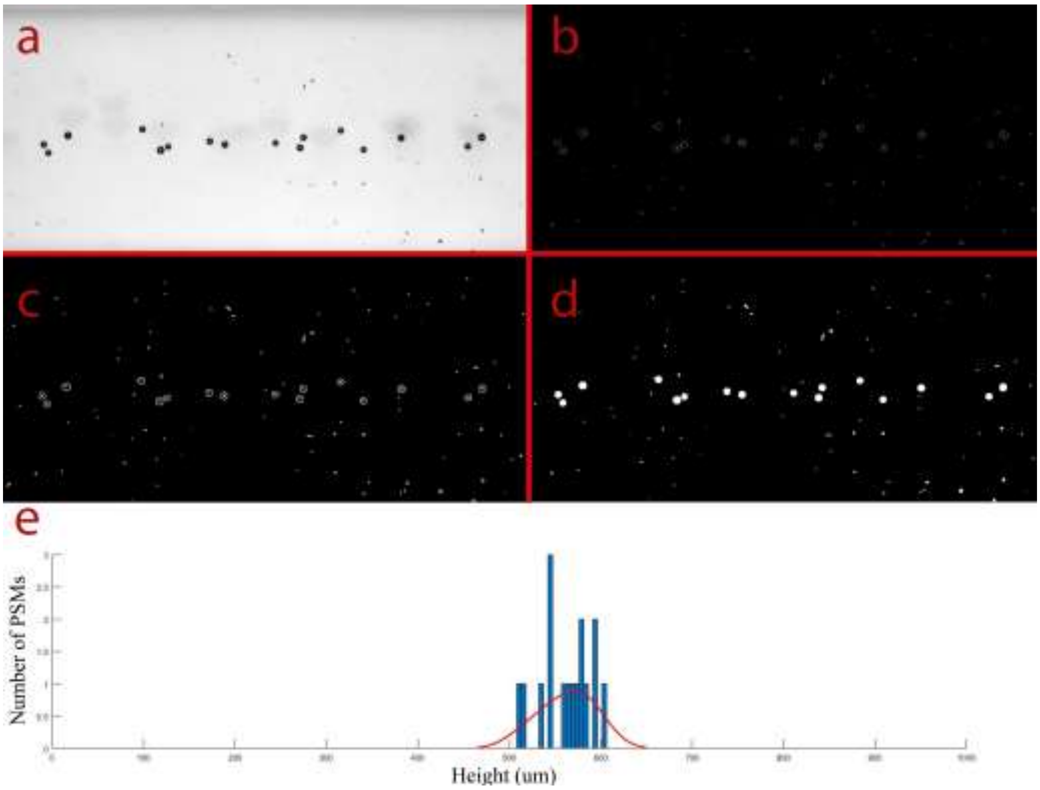

Figure 17. Step by step images produced by MATLAB code that’s used for measurement of magnetic levitation heights 1) Original image, 2) Simplified image by Sobel method, 3)Image after structural element addition, 4)Image after filling constituted shapes, and (bottom) Distribution figure generated by MATLAB 2018b.

2.3.3 MagLev Sensor Platform Optimization

Optimization of MagLev setup was started with determination of the ideal size PSMs for the application. Then, Ab concentration optimization was carried out to calculate the concentration of Ab that would saturate the PSM surfaces for higher interaction with the desired target antigen.

Microsphere Size Optimization

Three sizes of microspheres (5, 20, and 200 µm diameter) were used and standard deviation of sample free microspheres (s_0), standard deviation corrected for LOD calculations (so’), calculated LOD, and p-value of normality test were estimated. Desired values were low s_0 and LOD; and a p-value which would indicate normal distribution of sample-free microspheres in vertical axis; following equations were used for this purpose (Magnusson and Örnemark 2014). Afterwards, dilution rates of microspheres were analyzed in context to determine the most sensitive option to be utilized in the sensor platform.

$s_0^{\iota} = \frac{s_0}{\sqrt{n}}$ *Standard deviation calculation used for further LOD calculations.*

$LOD = 3\ x\ s_0^{\iota}$ *LOD estimation with repeated blank measurements.*

Where:

s_0	*Standard deviation of repeated blank measurements*
s'_0	*Standard deviation value that is used for further LOD and LOQ calculations.*
n	*Number of repeated measurements*
LOD	*Estimated limit of detection*

Antibody Functionalization Optimization

For this purpose, Carboxylated Polystyrene Microspheres (PSMs, lab261) of 20 and 200 µm diameter were used, and EDC/NHS protocol was carried out. For microspheres with 200 µm diameter, 250 µl of each EDC (0.4M) and NHS (0.1M) were mixed and added to PSMs then half an hour of incubation time was given for surface activation. Afterwards 8 µl of 2mg/ml antibody (Ab) was added to the suspension and softly agitated; and another half an hour of incubation time was given. For microspheres with 20 µm, a serial dilution study was carried out to investigate surface saturation point of microspheres with Ab. Centrifuge was used to remove the liquid part of the suspension. Then to remove unattached antibodies 3 washing steps were carried out with PBS. 1ml of PBS was added and PSMs were resuspended then centrifuged (10,000rpm, 10 min for 200 µm, 15,000rpm, 10 min for 20 µm) again. Sediment was then resuspended with 300µl 50 mM paramagnetic solutions.

2.3.4 Protein Detection via Developed MagLev Sensor Platform

MagLev analysis of BSA was carried out as a model protein. For this PSMs were functionalized with anti-BSA Ab utilizing EDC-NHS protocol as described before. After half an hour of incubation excess Ab was removed via washing and centrifugation by PBS. BSA protein solutions with varied concentrations (1nM, 5nM, 10nM, 50nM, and 100nM) were separately added to anti-BSA functionalized PSMs, and two hours of incubation was given for Ab-antigen interaction. The samples were then introduced to MagLev sensor platform through the capillary tube and magnetic levitation heights were measured as described in the sections above. The same procedure was carried out for the target exosomal membrane proteins EPCAM, CD81, and CD151 with varied concentration ranges depending on the sensor platforms initial response to each protein sample.

2.4 Applications of Sensor Platforms for Exosome Detection

After optimization and characterization studies both sensor platforms were utilized to detect exosomes. Platforms were tested both for detection capabilities and their ability to distinguish healthy exosomes from cancerous exosomes.

2.4.1 Exosome Detection via Developed LSPR Sensor Platform

LSPR analysis of *in-vitro* exosomes were conducted. For this purpose, 96 well-plate was functionalized with GNPs and then EDC-NHS protocol was carried out as described in “Protein Detection via Developed LSPR Sensor Platform” section. After activation of surface, without a washing step, 50 µl of Ab was added with 4% dilution in PBS. After half an hour of incubation excess Ab was removed via rinsing by PBS and isolated exosomes were diluted by 1:2, 1:4, and 1:8 rates, then exosome samples were added into wells. After two hours of incubation, results were read by plate-reader in the range between 400-800 nm, and then wavelength shift for each well was calculated as described before. Each experiment was carried out in three replications.

2.4.2 Exosome Detection via Developed MagLev Sensor Platform

MagLev analysis of *in-vitro* exosomes was carried out. Single Ab (either anti-EpCAM, anti-CD81, or anti-CD151) functionalized PSMs were used to capture membrane protein containing exosomes from isolates. Isolated exosomes were diluted by 1:2, 1:4, and 1:8 rates and sensor platform was used to detect said exosomes. Previously described procedure was reenacted with exosomes isolates from cell lines MRC5, A549, and WI38. Samples were introduced to functionalized PSMs and after two hours of incubation magnetic levitation heights were measured of PSM-exosome complexes. All data were subjected to normality tests and ANOVA.

CHAPTER 3

RESULTS & DISCUSSION

3.1 Exosome and Exosome Protein Content Characterization

A549, MRC5, and WI38 cell culture supernatants (CCS) were used as cellular exosome sources for analysis throughout this study. After isolation, exosomes that were isolated from cell culture were characterized; their size, number, and protein content focusing on CD151, CD81, and EpCAM were determined.

3.1.1 Exosome Size Distribution and Exosome Count

Utilizing the equations that were given in methods section, number of phosphatidylcholine molecules that form the artificial liposomes and the number of liposomes in unit volume were calculated that each 100 nm diameter liposome is consisted of 80,047 PCs and each 200 nm diameter liposome consisted of 16,1421 lipids, approximately which totaled up for 2.39 x 10^{13} liposomes per liter for 100 nm diameter liposomes and 1.785 x 10^{13} liposomes per liter for 200nm diameter liposomes. The results of 50 and 400 diameter liposomes were disregarded since it was insignificant after *in-vitro* exosome size measurements (Figure 18).

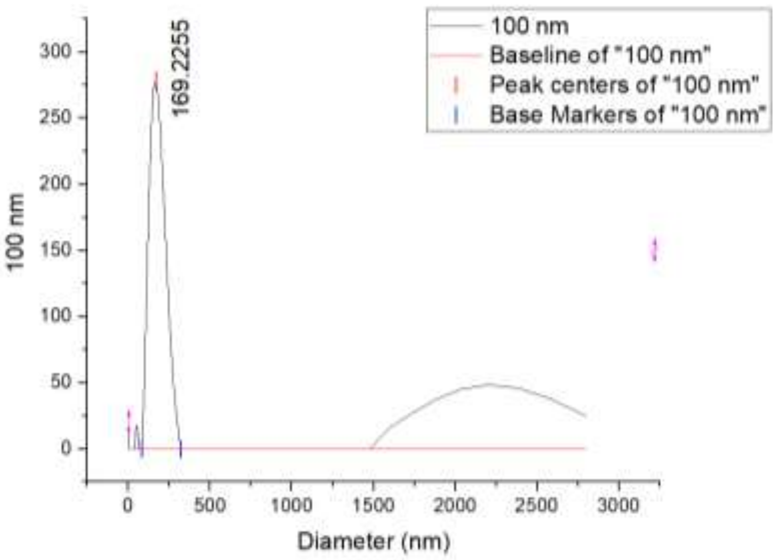

Figure 18. Size measurement results of artificial exosomes of 100nm diameter.

Following Figure 19 shows the Zeta Sizer results of *in-vitro* exosomes.

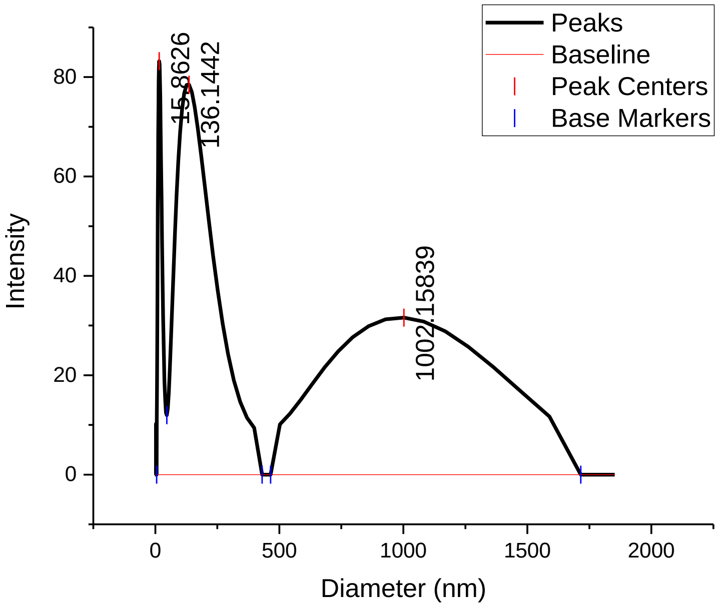

Figure 19. DLS size measurement results of isolated exosomes.

Three peaks were encountered with peak centers of 15.86, 136.14, and 1002.16 nm. The peak at 136.14 nm was assumed to be exosomes and was used for further calculations. Comparing three peaks in the figure the largest curve area is occupied by the 1002.16nm peak with 61.56% of total particles followed by exosomes with 34.29% of total particles. The total area of the exosome peak is calculated to be 14801.39 which were used for exosome concentration calculation.

As Mehdiani et al., proposed the peak area and concentration of lipids are linearly related for homogenous peaks such as our exosome peak (Mehdiani et al. 2015). Peak of 100nm diameter liposomes were used and averaged for this calculation and exosome concentration in isolate was calculated to be 2.9 x 10^9 exosomes/ml and concentration in cell supernatant was calculated to be 5.8 x 10^7 exosomes/ml for A549 isolated exosomes then same procedure was followed for each cell line that was used in this study and also for clinical samples. The table below shows the numbers of exosomes in each cell line that’s been used as an exosome source in this study and also clinical samples. Their graphics showed a similar trend compared to the given A549 cell line’s zeta size results.

Table 2. Exosome count and polydispersity indexes of *in-vitro* and plasma derived exosome samples

Sample	Exosome Count (in isolate)	Polydispersity
A549 cell line	2.90E+09	0.155
MRC5 cell line	1.80E+09	0.272

The resulting data, detailed in the table, presents the quantified exosome numbers for each cell line used as a source of exosomes in this study, alongside corresponding clinical samples. These measurements provide crucial insights into the exosome yields from different cellular sources, comparing cancerous cell line with healthy cell line.

3.1.2 Immunostaining of Isolated Exosomes

Immunostaining of isolated exosomes from A549 and MRC-5 cell lines were also carried out. Resultant microscopy images are given below.

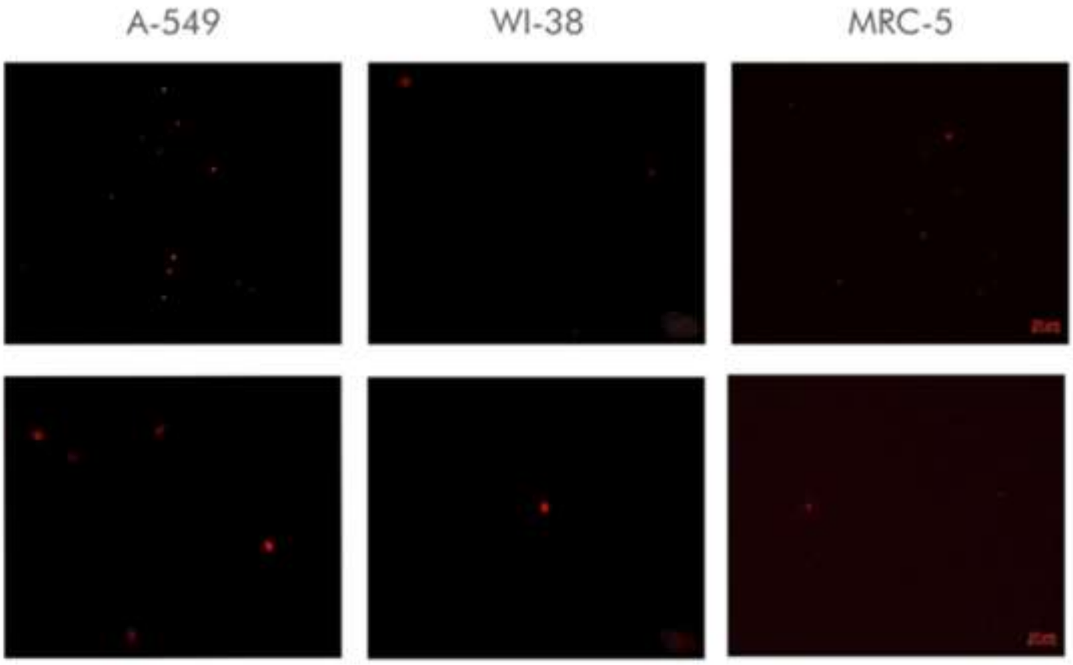

Figure 20. Immunostaining by EpCAM primer Ab, first row 20x magnification; second row 40x magnification.

A549 cell line showed both higher total exosome amount and increased protein expressions of CD151 and EpCAM. Comparing MRC-5 and WI-38; MRC5 might be a better candidate for the healthy control against A549, since it showed lower intensity and lower exosome count in CD151 staining.

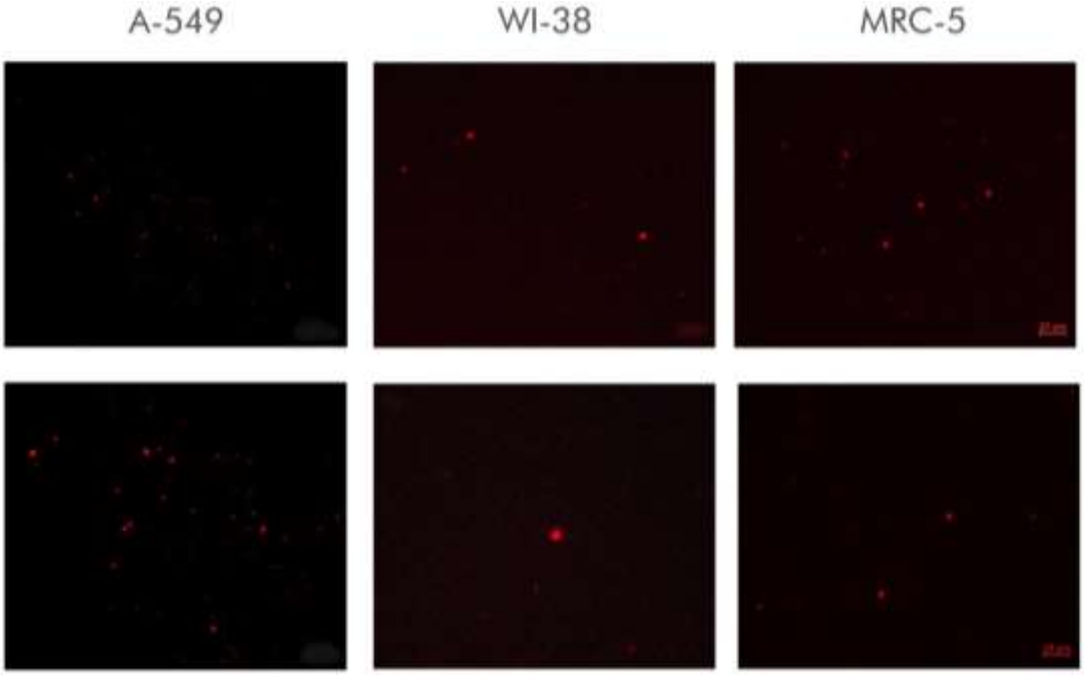

Figure 21.Immunostaining by CD81 primer Ab, first row 20x magnification; second row 40x magnification.

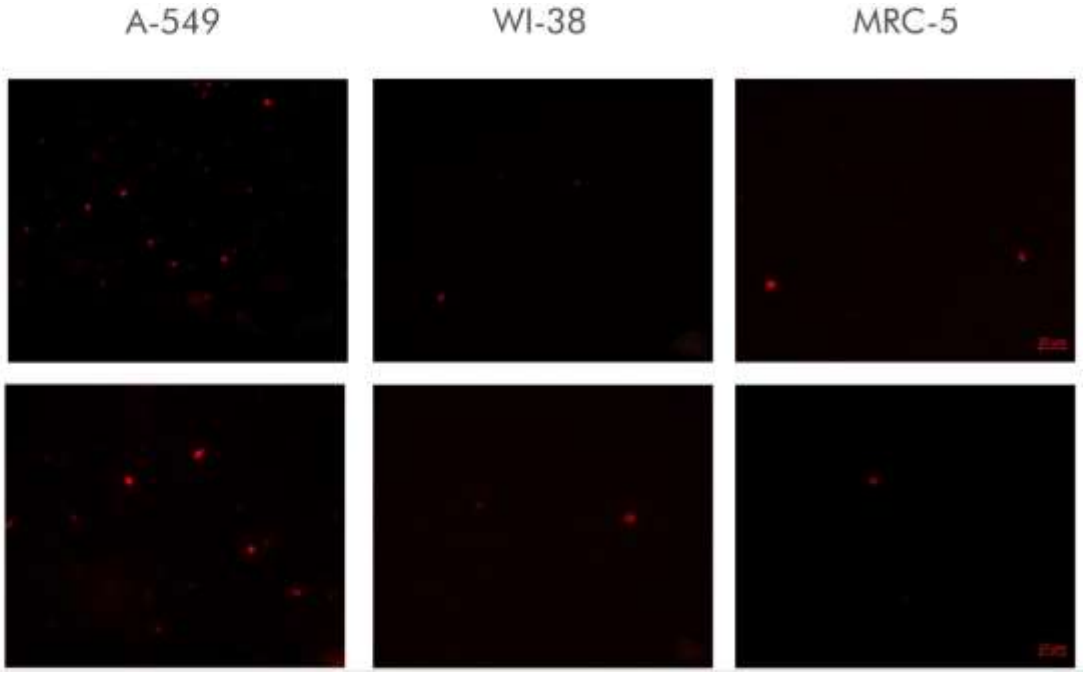

Figure 22. Immunostaining by CD151 primer Ab, first row 20x magnification; second row 40x magnification.

Then acquired images were used to calculate fluorescence intensity of each isolate from each cell line and each membrane protein. Results can be seen in Figure 23.

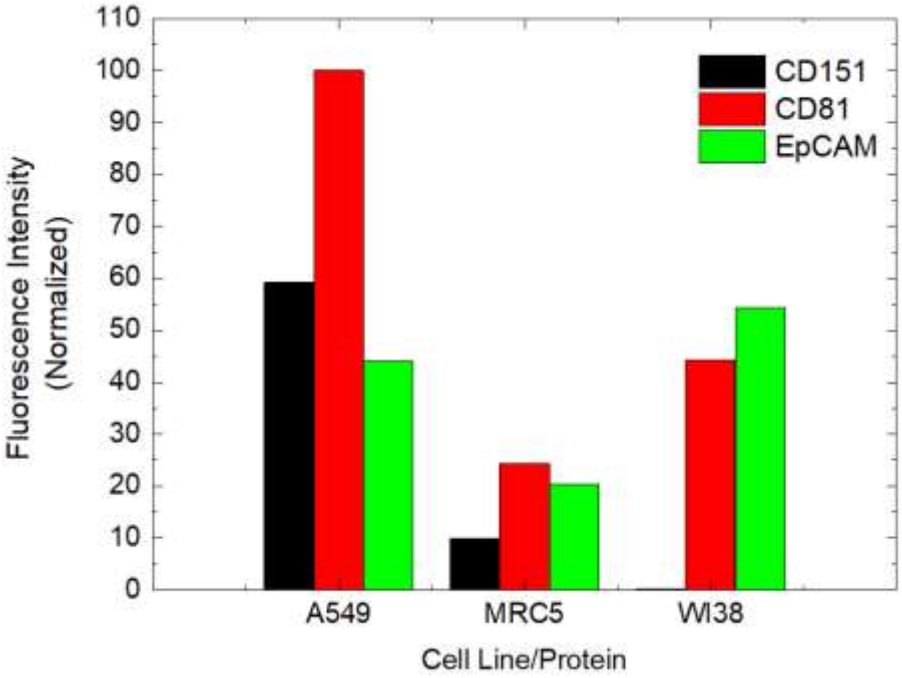

Figure 23.Normalized fluorescence intensity values of studied cell lines; for immunostaining of proteins CD151, CD81, and EpCAM

As Figure 23 shows; A549 cell line originated exosomes had much higher expression rates of CD151 proteins. Also, higher amount of CD81 signal suggests a higher synthesis rate of exosomes. WI38 showed exceptionally higher levels of EpCAM protein which indicates it may not be the rightest choice as a control group, hence it was excluded.

3.2 LSPR Sensor Platform Optimization and Characterization

3.2.1 LSPR Sensor Platform Working Principle

Developed LSPR platform utilized immobilized nanoparticles (NPs) in well plates and utilized as plasmonic platform that provide electron oscillations. Immobilized NPs provided an absorbance peak in the spectra between 400-800 nm. As opposed to a typical setup, where light is directed onto the metallic NP containing solution and the resonance condition is monitored by measuring changes in the reflected or transmitted light intensity, immobilized NPs were utilized for better reproducibility, easier handling, and giving the opportunity for washing steps which would provide lower interference. Position and intensity of this peak depends on the NP size, shape, composition, orientation, and local dielectric environment. Therefore, optimizing the sensory characteristics of LSPR-based sensor platforms such as sensitivity and resolution is highly dependent on NP features that are being used. Observed shifts in absorbance maximum are then correlated with the concentration or presence of analytes, enabling the detection of biomolecular interactions. The working principle of the sensor platform is summarized in Figure 24.

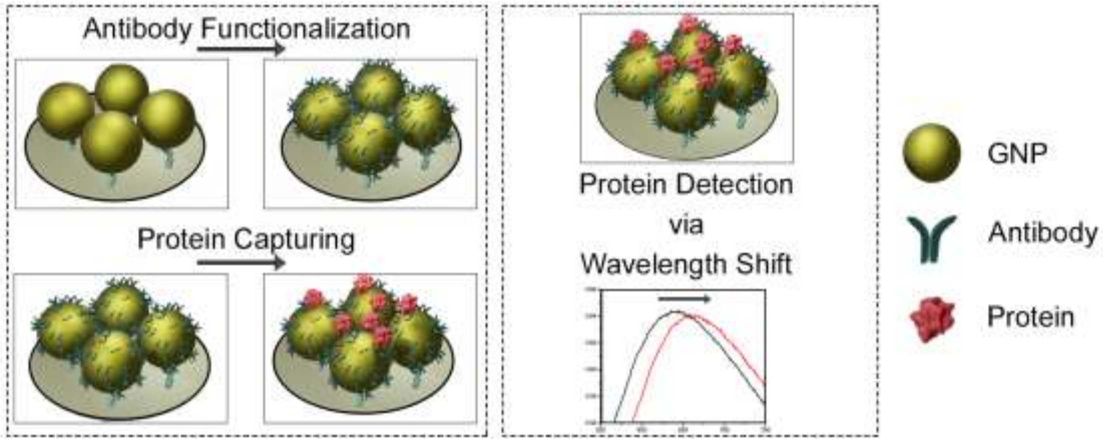

Figure 24. Working principle of LSPR biosensor platform with gold nanoparticles (GNPs) as transducers.

3.2.2 Gold Nanoparticle Synthesis

Spectrophotometric measurements were carried out to determine the size GNPs after synthesis, immobilization, and growth procedures. The spectra were obtained in 100 µL PBS solution at range between 400-800 nm as shown in Figure 25. The acquired peak indicates GNPs with a size ranging between 20-30 nm (Amendola and Meneghetti 2009).

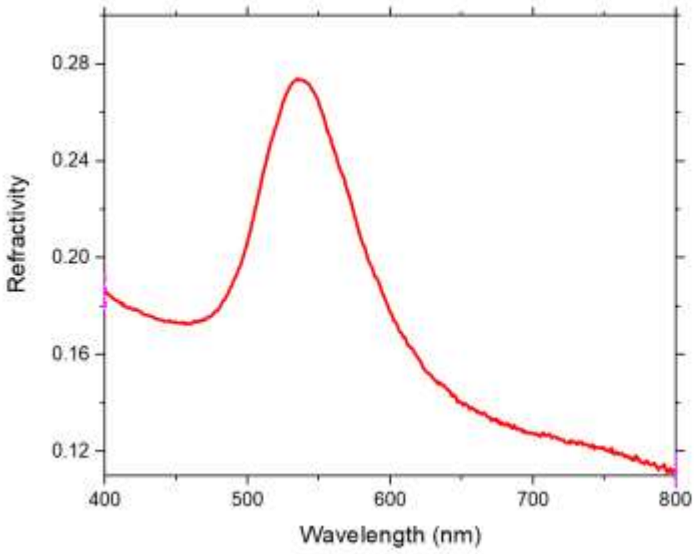

Figure 25. Mean absorbance peak of synthesized GNPs

3.2.3 LSPR Sensor Platform Fabrication

LSPR sensor platform fabrication was carried out as described in methods sections. After each functionalization step a UV-Vis spectral measurement was done. A λ_{max} at 537nm was observed at the beginning and a red-shift was observed with each functionalization step and after protein-Ab interaction. Experimental results demonstrating the said shifts can be seen in the following Figure 26. Briefly, GNPs were immobilized onto well-plates and mercaptoundecanoic acid (MUA) was utilized to functionalize the surface since MUA provides required carboxyl groups for further Ab functionalization. Then protein detection was carried out with the related Ab, in case of the following figure bovine serum albumin (BSA) detection.

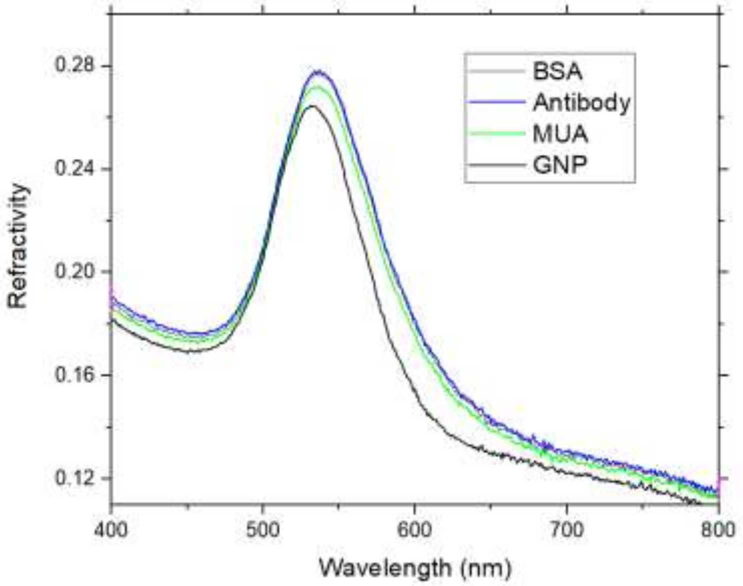

Figure 26. Wavelength shifts observed during the fabrication and utilization of LSPR based biosensor platform with GNPs.

3.2.4 GNP Utilization in Sensor Platform

LSPR applications were started with anti-BSA BSA trials. In following figure responses of BSA with concentrations of 100 µM, 10µM, and 1 µM are shown. LSPR sensor platforms were prepared as described before. The method had become able to detect BSA protein down to 1 µM range. Higher concentrations of anti-BSA (higher than 4% v/v) usage may improve the sensitivity.

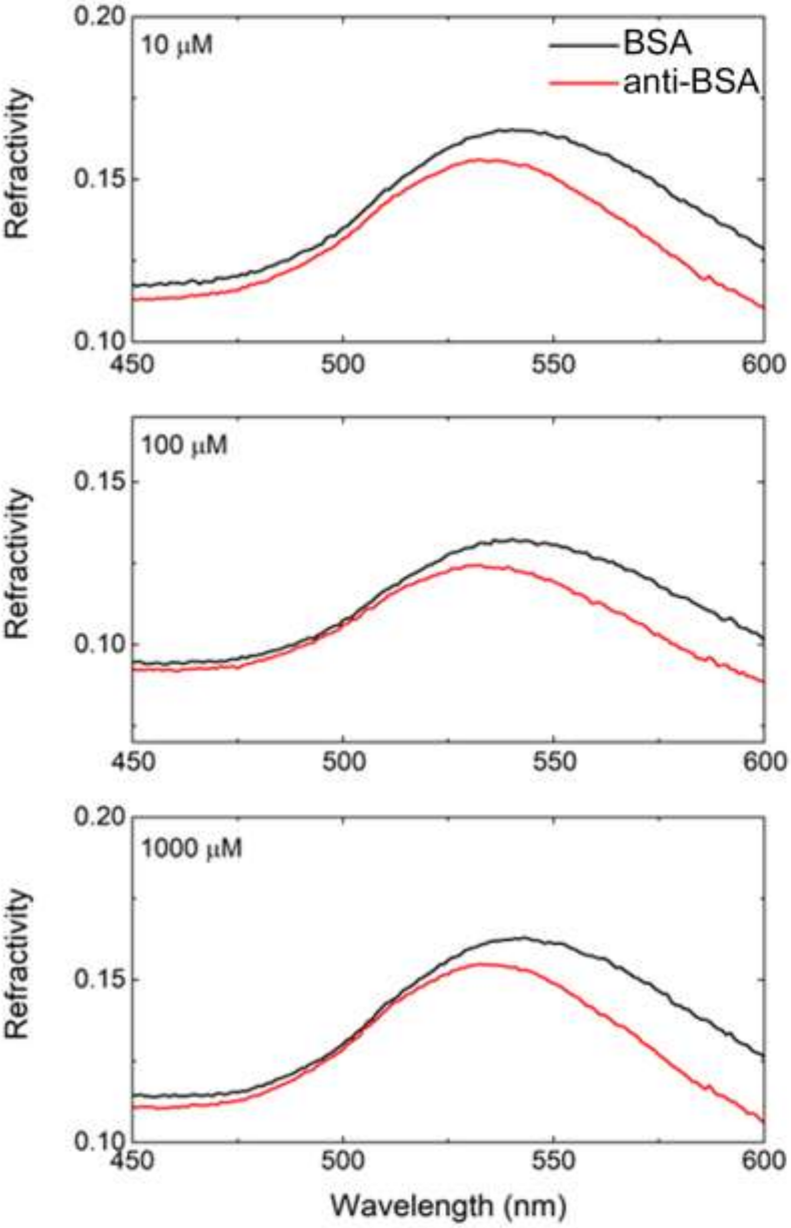

Figure 27. Response signal comparisons between solutions of various concentrations of BSA protein, from top to bottom; 10 μM, 100 μM, and 1000 μM.

3.2.5 Membrane Protein Detection

Next, LSPR applications were carried out for samples with protein concentrations in the range between 1 and 100 nM. For this purpose anti-BSA functionalization was carried out as described before and anti-EpCAM Ab with 1 μg/ml was used for functionalization. Results can be seen in Figure 28.

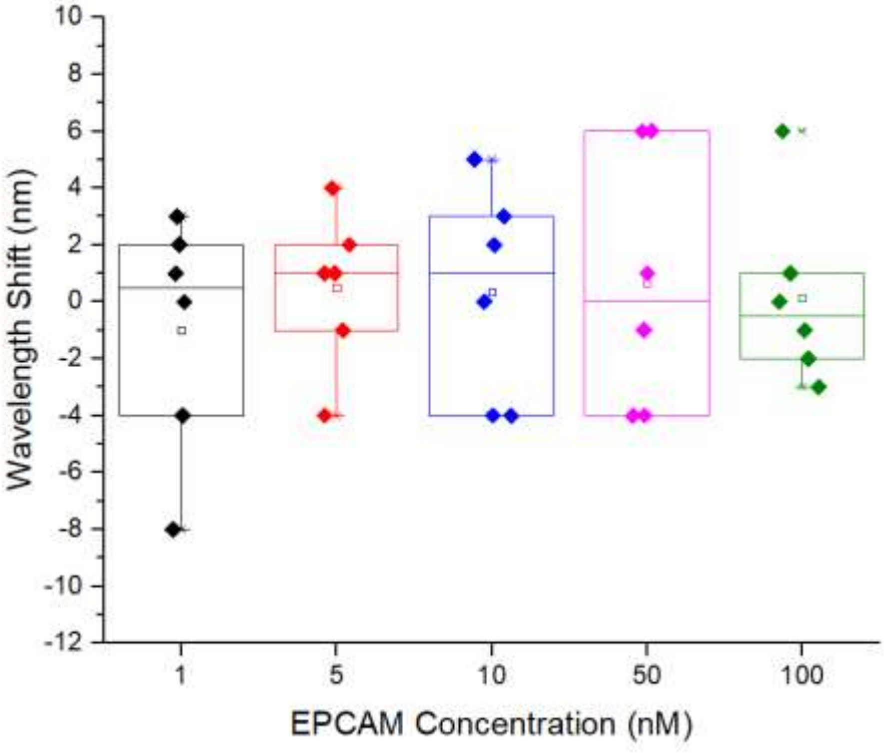

Figure 28. LSPR results of EPCAM protein detection study utilizing GNPs.

Although no significant difference in $\Delta\lambda_{max}$ was observed before and after Ab-protein interactions it was evident that Ab functionalization was detectable; a sample graphic can be seen in Figure 29. It also shows that there was an increase in absorbance intensity too.

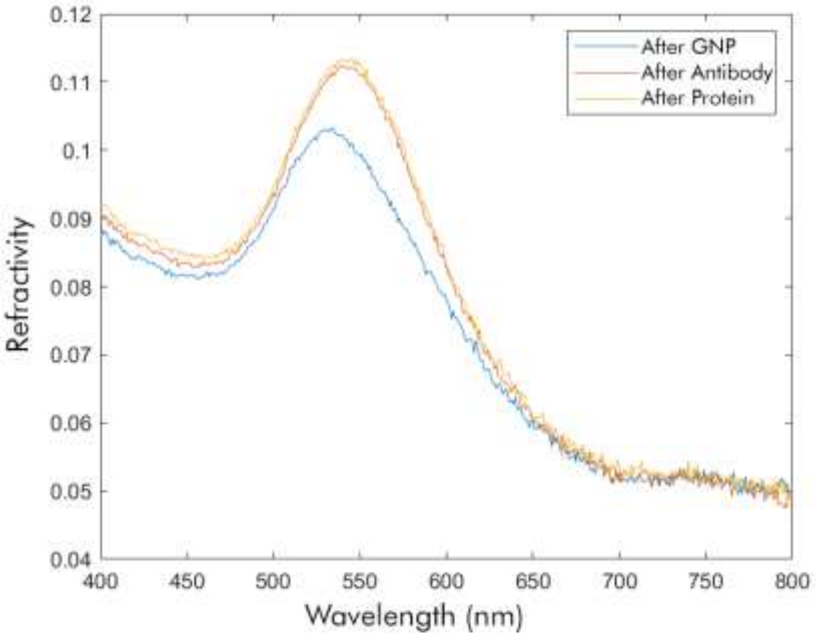

Figure 29. A sample graphic of LSPR measurements before and after Ab functionalization and after Ab-protein interaction.

Although it is unconventional for LSPR based sensor platforms where generally a wavelength shift is observed and utilized for sensing purposes; in here there was a significant difference and correlation between absorbance intensity differences of LSPR signals between the measurements before and after Ab-protein interaction. The shifts that were encountered in each sample concentration were analyzed and their related distributions can be seen in Figure 30. It is possible to see that there is a significant absorbance intensity difference after protein Ab interaction and iIt is evident that especially for concentration greater than 10 nM, wavelength shifts increase drastically. This indicates that the developed sensor system interacts with the protein, however a wavelength shift was not observable, most likely due to inefficiency of the sensor platform at its current state, therefore further optimization was done for the platform. Also it is important to note that the absorbance intensity changes due to protein Ab interactions are quite small and for higher sensitivity and resolution these intensity differences should be enhanced.

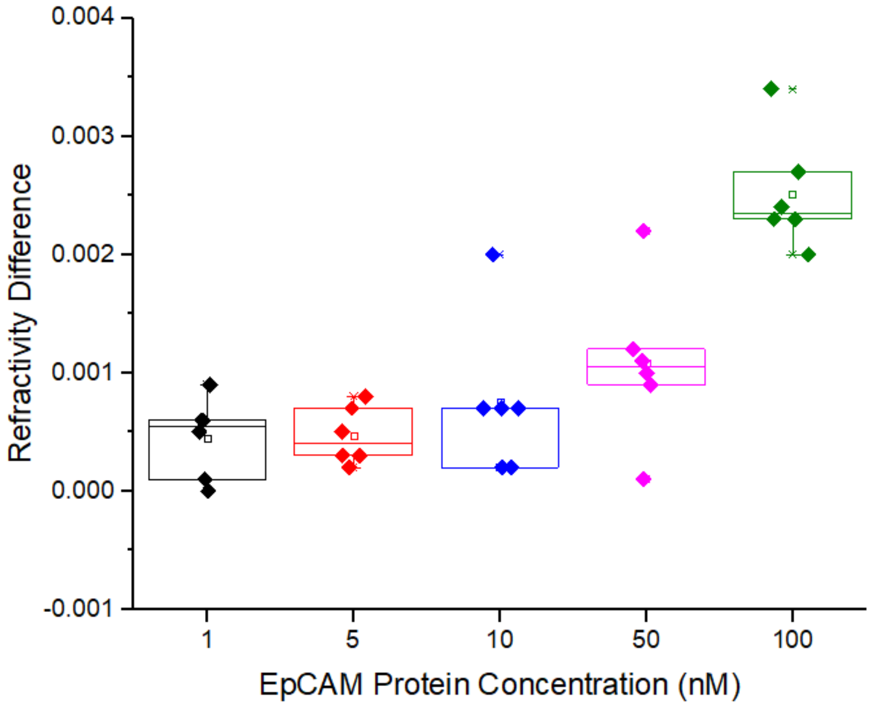

Figure 30. Intensity difference between LSPR measurements before and after EpCAM protein-Ab interaction.

On the other hand, the primary objective of this study was to visualize a wavelength shift, thereby enhancing the sensitivity of the LSPR sensor platform. To achieve this objective, comprehensive sensitivity enhancement studies were carried out. These studies were designed to meticulously evaluate the potential of the sensor platform in detecting minute changes in the refractive index, which is critical for achieving higher sensitivity. As part of these enhancement studies, first a detailed investigation into the dilution of Gold Nanoparticles (GNPs) was conducted. The GNP solution, which was prepared using the Turkevich method, was subjected to a series of dilution experiments. These dilutions were performed systematically with dilution factors of 2x, 5x, 10x, 25x, and 50x, in order to understand the impact of different concentrations on the immobilization process and subsequent sensor performance.

Prior to immobilization, the diluted GNP solutions were carefully prepared and characterized to ensure uniformity and reproducibility. The subsequent immobilization of GNPs onto the sensor surface was monitored and analyzed to determine the optimal dilution factor that yields the best sensitivity enhancement. The results of these immobilization experiments, which are crucial for understanding the relationship between GNP concentration and sensor sensitivity, are presented in detail below in Figure 31. This figure provides a visual representation of the immobilization efficiency across the different dilution factors, highlighting the impact of each dilution on the overall performance of the LSPR sensor platform.

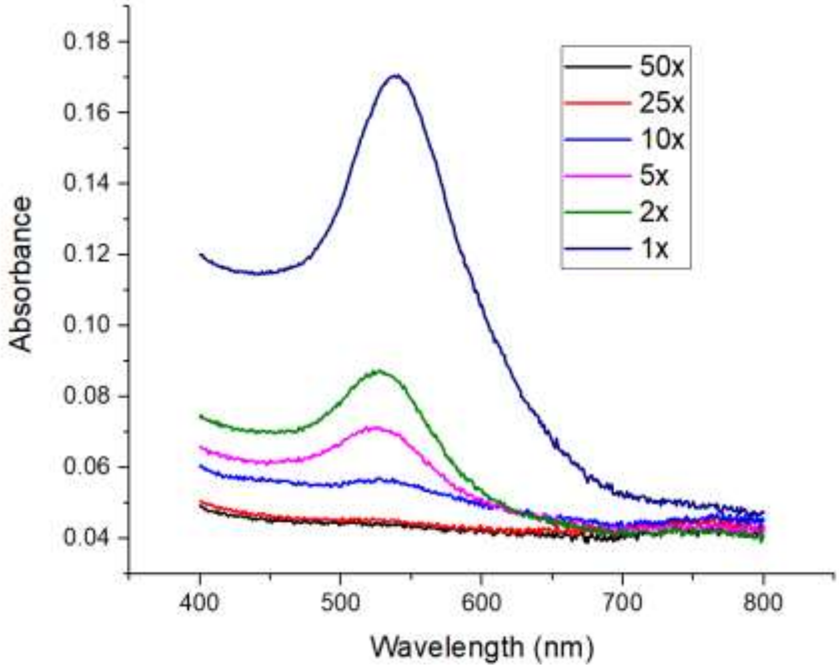

Figure 31. Decline of absorbance spectra peaks with increasing GNP dilution.

Later, the same procedure was carried out and BSA was used as a model protein again. However, higher dilution showed no coherent results and greater deviation. Hence, Ab concentrations were increased for higher sensitivity. Wavelength shift signal acquired by triplicated Ab concentration. There was no significant difference when compared to previous study in case of protein signal. On the other hand, the wavelength shift that was acquired after Ab functionalization was increased where the Ab concentration used previously showed a 11.5 ± 3.47 nm shift; increased Ab concentration showed a 15.83 ± 2.85 nm shift. It is evident that the platform was able to differentiate the difference between the initial Ab concentration (2µg/ml) and increased Ab concentration (6µg/ml). The sensitivity of the platform is highly dependent on the molecular size of target molecule; this is also supported by comparing results obtained by BSA protein study and EpCAM protein study; and also literature (Unser et al. 2015; Yoon and Kim 2008). This explains the visible shift with the increased Ab concentration which has relatively larger molecular size (150kDa) compared to BSA (66kDA).

The same study that has been carried out with EpCAM protein and anti-EpCAM Ab was reenacted with CD151 protein and anti-CD151 Ab. As expected, based on the previous experimentation there was close to no observable wavelength shift, however there was again a refractivity difference which is shown in Figure 32. In the case of CD151 protein and Ab interaction only significantly different signal was measured from the protein sample with 100nM.

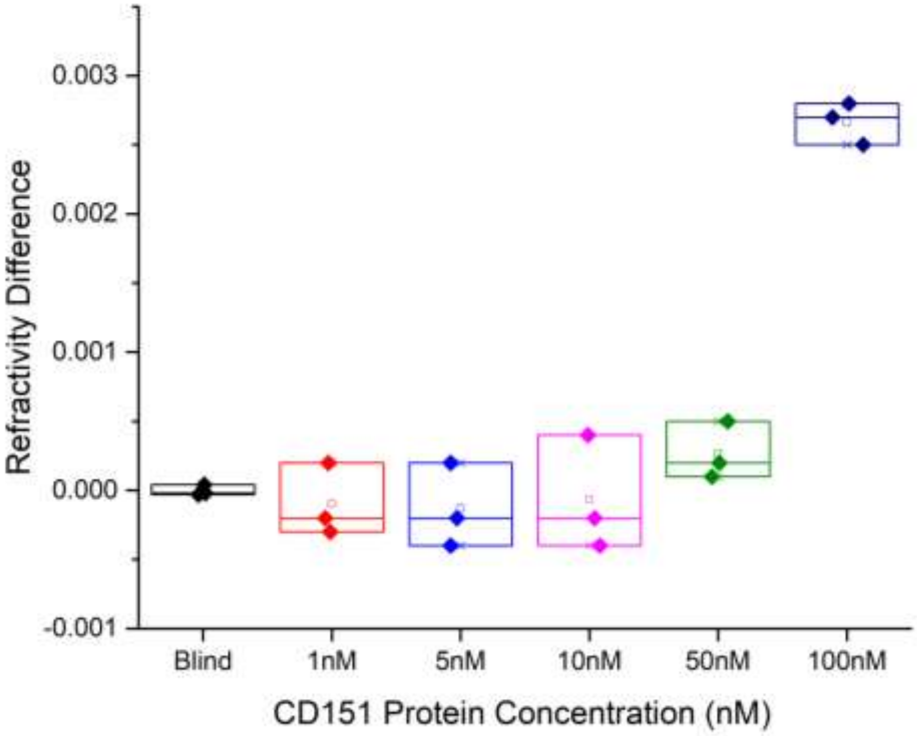

Figure 32. Intensity difference between LSPR measurements before and after CD151 protein-Ab interaction.

Overall Ab-antigen and GNP – sample interactions were successfully visualized. However, it’s been seen that a wavelength shift was not observable in case of molecules with smaller molecular masses (<60kDa). Hence a difference in absorbance was be analyzed as proposed by Englebienne. They proposed that even a kinetic measurement was possible by simply analyzing absorbance differences. A report shows that the absorbance difference of colloidal gold particles can be used to measure the apparent affinity of molecules (Englebienne 1998). Moreover, a more recent study used a very similar method to detect exosomes. Although their method included lithography techniques to fabricate single gold nano pillars, their analyses could find resourceful applications in current study. Their design validation was carried out by utilizing anti-CD63 antibodies and exosomes synthesized by MCF7 adenocarcinoma cell line. Exosome detection was manifested by increased nanostructure brightness resulting from the spectral shift; exosomes induced a 2 nm peak red shift as well as an overall increase in the scattered peak intensity (Raghu et al. 2018) . All these in mind, this approach of comparing absorbance intensities might not be necessary after experimenting and analyzing of *in-vitro* exosomes are carried out.

Table 3. LSPR results of *in-vitro* synthesized exosome isolated and then captured via various antibodies.

	A549		MRC5	
	CD81	**CD151**	**CD81**	**C151**
Absorbance Difference	0.002	0.002	0.002	0.002
Wavelength Shift	1.333	0.667	0.667	0.333

Table 3 shows the absorbance differences and wavelength shifts caused by exosome - Ab interactions for exosomes acquired from each cell line and with various antibodies as recognition elements. Ot was evident that the increase in sample particle size, from protein to exosome alone, did not provided sufficient increase in absorbance intensity differences. Hence, to be able to detect and distinguish cancerous and healthy exosomes it was apparent that a sensitivity enhancement was a necessity. In order to satisfy this necessity several plasmonic sensor platform enhancement techniques were utilized during the study which are detailed in the following parts.

3.2.6 Enhancement of Nanoparticles and Their Utilization in Sensor Platform

Herein, several synthesis and modification methodologies were employed for sensor sensitivity and resolution enhancement. Following part includes the results that were most promising in detail, and brief information of all NPs that were utilized at the end of it. Figure 33 summarizes the followed procedures for these NPs briefly.

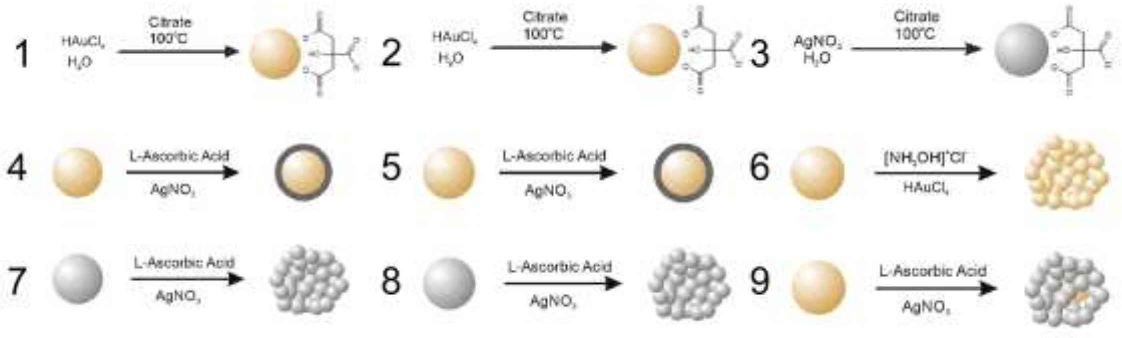

Figure 33. Summary of various NP synthesis procedures.

Briefly the methodologies consisted of:

1. GNP synthesis via modified Turkevich method as described in detail in part “2.2.1 Gold Nanoparticle Synthesis”
2. Silver Nanoparticle (SNP) synthesis via modified Turkevich method as described in detail in part “2.2.3 Silver Nanoparticle Synthesis
3. Core-Shell Gold-Silver NP synthesis with 50:50 silver to gold ratio utilizing the method described in the section “2.2.6 Core-Shell Nanoparticle Synthesis”

4. Core-Shell Gold-Silver NP synthesis with 70:30 silver to gold ratio utilizing the method described in the section “2.2.6 Core-Shell Nanoparticle Synthesis”
5. Gold Growth on Gold Nanoparticles as described in section “2.2.5 Nanoparticle Growth and Coating” for 4 min
6. Gold Growth on Gold Nanoparticles as described in section “2.2.5 Nanoparticle Growth and Coating” for 10 min
7. Consecutive Gold and Silver Growth on Gold Nanoparticles as described in section “2.2.5 Nanoparticle Growth and Coating” for
8. Silver Growth on Gold Nanoparticles as described in section “2.2.5 Nanoparticle Growth and Coating” for 10 min of gold followed by 30 min of silver
9. Utilizing Tyrosine as the reducing agent for synthesis of GNPs instead of citrate and for capping of GNPs as well

Silver Nanoparticle Synthesis

GNP utilization without any modification was discussed in the previous sections so that here SNP utilization is included first. Figure 34 describes the results acquired when SNPs were utilized instead of GNPs without any further modification. They were immobilized via PLL, functionalized by MUA modification and EDC/NHS protocol, then used for detection of BSA as a model protein as described before as done with GNPs in previous sections.

Figure 34 suggests that there is a significant and readable difference after protein sample. Even though, it is significant it was possible that detection of proteins with smaller molecular size or with smaller concentrations would prove ineffective with current state of the system. The acquired data was utilized to calculate wavelength shifts caused by protein-Ab interactions and are compared with other methodologies of enhancement at the end of this section. Current state of the LSPR-based biosensor platform, utilizing immobilized SNPs in place of GNPs, was able to provide wavelength shifts for detection.

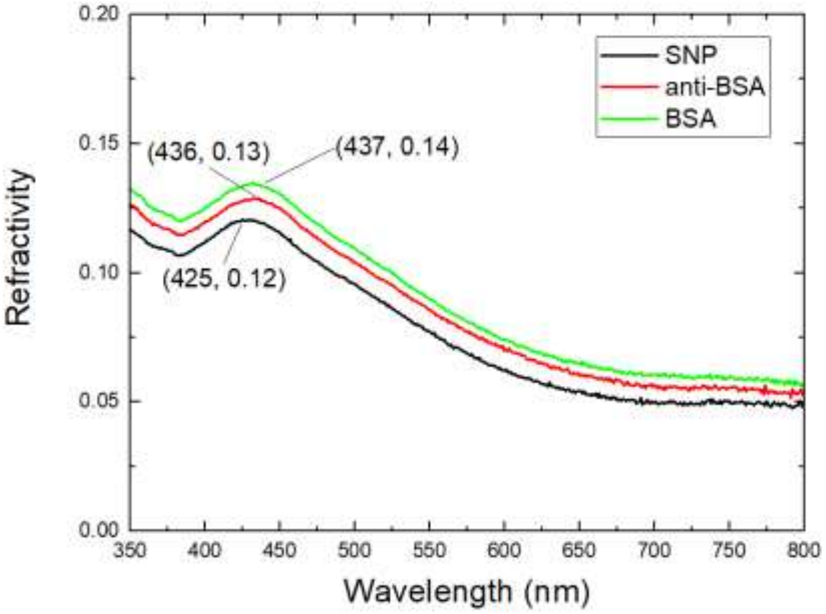

Figure 34. Mean absorbance peak of immobilized SNPs, SNPs with anti-BSA functionalization, and BSA anti-BSA interaction.

Gold-Silver Core-Shell Type Nanoparticle Synthesis

Core-Shell type nanoparticle synthesis was carried out next for enhancement of the LSPR sensor platform study. Silver-gold bimetallic nanoparticles were synthesized by the reaction that was started with GNP synthesis as described by Turkevich as described in the methods section “2.2.1 Gold Nanoparticle Synthesis”. Then, core-shell synthesis was carried out as given in the methods section. Figure 35 shows the absorbance spectrum of synthesized nanoparticles. With newly synthesized NPs immobilization onto wells were carried out with PLL and then MUA modification was done. Figure 35 shows the absorbance spectrums of both in comparison, and it indicates a successful immobilization and modification. The core-shell nanoparticles were then immobilized onto well plates via PLL linkage with success however MUA modification was ineffectual, so experimentation was ceased, and Ab functionalization and protein detection wasn’t carried out at all. A different approach was utilized for core-shell synthesis, as described in methods section. L-ascorbic acid instead of citrate was utilized as the reducing agent.

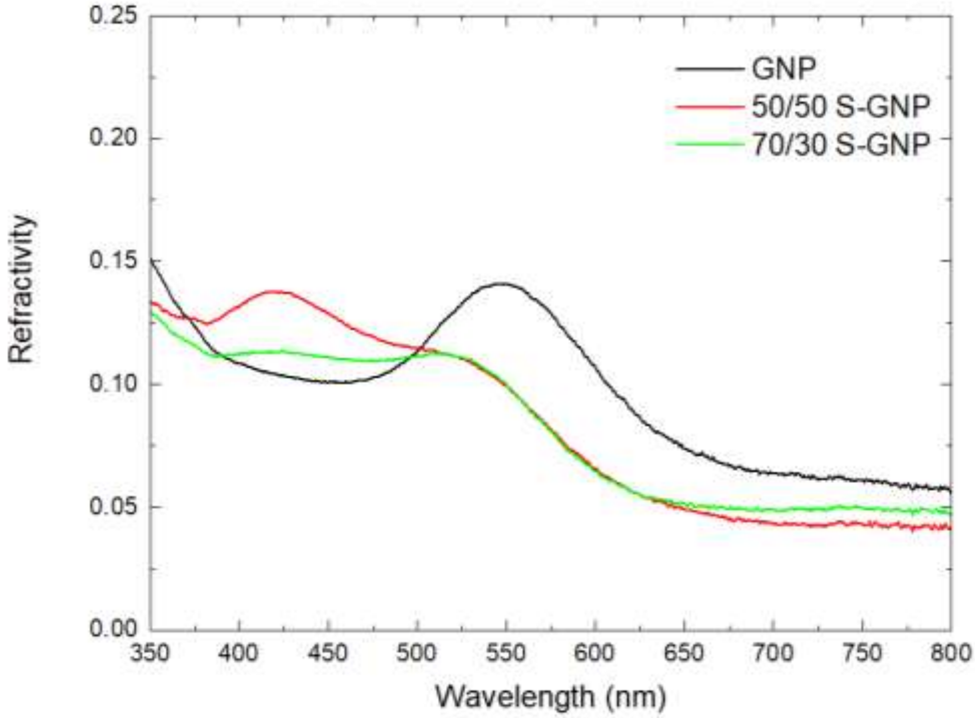

Figure 35. Core-Shell type Gold-Silver NP synthesis.

As seen in Figure 35 a secondary peak is formed when bimetallic NPs are synthesized. The absorption spectra of metallic nanoparticles, such as gold and silver, are primarily influenced by the collective oscillation of conduction electrons. This phenomenon results in a characteristic peak in the UV-vis spectrum. For individual gold or silver nanoparticles, the SPR occurs at a specific wavelength, leading to a single absorbance peak. When it comes to gold-silver core-shell structures the presence of two different metals introduces additional complexity to the electronic structure and plasmonic behavior. The combination of gold and silver in a core-shell structure can result in multiple SPR peaks due to the different properties of each metal (Dikkumbura et al. 2021; Steinbrück et al. 2011).

In a core-shell nanoparticle, both the core and the shell contribute to the overall plasmonic response. Interactions between the core and shell, such as charge transfer and hybridization of electronic states, can give rise to new absorption features. The multiple peaks in the UV-vis spectrum of core-shell nanoparticles are a consequence of this interplay between the plasmonic properties of the individual metals and their combined effects in the composite structure (Borah and Verbruggen 2020; Sood et al. 2016). After the synthesis NPs were immobilized using the same methodology and Ab functionalization was carried out as described. BSA detection was done similar to the previous studies. Results can be seen in Figure 36.

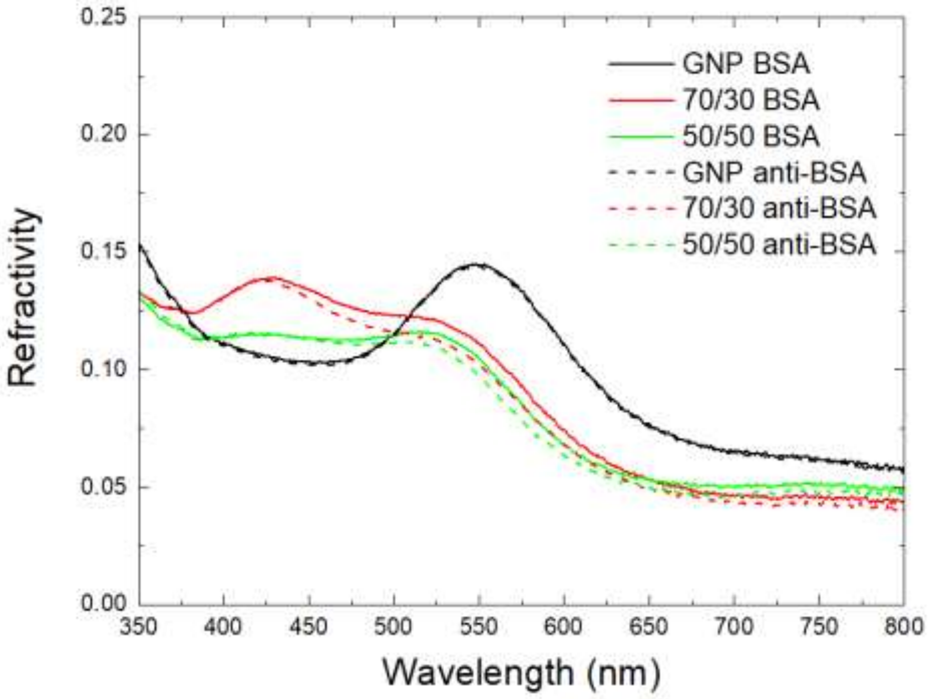

Figure 36. BSA detection via Core-Shell Gold-Silver NPs and GNPs.

As seen in Figure 36 both 70:30 and 50:50 core-shell ratio NPs had greater wavelength shifts when compared to GNPs.

Gold Growth on immobilized GNP Study

GNP growth was carried out in wells and Ab-antigen interaction was investigated through it. For this purpose 15 min growth was carried out as described in methods section; in 1 min intervals and growth reaction was ceased at each min. Figure 37 shows the absorbance peak intensity increase and wavelength shift during the growth reaction. As shown in the figure it was quite possible to control the amount of growth by ceasing the growth reaction at the desired point.

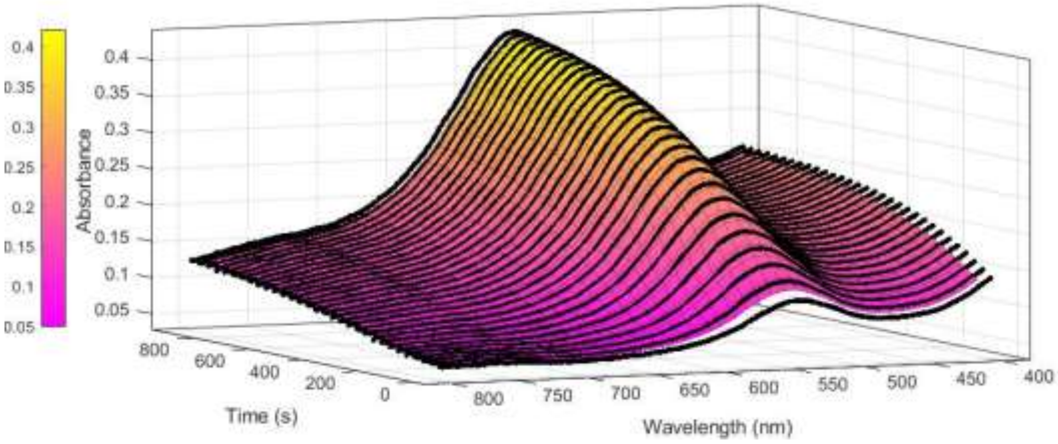

Figure 37. GNP growth UV-Vis spectra of each growth period.

Afterwards grown GNPs were functionalized with anti-BSA and BSA detection was carried out as a model. Detection was carried out using 10 µM BSA solutions with each well and the observed wavelength shift was the largest when the growth reached 4 min. Results can be seen in Table 6.

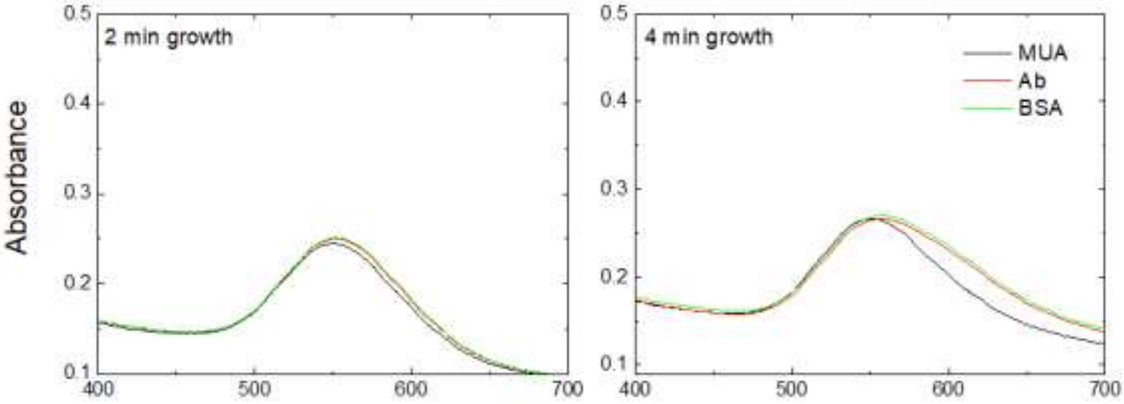

Figure 38. Acquired UV-Vis spectrum during the BSA detection study utilizing g-GNPs

As after 4 min of growth, there was a significant difference in the shifts; using increased growth time seemed unnecessary though readily providing higher wavelength shifts compared to GNPs without growth. Further experimentation was carried out with

4 min grown *g*-GNPS, in order to compare with GNPs without modification more thoroughly.

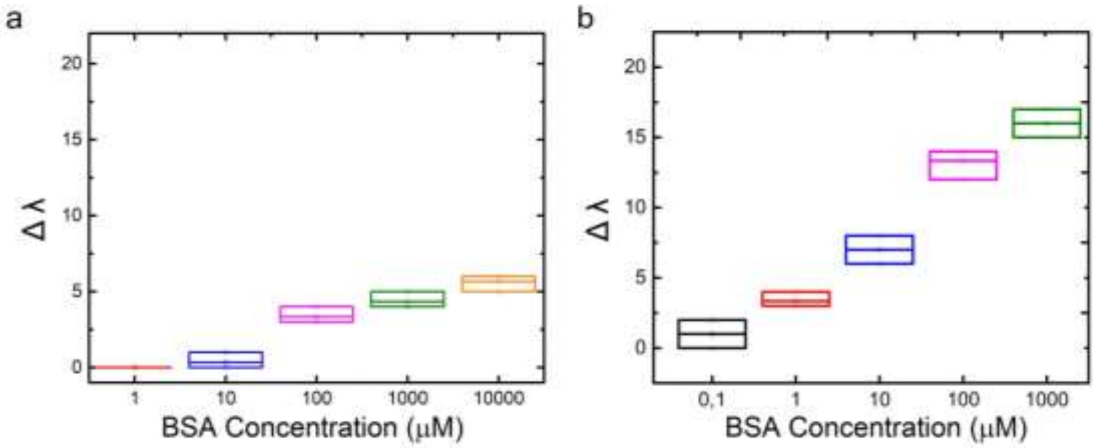

Figure 39. Wavelength shift of absorbance maximum (Δ λ) values for various concentrations of BSA, a) Utilizing i-GNPs b) Utilizing g-GNPs.

Figure 39 depicts the obtained data, where *i*-GNPs served as controls to assess the sensitivity enhancement resulting from the gold growth procedure. On the other hand 4 min grown *g*-GNP were utilized for detection. A correlation was identified between BSA concentrations and Δλ values. Notably, a higher Δλ was observed when *g*-GNPs were employed in comparison to *i*-GNPs. Data linearization was performed to construct a calibration curve and determine sensory characteristics.

Furthermore, The acquired results reveal a dynamic working range of 0.344 μM – 1mM, comparable to commercial kits with similar ranges. Additionally, the calculated Limit of Detection (LoD) value (0.344 μM) closely aligns with the widely used BCA protein determination technique (0.301μM) (Khamehchian et al. 2008; BioTek Instruments 2021).

Silver Growth on Immobilized GNP Study

Next, silver growth on immobilized GNPs was carried out with various methods. Firstly, the method that has been used on a previous study for GNP growth was intended, 10 mM hydroxylamine hydrochloride ($[NH_3OH]^+Cl^-$) solution of was prepared and 80 µl of it was added into GNP immobilized wells at the same time with 20 µl, 7.5mM $AgNO_3$. Real time absorbance spectrum was taken every 4 mi, and the results were given in the figures below, namely Figure 40 and Figure 41. The same procedure is followed with using 20mM L-ascorbic acid solution of instead of hydroxylamine hydrochloride and results were given in the figure below.

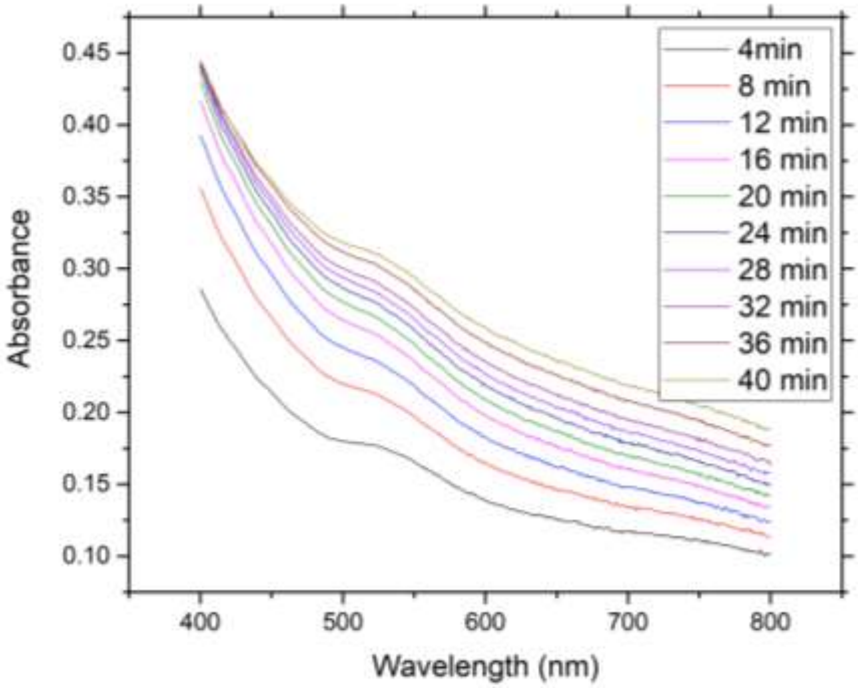

Figure 40. Ag growth on immobilized GNPs with $[NH_3OH]^+Cl^-$.

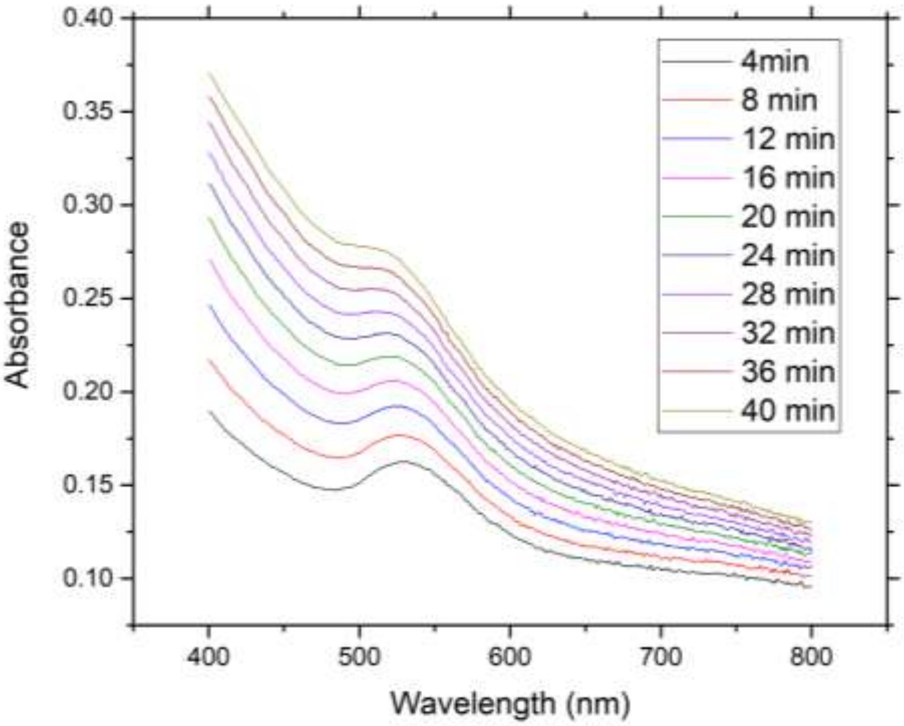

Figure 41. Ag growth on immobilized GNPs with L-Ascorbic Acid

Compared to Ascorbic acid $[NH_3OH]^+Cl^-$ showed a faster reaction rate however after the reaction is terminated and wells were washed L-Ascorbic Acid appeared to be the better option in this procedure.

Literature suggests that silver coating on Gold Nanoparticles (GNPs) can be identified by the presence of a second absorbance peak around 430 nm (Malassis et al. 2016). This characteristic peak is indicative of the successful deposition of silver onto the surface of GNPs, providing a reliable spectroscopic marker for the confirmation of silver coating (Malassis et al. 2016). In our study, the closest results to this expected absorbance peak were obtained by employing a method that utilized L-Ascorbic Acid as a reducing agent. Given its promising outcomes, further experimentation was carried out using this method to optimize the reaction conditions, particularly focusing on the reaction time. Following Figure 42 shows absorbance spectrum results for 8 separate reaction times (5, 10, 15, 20, 25, 30, 35, and 40 mis). These results were examined to discern the optimal conditions that maximize the characteristic silver peak, thus confirming the successful coating process.

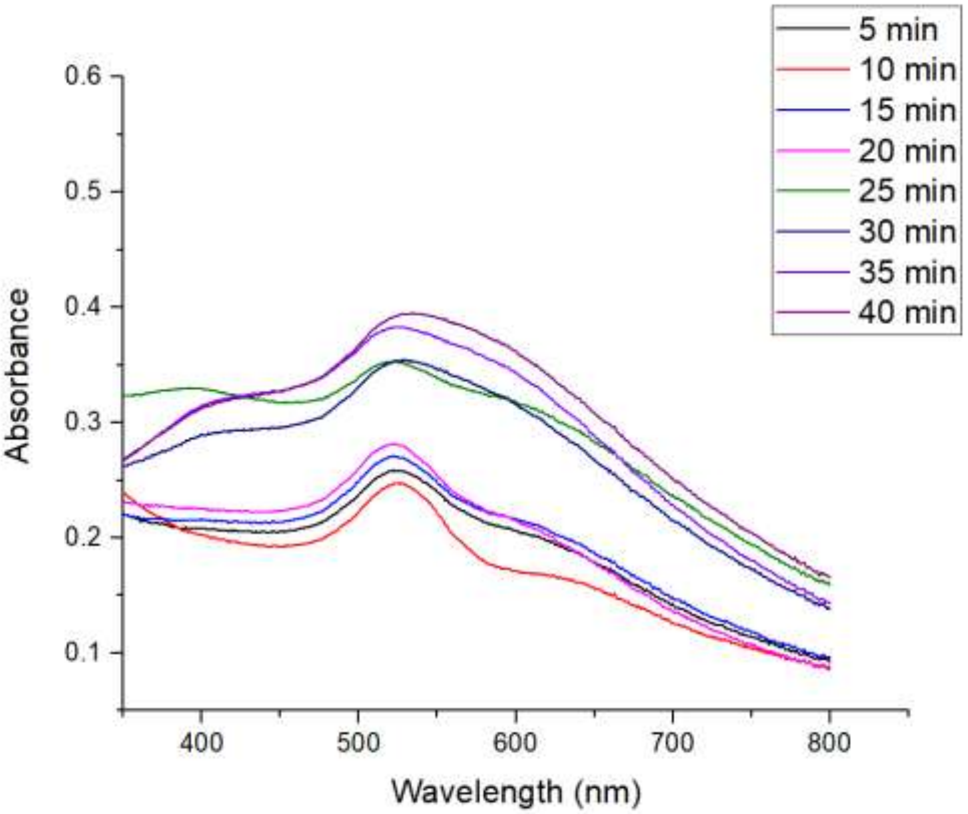

Figure 42. Silver growth on GNPs with various time frames.

As seen in Figure 42 there is a drastic change in spectrum after 25 minutes of silver growth. The detailed absorbance spectrum analysis presented here underscores the importance of reaction time optimization in achieving the desired silver coating on GNPs. The results highlight the potential of the L-Ascorbic Acid method in producing consistent and reliable silver-coated nanoparticles, paving the way for further advancements in nanotechnology. Also, growth slows down after minute 35. Hence, these two reaction time values were investigated further for detection study. First MUA functionalization was carried out. After MUA modification, for 35 min grown Ag-GNPs showed ~17 nm wavelength shift and 25 min grown Ag-GNPs showed ~12 nm wavelength shift. Since a higher shift promises a greater sensitivity, further applications were carried out utilizing 35 minutes of silver growth on GNPs. EpCAM detection was studied to investigate the sensitivity and resolution of developed platform that utilizes silver growth on GNPs. Figure 43 demonstrates the UV-Vis spectrum measurements during the application.

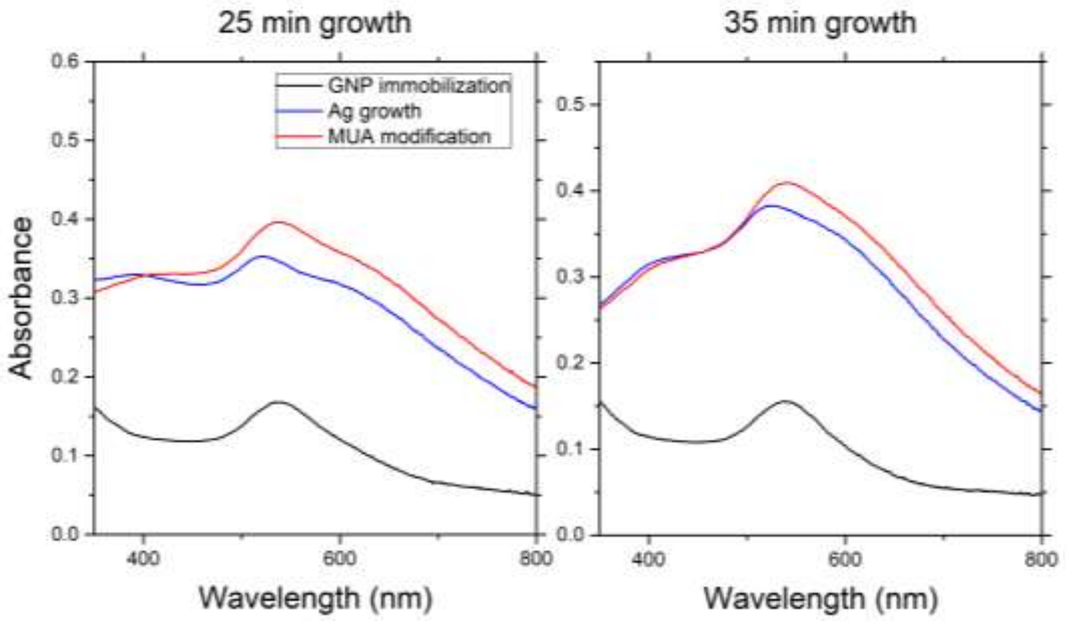

Figure 43. Silver growth on GNP; MUA functionalization comparison of 25 and 35 min reaction times.

EpCAM protein detection study was reenacted with silver grown immobilized GNPs and no wavelength shift was observed but greater absorbance differences were measured when compared to only GNP utilization as seen in Figure 44. Specifically, for protein detection assays, it was found that reaction times beyond 35 minutes did not result in higher resolution. This is an important consideration for practical applications, where efficiency and efficacy are paramount. The optimized reaction time not only enhances the performance of the sensor platform but also ensures that the process remains cost-effective and time-efficient.Conversely, the 5-fold increase in absorbance intensity, coupled with the formation of the secondary peak, indicates a substantial enhancement in the resolution of the developed sensor platform. This significant improvement aligns with the findings suggested by literature for bimetallic nanoparticles (Borah and Verbruggen 2020; Eskiköy Bayraktepe, Yıldız, and Yazan 2023). The secondary absorbance peak around 430 nm, characteristic of silver coating, not only validates the successful deposition of silver but also underscores the enhanced optical properties of the bimetallic NPs. The increased absorbance intensity directly correlates with improved sensitivity in detecting proteins, making the sensor platform more robust and reliable. This enhancement is particularly valuable in applications where precise and accurate detection of low-abundance proteins is critical. The secondary peak formation, indicative of successful silver coating, further reinforces the enhanced performance of the sensor, providing a higher resolution that is crucial for detailed and accurate analyses.

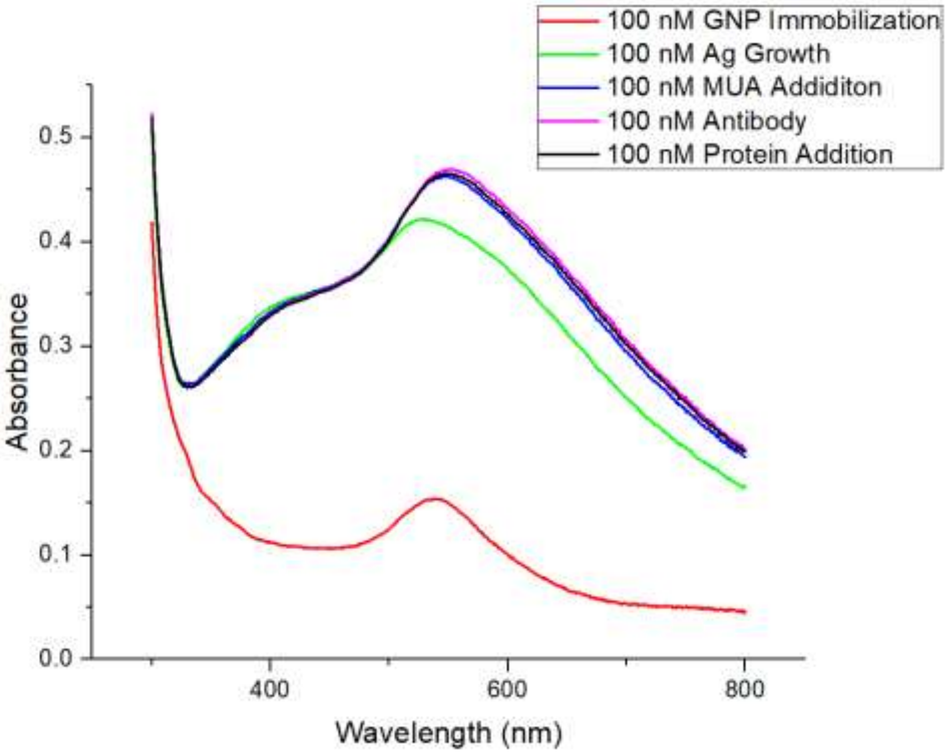

Figure 44. EpCAM detection study with silver grown on GNP for 25 min and utilizing L-ascorbic acid as the reducing agent.

Absorbance differences for the experiment sets that are shown in Figure 44 can be seen in detail in the following Table 4. As represented in the table, there was a clear correlation between the detected protein concentrations in the sample and the read absorbance difference before and after the introduction of the samples into the developed sensor platform. However, said absorbance differences were not large enough for the sensitivity of the system that was aimed at the start of this study. The difference here is better described in the next section where all the studied NPs that were either synthesized or modified by various methodologies are compared in terms of their platform sensitivity enhancement capabilities.

Table 4. EpCAM detection results with LSPR sensor platform.

Absorbance Difference	**EpCAM Concentration (nM)**
0.00205	6.25
0.0021	12.5
0.0026	25
0.0051	50
0.0081	100

Although no wavelength shift was observed after protein addition absorbance difference was increased five-fold compared to GNPs and a wavelength shift of ~17 nm was seen between Ag growth and MUA modification, whereas in previous studies with only *i*-GNPs it was around ~ 3 nm.

Comparison of the Enhancement Efficiency of Utilized Methods

Various NPs were synthesized or prepared by modification and utilized for BSA detection as a model study so far. For betterment of sensor sensitivity and widening of working range several NPs were utilized in a single experimentation set to detect BSA. NPs were immobilized and functionalized with anti-BSA Ab; trails were run in six replications. Utilized NPs were GNPs, GNPs with 10min gold growth, GNPs with 4 min gold growth, GNPs with 20 min silver growth (after immobilization), GNPs with 30 min silver growth (after immobilization), GNPs with 4 min gold growth followed by 20 min silver growth, GNPs with 10 min gold growth followed by 20 min silver growths, GNPs with 4 min gold growth followed by 30 min silver growth, GNPs with 10 min gold growth followed by 30 min silver growths, GNPs with 4 min gold 20 min silver and another 4 min of gold growth, Core-Shell S-GNPs (7:3 v/v), Core-Shell S-GNPs (1:1 v/v), SNPs, SNPs with 4 min gold growths, TYR capped GNPs. UV-vis spectrum of all the NPs; synthesized or modified during the study can be seen in Figure 45 and Figure 46.

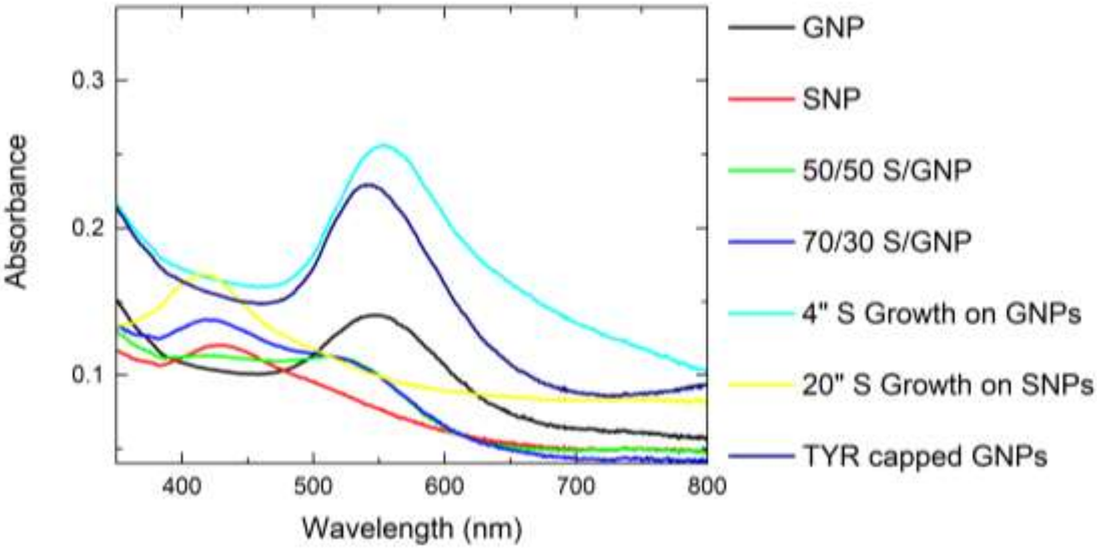

Figure 45. UV-Vis spectrum of synthesized NPs, Gold, Silver, Core-Shell S-GNPs (50/50 v/v), Core-Shell S-GNPs (70/30 v/v), 4 min grown GNPs, 20 min silver growth on SNPs, and Tyrosine capped GNPs instead of citrate.

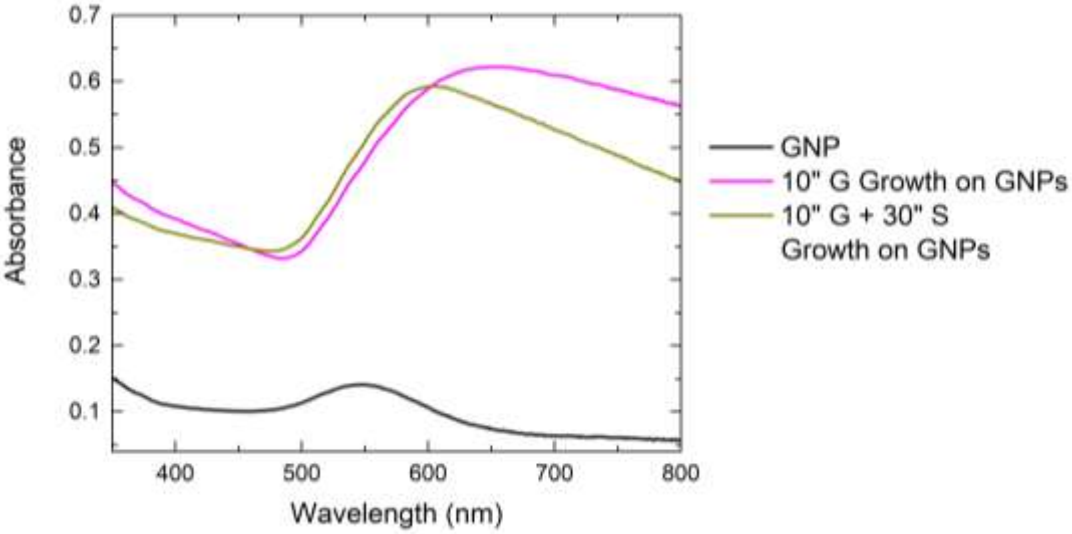

Figure 46. UV-Vis spectrum of synthesized NPs, Gold, 10 min grown GNPs, and GNPs with 10 min gold 30 min silver growth.

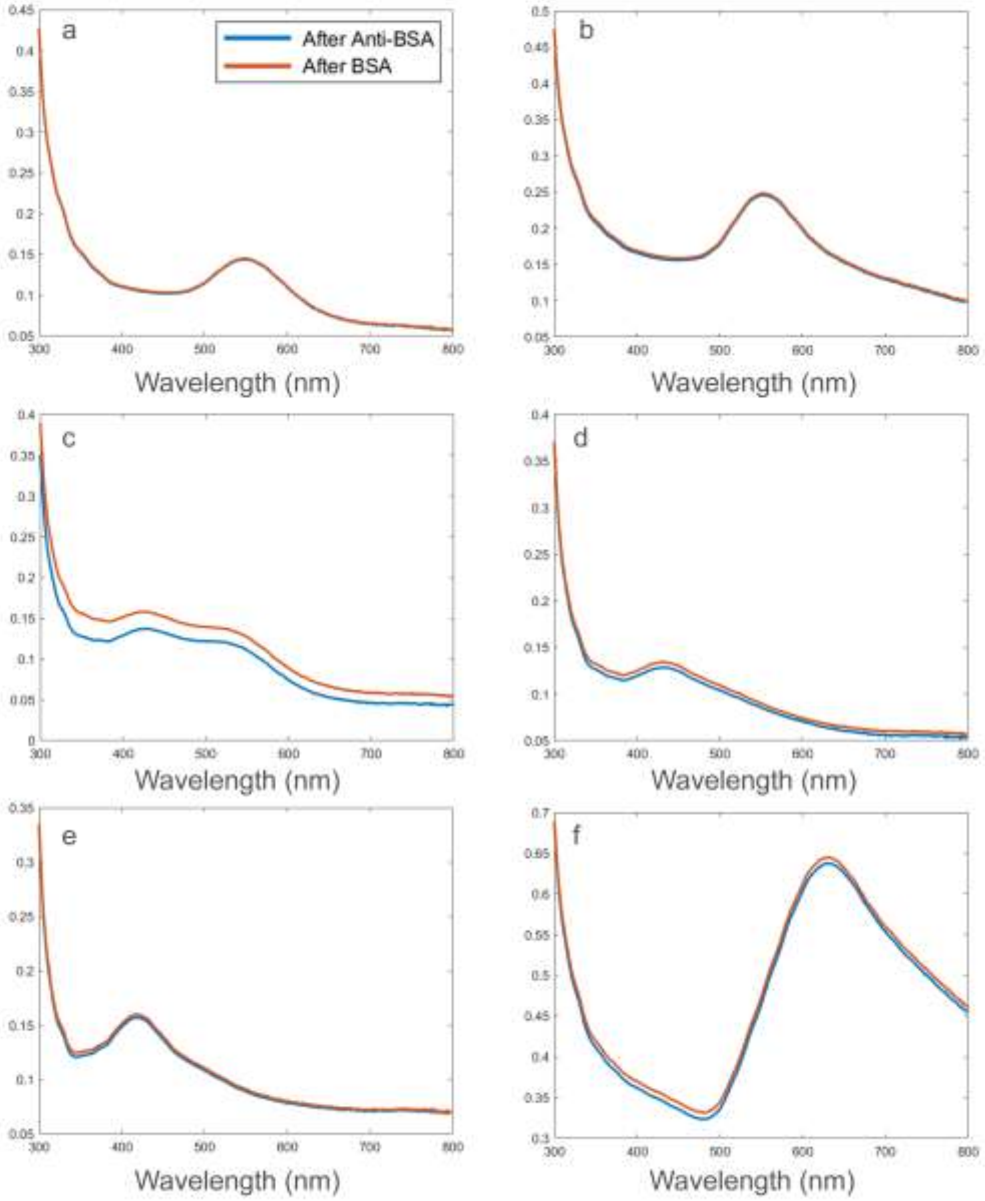

Figure 47. Absorbance spectrums of LSPR sensor platform prepared with a) Conventional GNPs; b) 4 min grown GNPs; c) Core-Shell S-GNPs (70/30 v/v); d) 20 min silver growth on SNPs; e) 30 min silver growth on SNPs; f) GNPs with 4 min gold 20 min silver and another 4 min of gold growth.

As seen in Figure 45 and 46, each fabricated NP showed a characteristic and specific peak intensity and position. While this phenomenon provided various plasmonic behaviors it also affected the sensory characteristics of LSPR platforms that were prepared by utilizing different NPs. Results of BSA detection study with various NPs can be seen in the above Figure 47.

As shown in Figure 48, the highest shift was encountered in the core-shell NPs that are synthesized in suspension. The second best was g-GNPs followed by the Silver grown on immobilized GNPs. Moreover, Figure 48 is the representative for the most promising results of six replications of each 15 different NP samples and conventional GNPs as control.

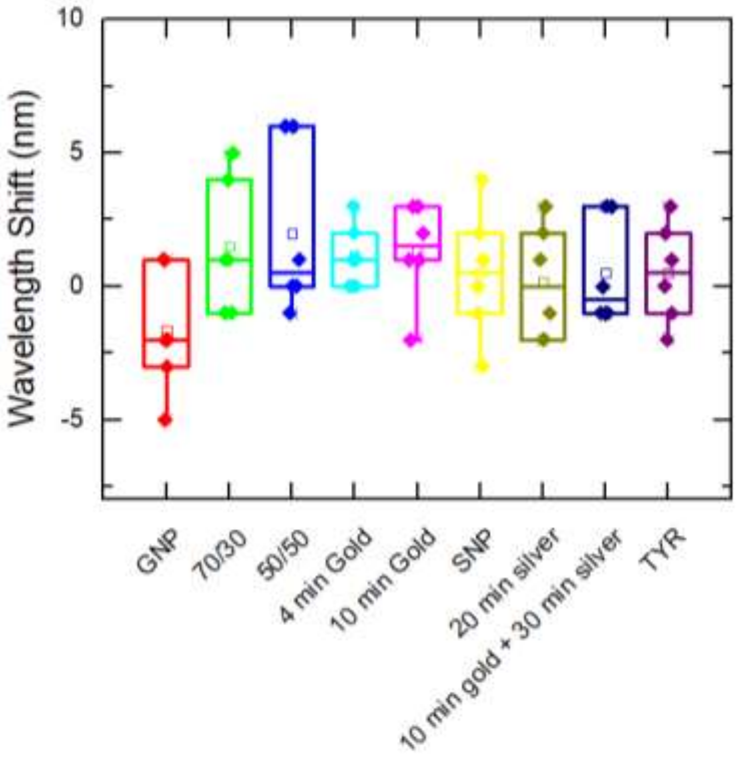

Figure 48. Wavelength shifts caused by protein-Ab interaction in LSPR sensor platforms prepared with various NPs.

Consequently, core-shell gold-silver NPs showed greater sensitivity; hence optimization of their synthesis, modification, and functionalization was carried out next.

Gold to Silver Volume Ratio Optimization

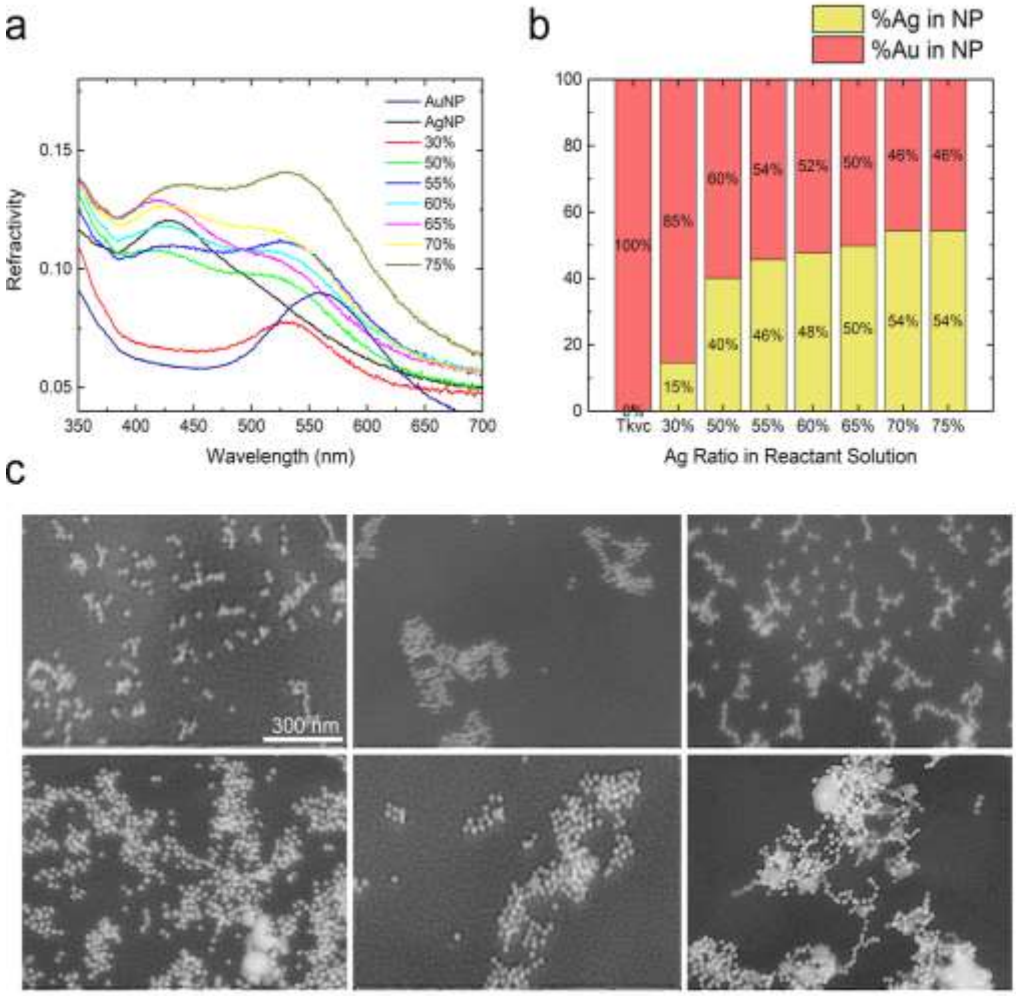

Figure 49. Characterization of NPs with various core to shell ratios; UV-Vis spectra (a), EDX analyses (b), and SEM images (c).

Optimization for core-shell NP based sensor system was carried out due to its greater performance in the previous part of this study and as a first step the gold-silver ratio was optimized. Figure 49 shows NPs that were synthesized via different volumetric ratios of GNPs and AgNO3. Characterization results with both spectrophotometric measurements and EDX analyses showed that there is a saturation ratio in between 60:40 and 70:30 silver to gold ratio. All synthesized NPs were used for detection studies next utilizing BSA as a model protein. Comparison of most notable result can be seen in the figure below. As seen in Figure 50 core-shell NPs between 60:40 and 70:30 silver/GNP ratio had higher shifts with addition of anti-BSA and BSA. Compared to GNPs there is a significant increase in sensitivity of the system.

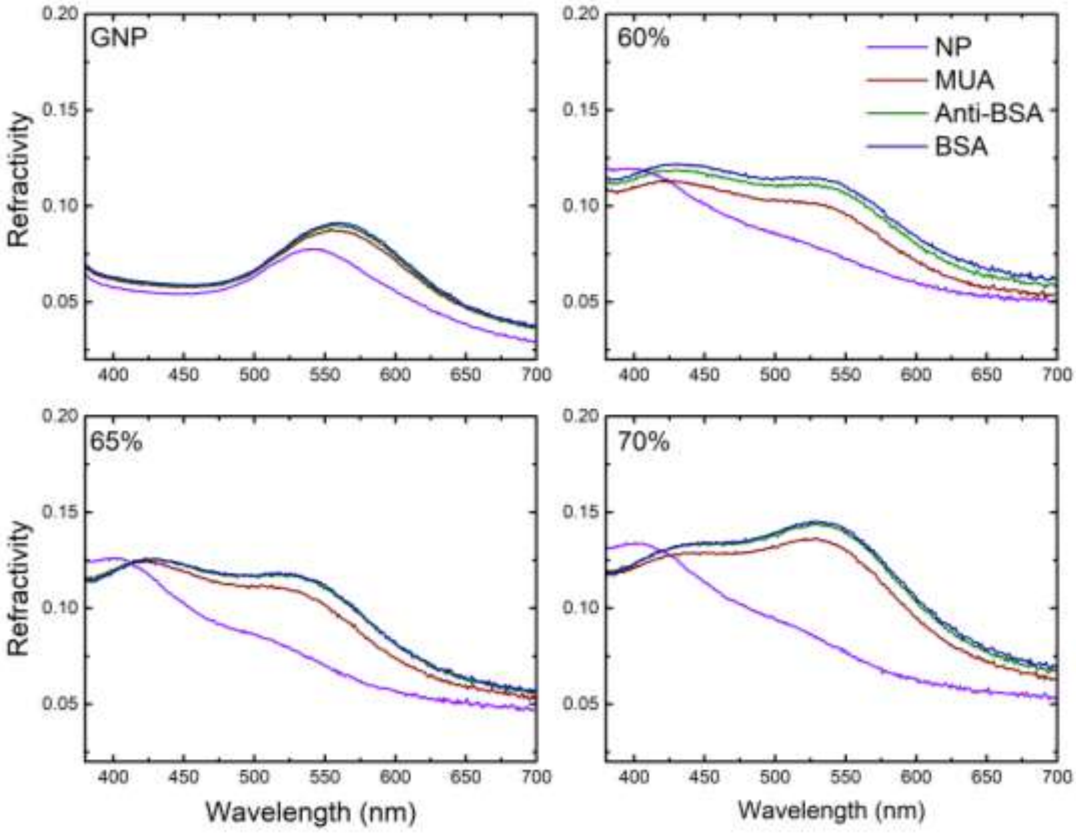

Figure 50. Wavelength shifts of core-shell NPs that showed significant signals, compared to conventionally synthesized GNPs.

Although a significant wavelength shift was observed, the absorbance intensity was low, and a higher absorbance intensity was favorable for further applications hence an optimization of reactant concentration was carried out with 60:40 silver to gold ratio. Reactant concentrations that were utilized in the previous step of the study were utilized for BSA detection too. As expected, a correlated increase in intensity was observed with increasing NP concentration. As seen in Figure 51 doubled reactant concentration showed a slightly greater wavelength shift. It can also be said that no significant difference is visible in intensity after immobilization for higher than doubled reactant concentration. Moreover, a tertiary peak was observed in the higher reactant concentrations at ~650 nm (J. He, Wu, and Sun 2019) which may indicate aggregation. Lastly, the characteristic GNP peak has started to be visible only as a shoulder after increasing the reactant concentrations tripled, the details of these analyses can be found in Figure 51.

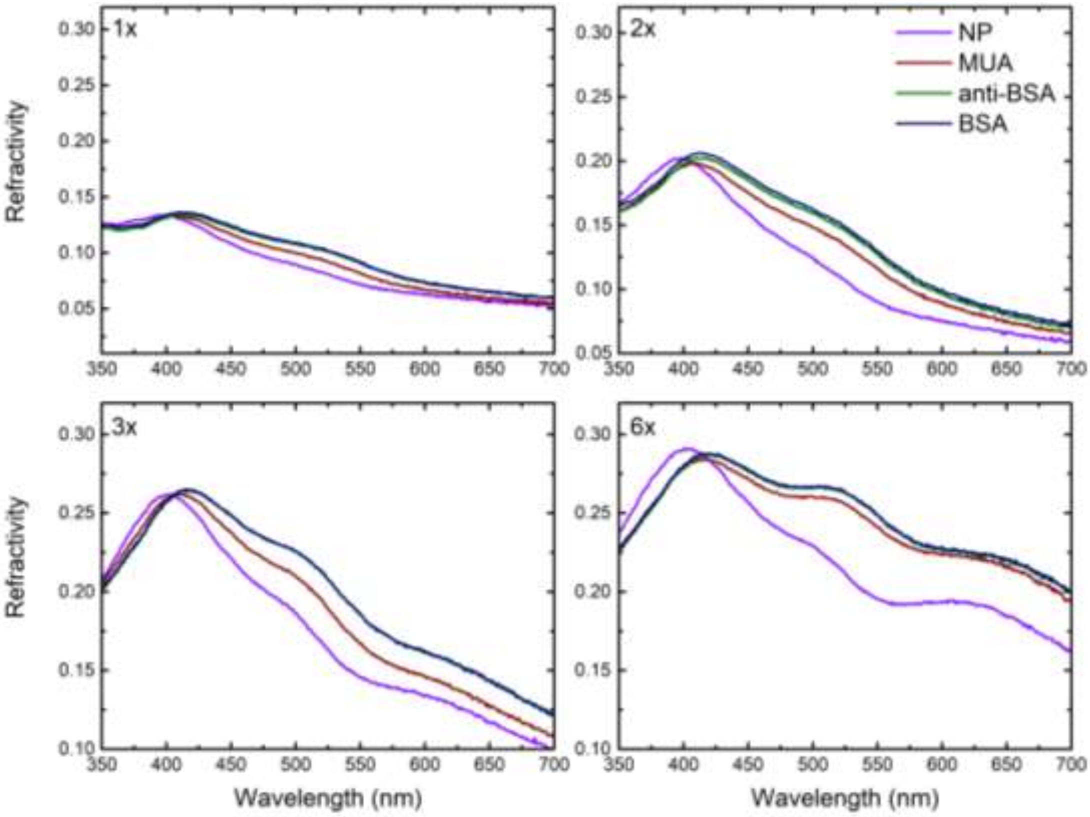

Figure 51. Model protein detection with core-shell NPs that were synthesized using various reactant concentrations.

Afterwards, the ratio of gold and silver was analyzed in synthesized NPs, this investigation was carried out to observe whether the increase in reactant concentrations effect the shell*-core ratio or not. It was apparent that the ratio was maintained at a constant level with increasing reactant concentration which was verified via EDX analyses.

Considering both the absorbance intensity increase not significantly changing after doubled concentration, formation of a tertiary peak at higher concentrations, and EDX results; doubled reactant concentration was utilized in the remainder of the study for higher intensity and very low chance of aggregation of NPs in long term storage.

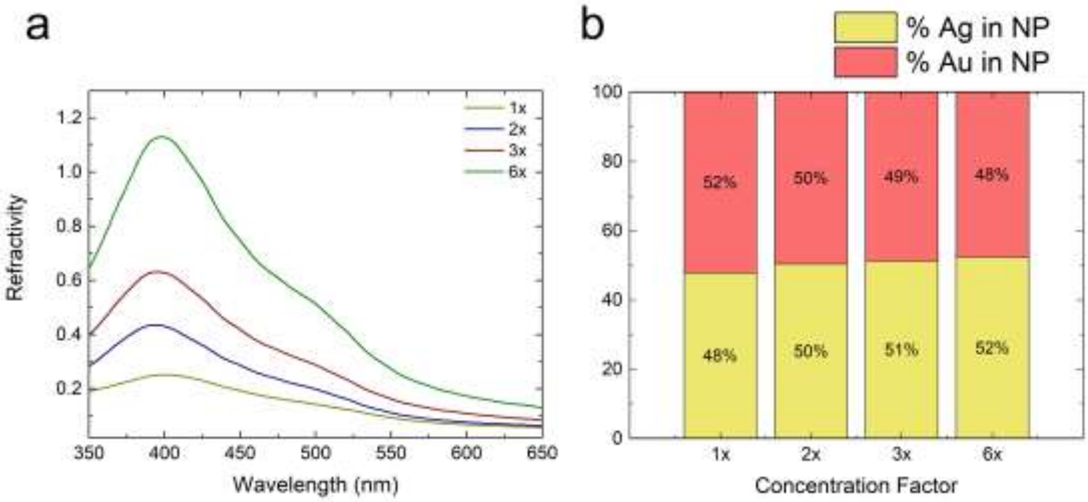

Figure 52. Characterization of core-shell NPs with various reactant dilution rates; UV-Vis spectra (a), and EDX analyses (b).

MUA Concentration Optimization for Core-Shell NPs

Optimization was the MUA concentration was carried out next, with the intention of decreasing the peak caused by MUA functionalization to increase any possible shifts that would derive from addition of anti-BSA and interactions between the anti-BSA and BSA. Figure 53 below shows the MUA peaks for both 60:40 and 70:30 silver to GNP ratios. As seen in Figure 53, addition of MUA causes a red shift in the peak that’s around 530 nm wavelength. It is also evident that with increased MUA concentrations there was a significant increase in the red shift of wavelengths.

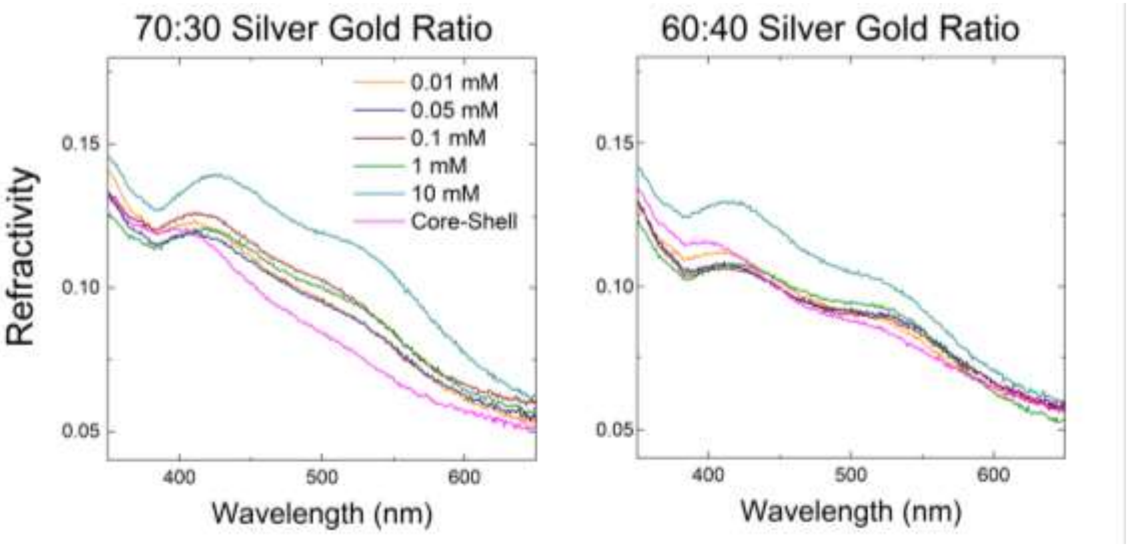

Figure 53. Absorbance spectrum of LSPR sensor platforms prepared via utilizing various concentrations of MUA.

The system was tested for its capability to detect BSA using various concentrations of MUA, and results can be seen in Figure 54. These results were instrumental in determining the optimal conditions for enhancing the sensitivity of the system to the Ab-BSA interaction. It was observed that decreasing the MUA concentration below 10 mM significantly increased the sensitivity of the sensor. This sensitivity enhancement was particularly notable, as it suggests that lower MUA concentrations are more effective in facilitating the interaction between antibodies and BSA, leading to more pronounced signal changes.

In the context of different volume ratios, the 60:40 v/v ratio was of particular interest. Within this ratio, no significant change in the signal was observed for a MUA concentration of 1 mM. However, the most substantial shift in signal was detected at a MUA concentration of 0.1 mM for the 60:40 v/v ratio. This indicates that lower concentrations of MUA, specifically 0.1 mM, are more conducive to achieving higher sensitivity in the sensor's response to BSA. Moreover, the 60:40 volume ratio not only showed a more distinguished peak but also exhibited a higher shift for the same BSA concentration compared to other volume ratios. This more pronounced peak and higher shift highlight the effectiveness of the 60:40 volume ratio in enhancing the sensitivity and resolution of the sensor platform. Based on these findings, the remainder of the study was conducted using the 60:40 volume ratio and a MUA concentration of 0.1 mM.

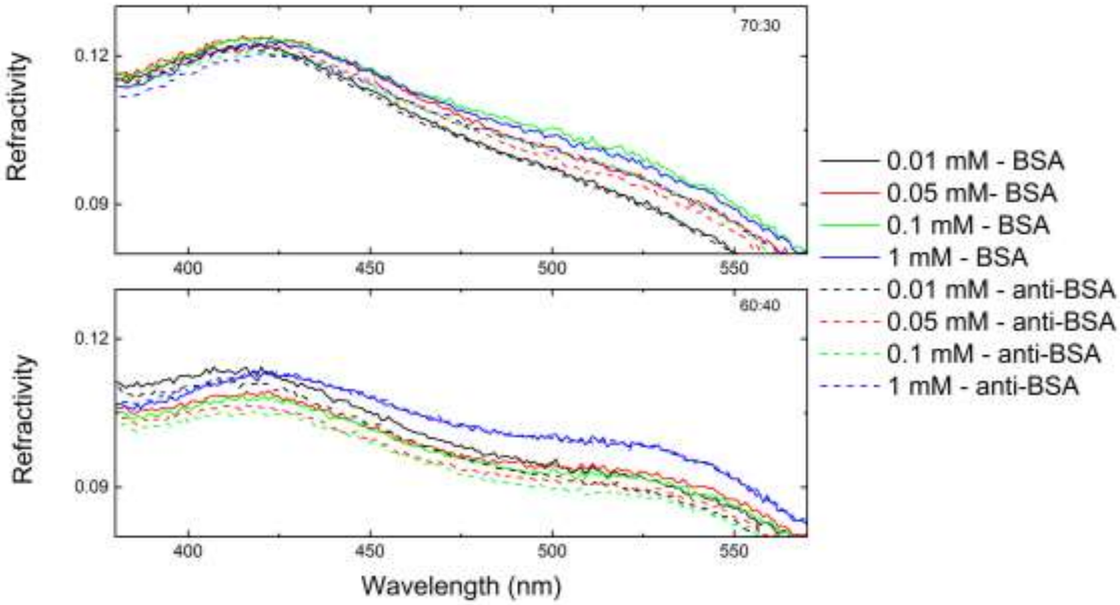

Figure 54. Wavelength shift after protein Ab interactions on platforms prepared with various MUA concentrations.

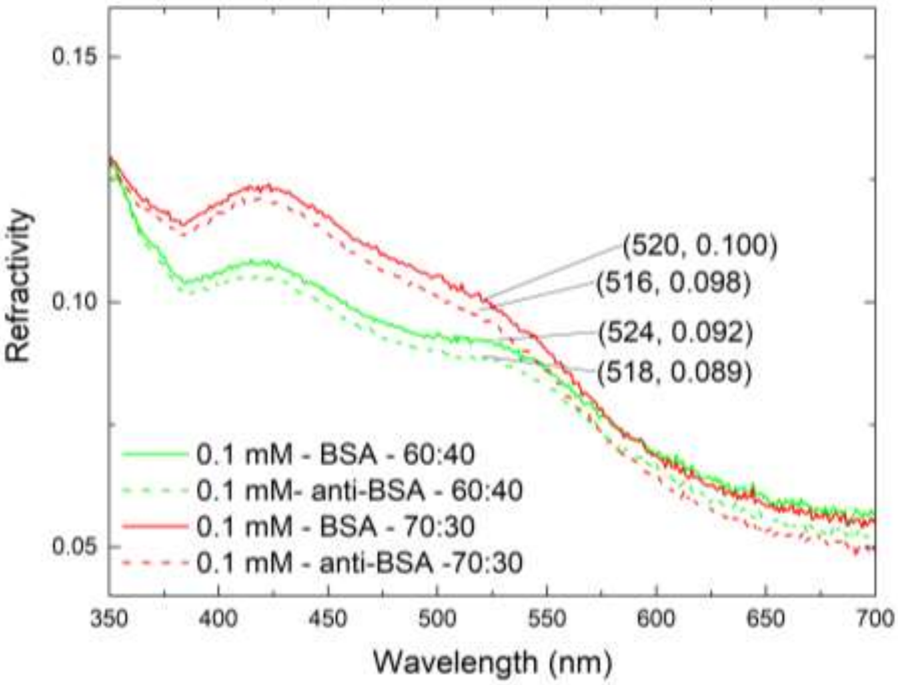

Figure 55. One on one comparison of 60:40 and 70:30 volume ratio core-shell NPs prepared via 0.1 mM MUA.

Further analyses of the acquired signals were carried out through a meticulous deconvolution of peaks and an in-depth, peak-by-peak investigation of the spectrums. This approach was essential for accurately interpreting the complex spectral data and extracting meaningful insights about the interaction between the nanoparticles and the biomolecules. The following figures present the comprehensive results of the peak deconvolution analyses specifically conducted for the 60:40 silver to gold volume ratio core-shell nanoparticles (NPs). These core-shell NPs were chosen due to their enhanced optical properties, which are critical for achieving high sensitivity in biosensing applications.

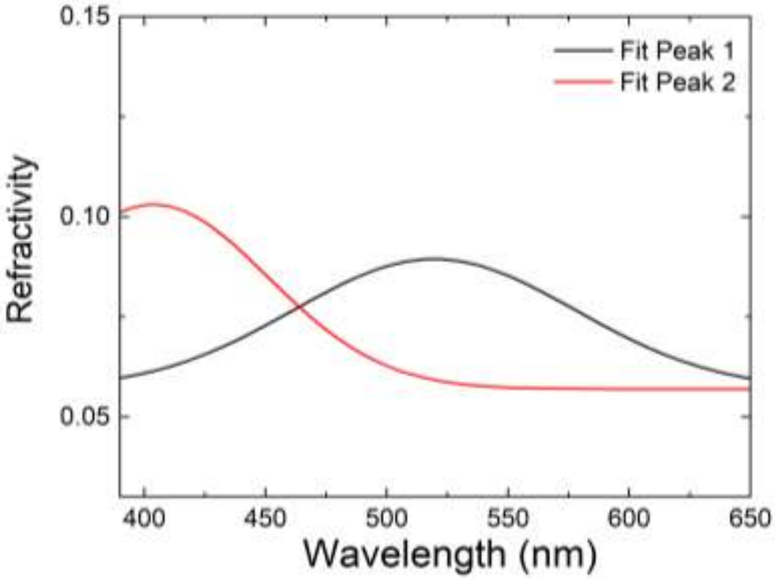

Figure 56. Deconvolution result of absorbance spectrum taken after anti-BSA functionalization.

In these analyses, the spectra for both anti-BSA and BSA interactions were carefully examined. Each spectrum was subjected to peak fitting procedures, where the overlapping peaks were deconvoluted to isolate individual components. This deconvolution process is crucial as it allows for the precise determination of peak positions, intensities, and widths, providing detailed information about the binding events and interactions at the nanoparticle surface. As seen in Figure 56, deconvolution analyses provided much clarity locating the absorbance peaks at both ~420 nm and ~530 nm, ensuring more sensitive and fine determination of wavelength shifts at both positions.

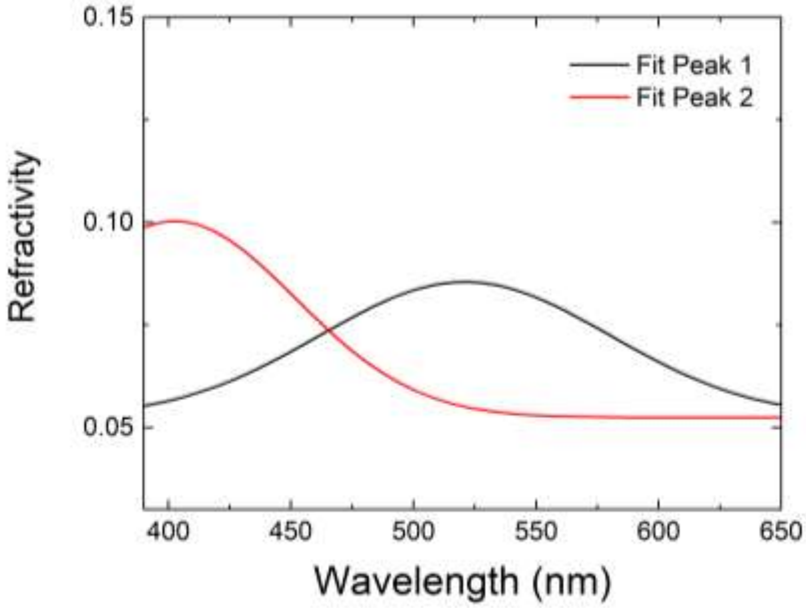

Figure 57. Deconvolution result of absorbance spectrum taken after anti-BSA and-BSA interaction.

After deconvolution, peaks were separated, and peak fitting were carried onto a separate figure. Figure 58 demonstrates peak shifts on both peaks after anti-BSA and-BSA interaction. These two peaks were acquired via regression and redrawing of deconvoluted peaks. As seen in the figure there was a significant wavelength shift and a refractivity increase after addition of BSA to the sensor platform. There was around 3 nm red shift on ~520 nm peak and around 2 nm red shift on ~400 nm peak after the interaction whereas no significant shift was ever observed with the rest of NPs that were modified or synthesized during this study. Deconvolution analyses that were added into the study at this step were also included in the future LSPR-based biosensor related analyses in the remainder of the study for better understanding the wavelength shifts caused by either protein or exosome interaction with the platform.

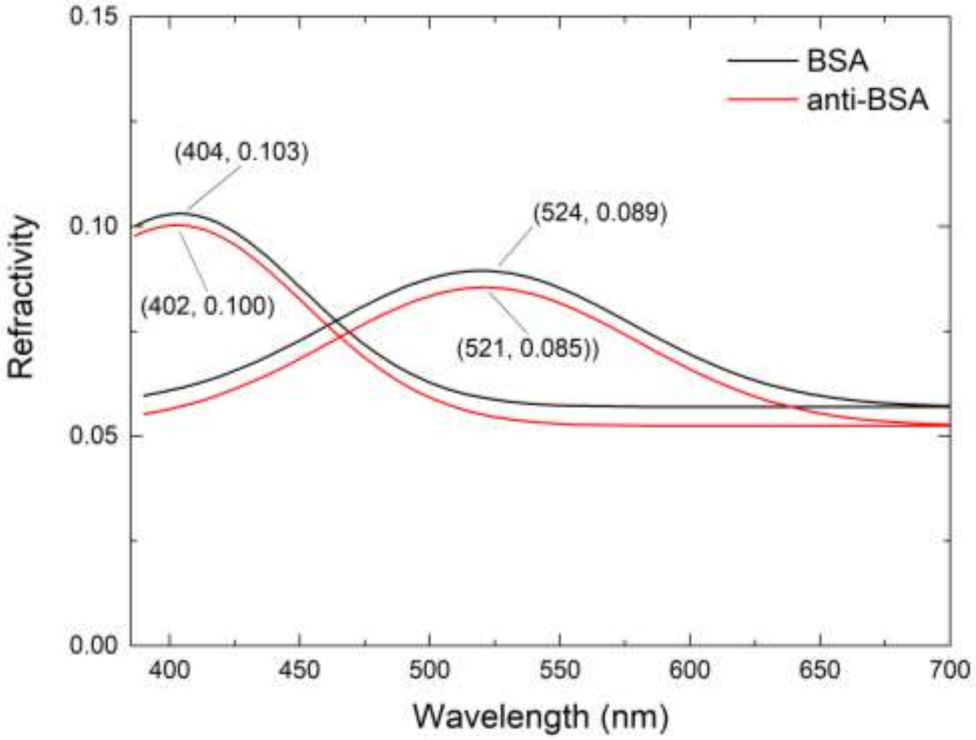

Figure 58. Deconvoluted peaks of Ab functionalization and BSA interaction signals.

Overall, deconvolution analyses provided much better visibility and hence promise better resolution. Figure 58 shows the wavelength shift of deconvoluted UV-Vis spectrum of 60:40 core-shell GNPs after addition of BSA protein. Henceforth all the analyses that include wavelength shift calculation of core-shell NPs were carried out after deconvolution of peaks were done. So far the optimization of the LSPR-based sensor platform was carried out in terms of nanoparticle synthesis and modification for enhanced plasmonic characteristics for biosensing applications and also optimization of utilized reagent such as MUA was concluded. In summary, the optimization of the LSPR-based sensor platform encompassed nanoparticle synthesis, surface modification with MUA, and rigorous protein detection studies with BSA. Each phase of the study contributed to refining the platform's capabilities and understanding its operational parameters. Moving forward, these advancements pave the way for deploying the LSPR biosensor platform in diverse research and practical settings, offering a robust tool for sensitive and selective biomolecular detection. The study followed up with model protein detection study with BSA to determine sensory characteristics further, for LPSR biosensor platform.

3.2.7 Model Protein Detection via Developed LSPR Sensor Platform

After the optimization of NPs was completed, characterization of the platform for biosensing applications were carried out in terms of detection limits, dynamic detection range, and resolution. For this purpose, BSA was used as a model protein initially, and the platform was tested within the protein concentration range of 30-1000 nM. Figure 59 shows both the shifts of six replications and prepared calibration curve.

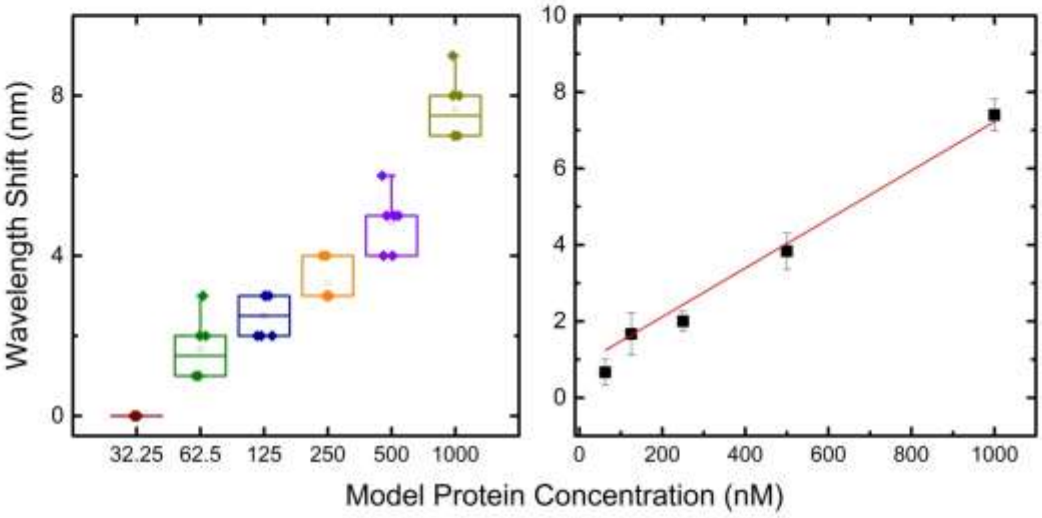

Figure 59.Wavelength shifts acquired during BSA detection and prepared calibration curve for BSA

As seen in the figure, signal acquired from the platform followed a linear trend in the studied concentration range. The lower detection limit (LoD) was calculated to be 0.26 nM and limit of quantification (LoQ) to be 0.78 nM for BSA. Which are highly comparable to one of the current gold standards ELISA that reported to have an LoD of 0.96 nM (Khamehchian et al. 2008).

3.2.8 Membrane protein detection with core-shell LSPR platform

The same procedure that was done for the model protein was followed and a study range of 6-200 nM for CD81 and 1-100 nM for CD151 was utilized. Figure 60 shows the wavelength shifts of six replications of both protein detection assays. A linear trend was observed in the whole studied range and a significant difference was seen throughout all samples. Following figure shows the wavelength shifts acquired during the study.

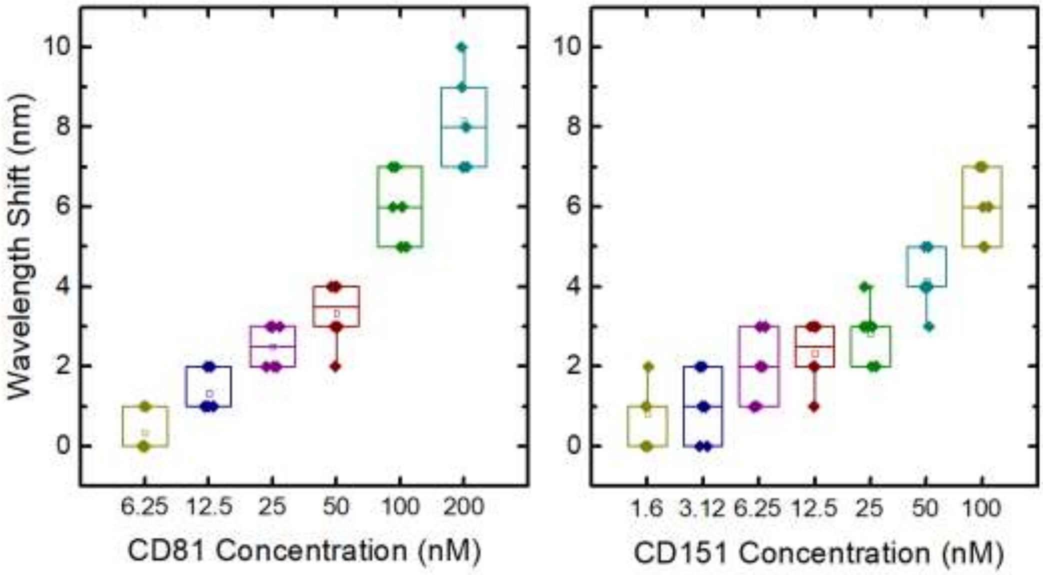

Figure 60. Wavelength shifts acquired during CD81 and CD151 detection.

Next, calibration curves were formed for further investigation of sensory characteristics of LSPR sensor platform. The prepared calibration curves can be seen in the Figure 61. The LoD was calculated to be 0.43 nM and LoQ to be 1.32 nM for CD81; and 0.31 and 0.93 nM for CD151. As CD81and CD151 have lower molecular weights compared to BSA, it was anticipated to have a relatively lower signal per concentration difference ratio. Overall, exosomal membrane protein detection studies were carried out successfully in the determined study range.

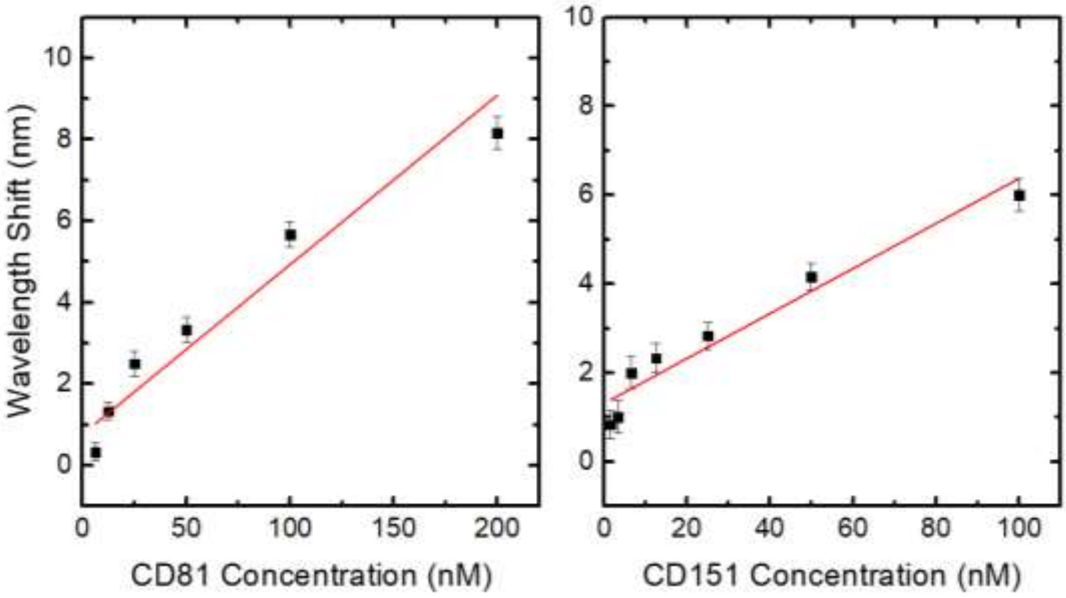

Figure 61. Calibration curves formed utilizing the data acquired via the detection study of CD81 and CD151 studies.

Overall, LSPR sensor development for exosome detection was completed. For this purpose, several NPs were synthesized or modified and used during the study. Then, these NPs were utilized in the developed LSPR biosensor platform for BSA detection as a model protein. Comparing the sensitivity and resolution enhancement effectivity of utilized methodologies it was evident that sore-shell NPs showed better sensitivity for both the model protein. Then further optimization of core-shell NP synthesis and functionalization was carried out and the sensor platform was made ready for further characterization of its sensory characteristics such as resolution, working range, and detection limits. These characterizations were carried out utilizing BSA as a model protein and then utilizing target ExoMPs.

3.3 MagLev Sensor Platform Fabrication and Optimization

3.3.1 MagLev Sensor Platform Working Principle

MagLev biosensor platforms provide density-based detection and quantification. In the magnetic levitation setup that has been utilized in this study, magnets are used in an orientation facing each other's same poles to overcome gravitational acceleration. Within this field a paramagnetic medium is filled, and it is used to levitate samples exploiting their diamagnetic features. This procures a method without complexity and with high sensitivity which is used to separate samples with minute differences in density (Chengqian Zhang et al. 2018; Katherine A Mirica et al. 2009). Figure 62 summarizes the detection principle of MagLev biosensor platform. As seen in the figure the density changes of Polystyrene Microspheres (PSMs) were utilized to verify Ab functionalization and determine their interaction with proteins or exosomes. Here, PSMs were functionalized with related Abs. Afterwards Ab functionalized PSMs were incubated in antigen solutions. The levitation height of PSMs, Ab functionalized PSMs, and antigen captured PSMs were then compared to procure the effect of antigen on the mean density of PSMs which was expected to increase accordingly with antigen concentration due to the density increase in PSM-antigen complex.

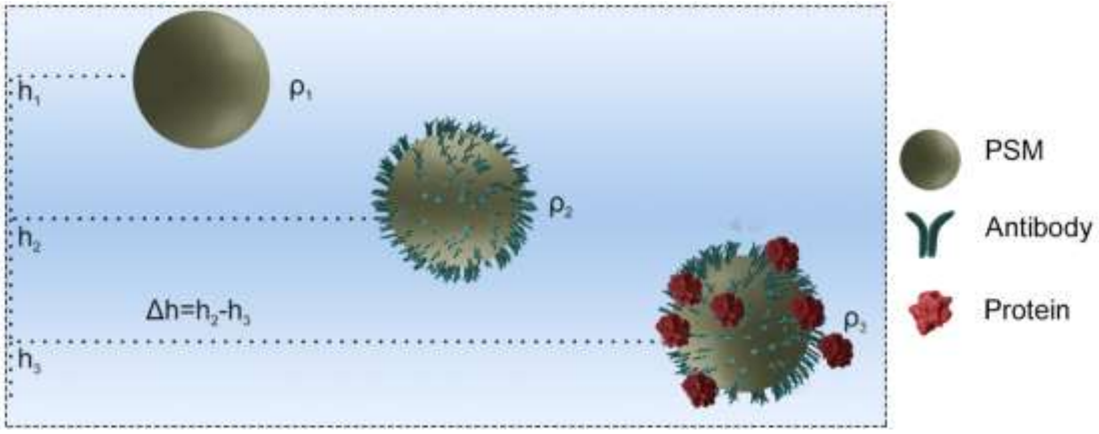

Figure 62. Working principle of MagLev biosensor platform

3.3.2 Optimization of the MagLev Biosensor Platform

Microsphere Size and Concentration Optimization

To obtain higher sensitivity and the best resolution, PSM size optimization for was carried out first. For this purpose, three sizes of microspheres (5, 20, and 200 µm diameter) were used and standard deviation of sample free PSMs (s_0), standard deviation corrected for LOD calculations (so’), calculated LOD, and p-value of normality test were estimated. Afterwards, dilution rates of microspheres were analyzed. Acquired microscopy images of said optimizations can be monitored in Figure 63. As seen in the figure no levitation greater than 600 µm was seen in any size of PSMs; hence it‘d theoretically be possible to enhance resolution of the platform with usage of higher concentration paramagnetic agent and fix a higher levitation height as reference.

Figure 63. Comparison of PSMs with different sizes; A) 200 µm, B) 20µm, and C) 5µm with 100x dilution ratio.

Levitation of all sizes of PSMs were carried out in 50mM Gx solution and succeeded. However, time period needed for levitation increase with decreasing PSM diameter where levitation of PSMs with 200 µm had taken about 3-5 minutes; PSMs with 5 µm needed more than 20 mins to stabilize at a certain levitation height. Also, aggregation was monitored in both 20 and 5 µm PSMs.

Table 5. Statistical analyses for possible sensory characteristics of PSMs with various diameters.

PSM size	**P-Value (Kolmogorov-Smirnov Correction)**	**Std. Deviation**	**S'$_0$**	**LOD (µm)**	**n**
5 µm (100x)	0.2253	94.312	17.823	53.467	28
20 µm	0.0528	41.978	7.798	23.393	28
200 µm	0.1349	71.514	13,515	40.455	28

Table 5 gives relevant statistical values of each PSM diameter. Because 200µm PSMs didn't provide a larger sample size (number of PSMs that were possible to visualize in a triplicate experiment due to the size of PSMs; n); all other samples were derived randomly from a larger pool, hence it'd be safer to compare 20 µm and 5 µm in a calculation with larger sample sizes, which is in Table 6. In the samples in table 6 nearly 10-fold greater samples sizes were utilized for statistical analyses to investigate standard deviation and levitation behavior in terms of normal distribution better.

Table 6. Statistical analyses for possible sensory characteristics of PSMs with 5 and 10 µm diameters.

PSM size	**P-Value (Kolmogorov-Smirnov Correction)**	**Std. Deviation**	**S'$_0$**	**LOD (µm)**	**n**
5 µm (100x)	0.2253	104.790	6.722	20.167	243
20 µm	0.0569	47.016	2.000	8.997	243

When larger sample sizes were taken into account LoD value of both PSM sizes decreased while they retain normality and a relatively close standard deviation. Comparison between varied dilutions (100x and 200x) of 5 µm microspheres was also carried out and images of both are presented in Figure 64. Both samples have shown levitation in about 20-30 minutes, and below is Table 7 that indicates related statistical analyses results.

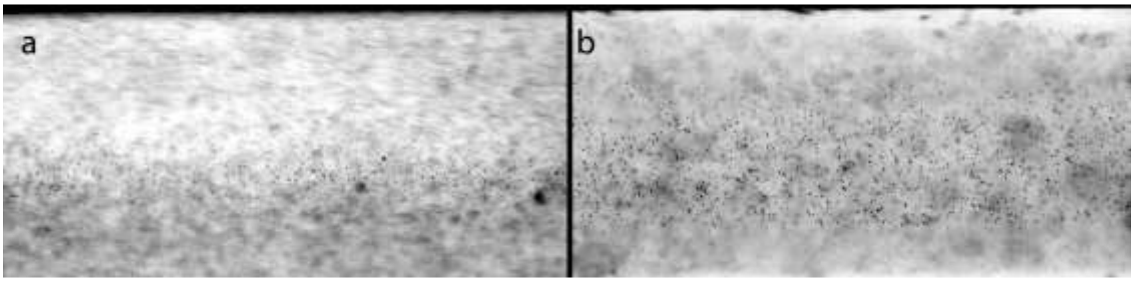

Figure 64. Images of microspheres with 5 µm diameter, with dilution factors of a) 100x dilution factor, b) 200x dilution factor.

As seen in Table 9, 200x dilution factor wasn’t normally distributed, in terms of LOD and standard deviation; dilution factor is not an effective factor Levitation was observed in each sample for approximately 20 minutes, but consistent levitation was not observed. Additionally, there was a continuous circular motion in the capillary, which impeded the clear imaging of the samples. These motions can be attributed to collisions between intra-particles and particles with the capillary wall. As explained by Tajfirooz et al. (2021), a reduction in particle size prolongs the time required for magnetic levitation to stabilize (Tajfirooz et al. 2021; Haq et al. 2023; Thompson 2000). Magnetic levitation is typically confined to the vertical axis; however, with a larger number of particles, the levitation region may shift. This off-axis levitation can induce rotation of the PSMs and result in unstable levitation due to constant motion, as discussed by Liang et al. (2021) and Zhang et al. (2020). Table 10 presents the statistical analysis results related to 5 µm PSMs (Liang et al. 2021; C Zhang et al. 2020).

Table 7. Statictical analyses resılts of microspheres with 5 µm diameter, with dilution factors of 100x 200x.

Dilution rate	**P-Value (Kolmogorov-Smirnov Correction)**	**Std. Deviation**	**S'_0**	**LOD (µm)**	**n**
100x	0.2253	104.790	6.722	20.167	243
200x	0.016	86.216	5.531	16.592	243

Henceforth, the rest of the experiments were carried out with 20 µm diameter microspheres both for sakes of lower LoD values and also for better resolution in microscopy images. Next step was to determine a dilution factor for microspheres since with its current dilution factor (25x) there were problems of aggregation and also the need of excess amount of Ab. The following Figure 65 consists of the images acquired by taking images of serially diluted 20 µm PSMs. 0.01% Tween 20 was added to each sample to prevent any possible aggregation and adhesion to capillary walls. The microscopy images of mentioned dilution rates can be observed in the following Figure 65. It is clear that, decreasing PSM concentration and the addition of detergent are effective strategies for preventing aggregation. The successful implementation of these strategies at 100x and 200x dilutions ensures that a sufficient number of well-dispersed PSMs are available for further statistical analyses, thereby enhancing the accuracy and reliability of the study. These findings are instrumental in guiding future experimental designs and optimizing the preparation of PSMs for various analytical applications.

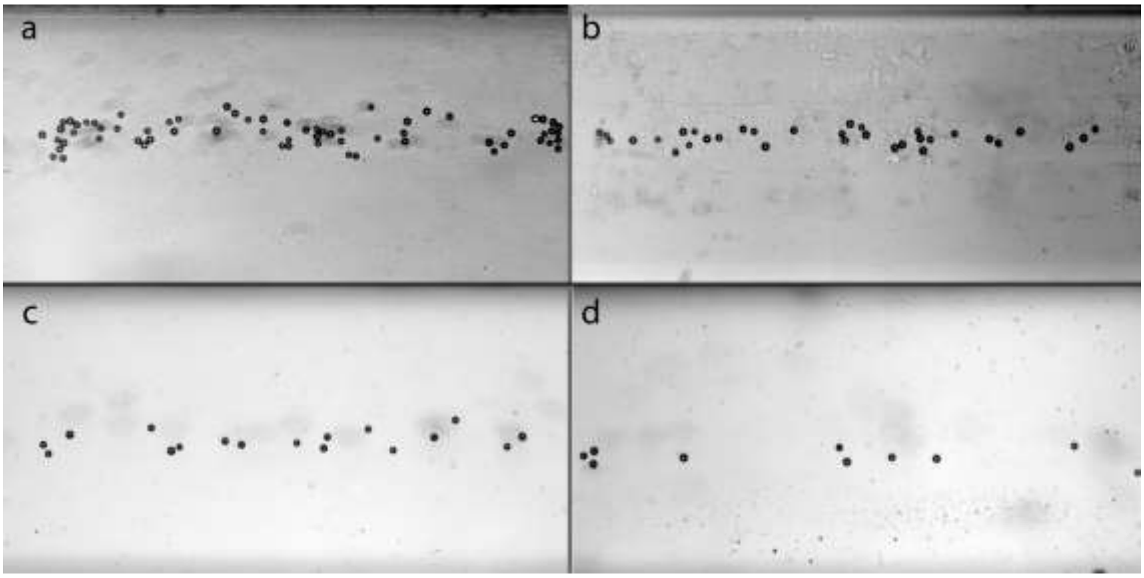

Figure 65. Images of PSMs with 20 µm diameter, with dilution factors a)50x, b)100x, c) 200x, and d) 400x.

Optimization of Antibody Functionalization

After optimization of PSM size and concentration optimization of Ab concentration was carried out and Ab concentration for surface saturation was determined; Figure 66 below summarizes the results.

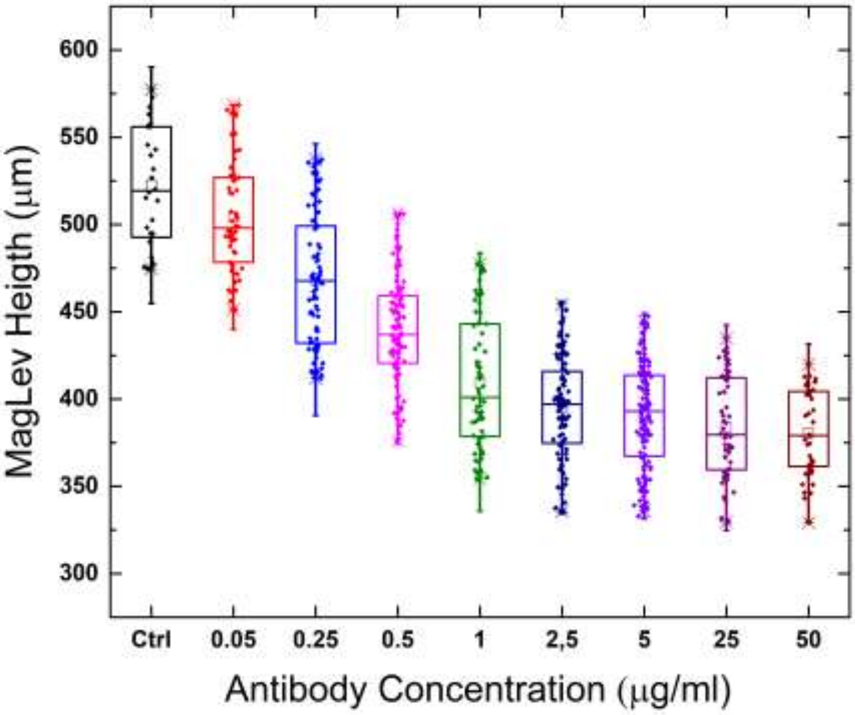

Figure 66. Distribution graphic of Ab functionalized microspheres with increasing Ab concentrations; regarding surface saturation study with various Ab concentrations.

One way ANOVA analysis was carried out and showed the model to be significant [F (6,311) = 28.932, p<.001], details can be seen in Table 10. Non-linear regression analyses were also carried out to support this claim and Figure 72 shows the regression plot and equation below gives the related mathematical model. It can be observed that concentrations greater than 5 µg/ml showed no significant magnetic levitation height difference, which point was accepted as the saturation concentration.

$$y = 577.841 + 58.929e^{-0.811X}$$

Mathematical model of the relation between Ab functionalized PSMs, Ab concentration on PSM surface and levitation height of PSMs; X representing Ab concentration and y representing mean magnetic levitation height of microspheres.

Table 8. Statistical analyses of Ab surface saturation study for PSMs utilizing anti-BSA Ab.

s	n	*Mean*	*Standard Deviation*	SE of Mean
0.125	57	*635.284*	*22.497*	2.980
0.25	52	*623.369*	*20.997*	2.912
0.5	38	*613.269*	*13.685*	2.220
1	44	*604.181*	*17.631*	2.658
2	46	*594.567*	*25.691*	3.788
4	41	*574.594*	*22.497*	3.514
5	40	*580.813*	*22.481*	3.554

**These values are given as contrast tests with sequent concentration i.e. 0.125% with 0.25%. or 0.25% with 0.5%.*

Regression analyses, as depicted in Figure 67, also revealed insightful trends regarding the mean levitation change of the PSMs in relation to varying Ab concentrations. The observed levitation changes can be attributed to the increasing density of Ab-PSM complex with increasing concentration of Abs. Given this data, it would be safe to assume that at a concentration of 25 µg/mL, the surface of the PSMs reaches a point of saturation with Abs. This assumption is supported by the relatively smaller incremental change in levitation height observed beyond the 25 µg/mL concentration. Essentially, once the PSM surface is saturated with Ab molecules, any further increase in Ab concentration results in minimal additional binding, thereby stabilizing the levitation height.

The saturation point at 25 µg/mL is a crucial finding, as it provides a benchmark for optimizing the concentration of antibodies in future experiments. Knowing this saturation point allows researchers to avoid using excessive Ab concentrations that do not significantly enhance the binding efficiency, thereby conserving valuable resources and reducing potential experimental costs. The regression analyses illustrated in Figure 67 highlight a critical threshold in Ab concentration, pinpointing 25 µg/mL as the saturation point for PSM surfaces.

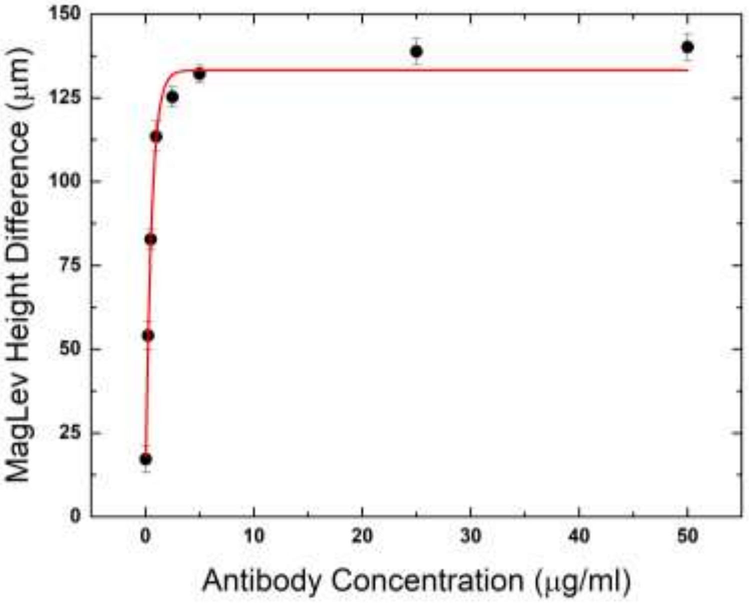

Figure 67. Nonlinear regression results of Ab saturation study, mean levitation heights of microspheres (R^2=0.97).

3.3.3 Model Protein Detection with MagLev Sensor Platform

The study was followed by a comparison of un-functionalized PSMs in paramagnetic solution, un-functionalized PSMs in BSA solution of 1 mM, Ab functionalized PSMs in paramagnetic solution, and Ab functionalized PSMs in 1mM BSA solution; results can be seen in the Figure 68. This comparison was carried out determine whether there are any interactions between PSMs without functionalization with BSA, measuring PSM levitation height and functionalized PSM levitation height to serve as control groups, and lastly determination of levitation height difference caused by protein PSM complex formation.

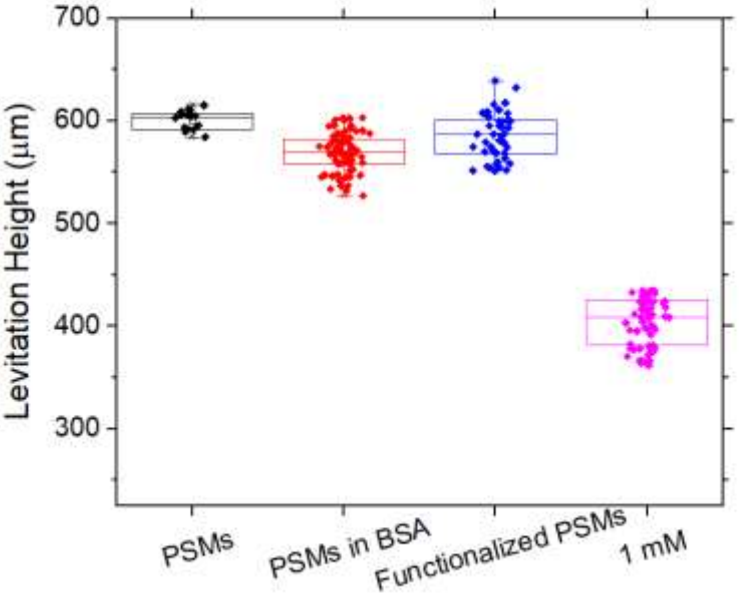

Figure 68. Comparison of Ab functionalized microspheres and non-functionalized microspheres against BSA solution. Left to right: 1st microspheres with no functionalization, 2nd microspheres with no functionalization in 1mM BSA solution (Control), 3rd functionalized microspheres (Blind), and 4th functionalized microspheres after interaction with protein solution.

Figure 68 illustrates the interaction between the carboxyl groups of the microspheres and the BSA protein. This interaction was observed to be relatively insignificant when compared to the interaction between Ab-functionalized microspheres and BSA. The functionalization of the microspheres with antibodies significantly enhances the binding affinity towards BSA, demonstrating the critical role of specific antibody conjugation in improving the sensitivity and specificity of the sensor platform.

To further evaluate the performance of the magnetic levitation sensor platform, various concentrations of BSA solutions were prepared and tested. These tests were designed to rigorously assess the sensor’s capability in detecting and quantifying BSA at different concentration levels. The goal was to determine the sensor's sensitivity range and its potential for practical applications in detecting target proteins in biological samples. The microscopy images obtained during these tests, presented in Figure 69.

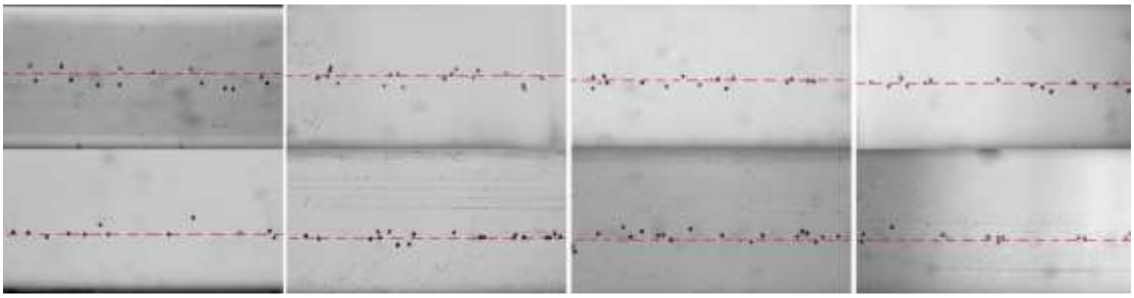

Figure 69. Top row from left to right: PSMs, functionalized PSMs, 10 nM, 10^2nM; bottom row from left to right: 10^3 nM, 10^4 nM, 10^5 nM, 10^6 nM. Red line indicates the mean value of each sample.

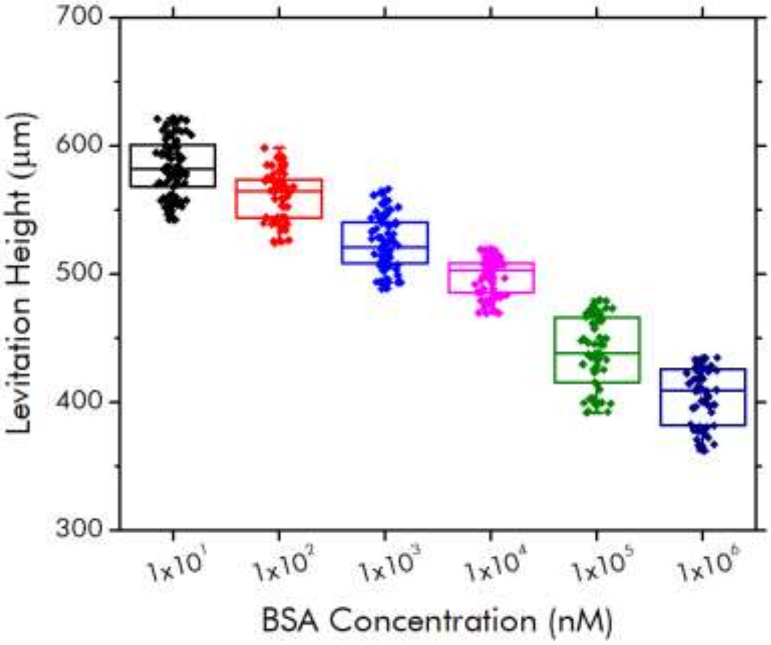

Figure 70. Interaction between suspensions of Ab functionalized microspheres of 20 µm diameter and BSA protein solutions of various concentrations.

It is evident that developed magnetic levitation sensor platform was able to successfully determine BSA protein down to 10 nM concentration. The results of the sample with lowest BSA concentration and Ab functionalized microspheres showed that the difference between their mean levitation heights is statistically significant ($p<.05$). An LoD value of 62.04 nM was calculatedThis calculated LoD is highly comparable to the current gold standard for BSA detection, ELISA. Literature reports LoD values of 64 ng/ml for ELISA, 157 ng/ml for the BCA assay, and 138 ng/ml for the Bradford assay (Khamehchian et al. 2008; BioTek Instruments 2021; Sudjarwo, Dobler, and Lieberzeit 2021). Table 9 summarizes the levitation heights and descriptive statistics of each sample, also normativity test results.

Table 9. Descriptive statistics and Kolmogorov-Smirnov normality test results of BSA detection via MagLev sensor platform.

Concentration (nM)	Mean	Standard Deviation	Median	Variance	p-Value
Control	585.097	23.005	586.960	529.250	0.109
10	586.55	19.651	584.074	386.160	0.348
10^2	563.740	17.734	564.844	314.488	0.102
10^3	526.637	21.840	524.156	476.964	0.034
10^4	499.860	13.094	502.614	171.453	0.020
10^5	442.949	25.685	445.064	659.740	0.023
10^6	409.869	20.485	414.327	419.627	0.001

PSM levitation height showed normal distribution for all studied protein concentrations, then one-way ANOVA was applied for further analyses and comparison. One way ANOVA results showed that the population means are significantly different at the 0.05 level. Also, Tukey post-hoc tests were run, and Tukey’s Honest Significant Difference (HSD) showed that there is a significant difference of means between all pairwise comparisons at the 0.05 level. These findings suggest that there are indeed significant differences in means among the samples with various concentrations, and the Tukey’s HSD post hoc analysis has helped identify all samples’ means differ from each other.

3.3.4 Exosomal Membrane Protein Detection via MagLev Sensor Platform

Next, in order to investigate the capability of the MagLev sensor platform to detect membrane proteins, previous study on BSA detection with MagLev platform was reenacted for EpCAM ExoMP. Resultant microscopy images can be seen in the Figure 71.

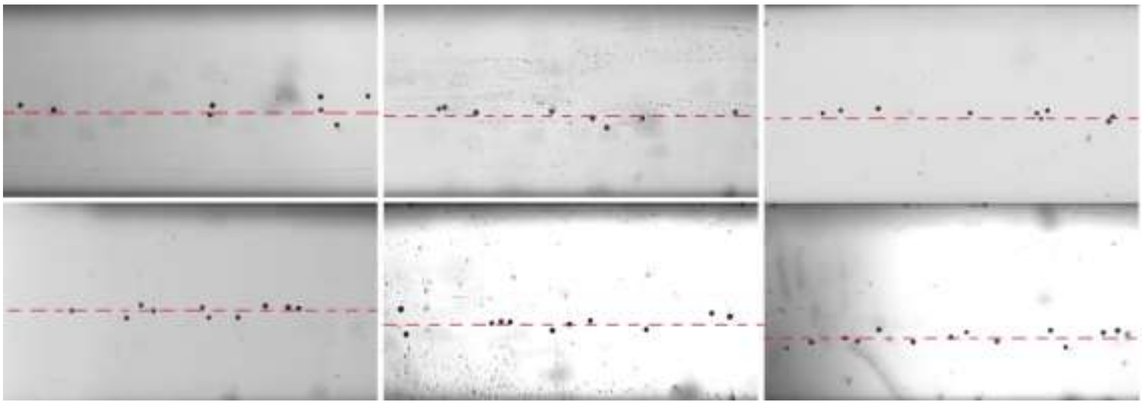

Figure 71. Studied sample concentrations of EpCAM protein were as follows; Top row from left to right: Control, 1 nM, 5 nM; bottom row from left to right: 10 nM, 50 nM, 100 nM. Red line indicates the mean value of PSMs.

The details of levitation height differences and distribution is demonstrated in Figure 72. These images provide a detailed visual representation of the microspheres and their interaction with EpCAM at different concentrations. At first glance results indicate that prepared PSMs were able to detect EpCAM protein with a concentration as low as 5nM. In conjunction with the microscopy images, the measured levitation heights, as shown in Figure 72, quantitatively depict the sensor’s response to the different EpCAM concentrations.

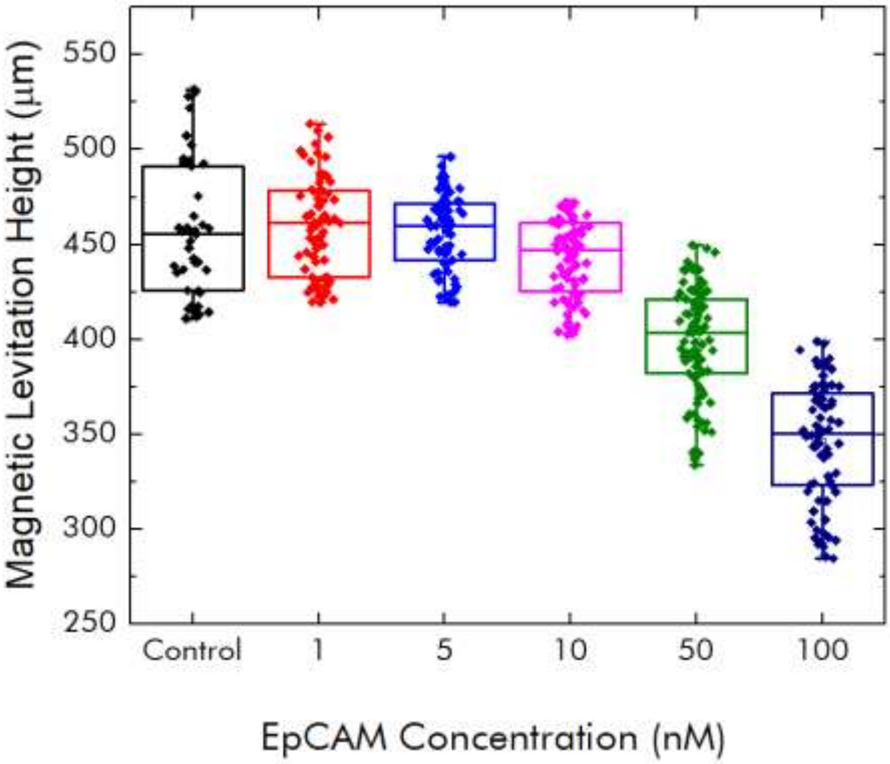

Figure 72. Magnetic levitation heights of PSMs in EpCAM protein samples, mean values, standard deviations, and medians.

Next, linear fitting was applied between results of samples with concentrations of 5, 10, 50, and 100 nM below the results can be seen in Figure 73. It is evident that a linear dynamic range between 5-100 nM was reached with possibility of further improvement for higher protein concentrations.

As Figure 73 suggests, there is a linear relation between magnetic levitation height difference and target protein concentration. The increase in protein concentration in the samples directly affected the levitation height difference between Ab functionalized PSMs and PSMs that formed a complex with ExoMPs in this study. The LoD value of the sensor platform was calculated to be 5.47 nM, and the LoQ to be 16.42 nM. For further investigation statistical analyses were carried out.

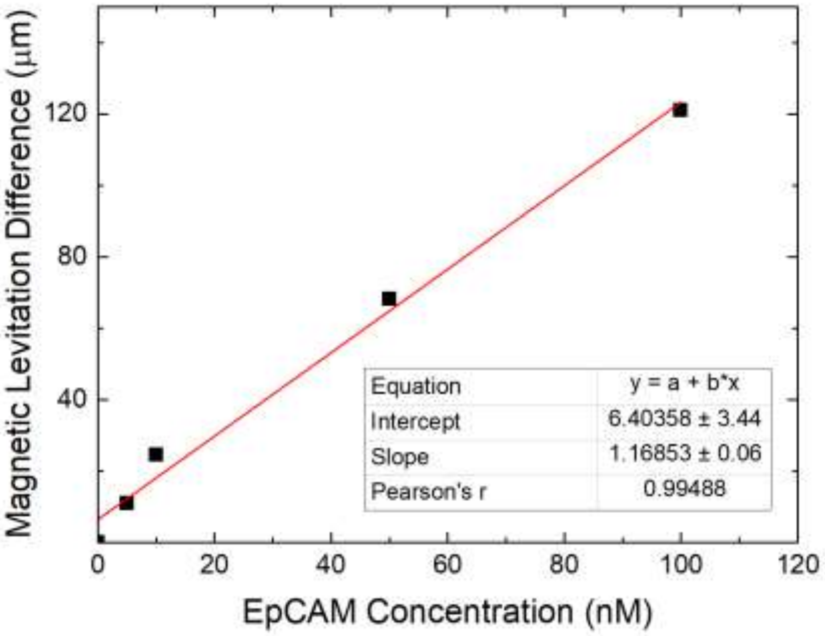

Figure 73. Calibration curve prepared by the linear fitting of EpCAM detection MagLev results.

Table 10 below shows the results descriptive statistical analyses of these results. In the table, Kolmogorov-Smirnov normality test results can be seen where each sample showed a normal distribution.

Table 10. Descriptive statistics and Kolmogorov-Smirnov normality test results of EpCAM detection study via MagLev sensor platform.

Concentration (nM)	Mean	Standard Deviation	Median	Variance	p-Value
Control	467.056	32.43	463.081	1051.841	0.588
1	459.715	25.78	461.413	664.762	0.307
5	456.000	19.98	459.590	399.539	0.458
10	442.478	20.98	446.929	439.989	0.260
50	398.836	28.93	403.701	837.027	0.567
100	346.084	31.42	350.394	987.277	0.630

One way ANOVA results showed that the population means are significantly different [F (6, 469) = 183.4] at the 0.05 level. Also, Tukey post-hoc tests were run and Tukey’s Honest Significant Difference (HSD) showed that there is a significant difference of means between all consecutive pairwise comparisons at the 0.05 level, except for 1 and 5 nM. These findings suggest that there are indeed significant differences in means among the samples with concentrations greater than 5nM.

The same procedure then was applied with CD151 protein and due to better sensitivity of the MagLev platform for CD151 protein lower protein concentrations were also added to experimentation plan. The same detection methodology was followed, except instead of anti-EpCAM Ab PSMs were functionalized with anti-CD151 Ab with the same concentration. Then the procedure was followed as described before. The levitation heights of the samples visualized by light microscopy can be seen in Figure 74.

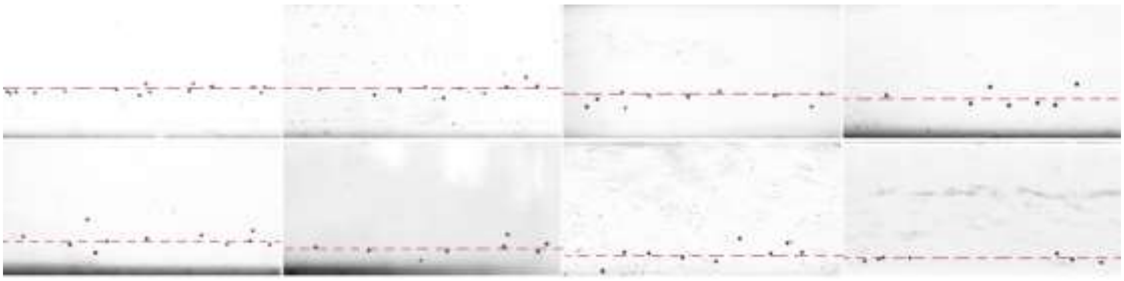

Figure 74. Studied sample concentrations of CD151 protein was as follows; Top row from left to right: Control, 0.1 nM, 0.5 nM, 1nM; bottom row from left to right: 2.5 nM, 5 nM, 10 nM, and 50 nM. Red line indicates the mean value of PSMs.

Results indicate that prepared PSMs were able to detect CD151 protein with a concentration as low as 0.5 nM. Figure 75 exhibits all the experimental results graphically which also summarizes the results of CD151 detection study for MagLev sensor platform. Next, linear fitting was applied between results of samples with concentrations of 1, 2.5, 5, and 10 nM below the results can be seen. It is evident that a linear dynamic range between 0.5-10 nM was reached with possibility of further improvement for higher protein concentrations.

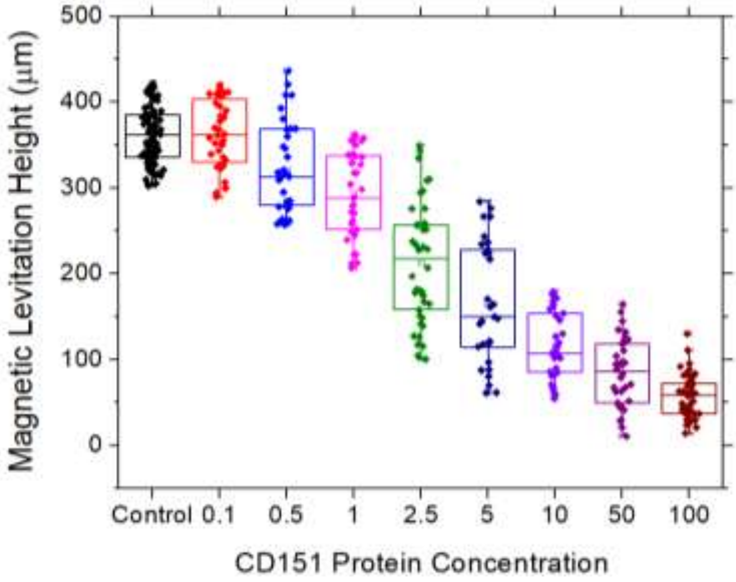

Figure 75. Magnetic levitation heights of PSMs in CD151 protein samples, mean values, standard deviations, and medians.

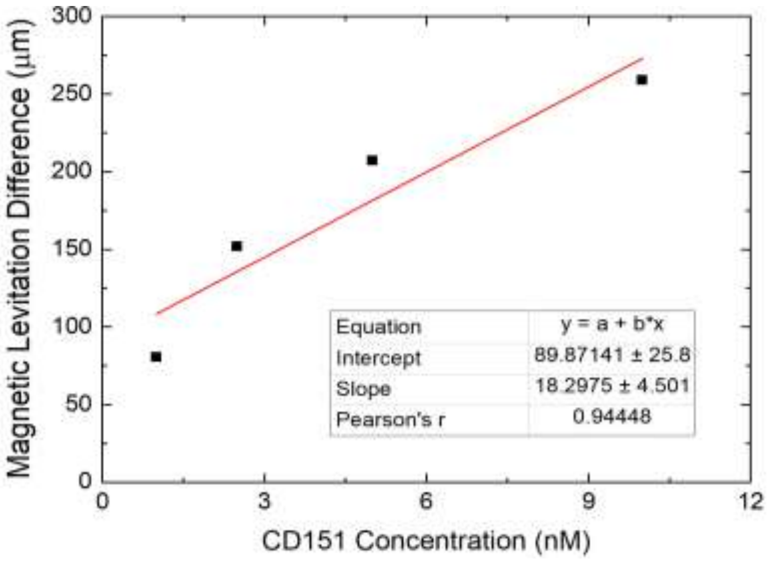

Figure 76. Calibration curve prepared by the linear fitting of CD151 detection MagLev results.

Figure 76 suggests, there is a linear relation between magnetic levitation height difference and target protein concentration in the range between 0.5-10 nM CD151 concentrations. The LoD value of the sensor platform was calculated to be 0.81 nM, and the LoQ to be 2.43 nM. There was a definitive sensitivity variation between the proteins that were used in the detection studies so far. This sensitivity difference against BSA, EpCAM, and CD151 can be explained by density differences between proteins. As explained by Fischer et al., average protein density is a molecular weight-based property especially for proteins with a molecular weight lower than ~40kDA (Fischer, Polikarpov, and Craievich 2004). The density slowly increases after the mentioned limit, and it shifts from 1.35g/ml to 1.42g/ml at 20kDA; where EpCAM and CD151 proteins reside in between, hence it can be said that there is an increase in density as the experiments advanced from BSA to EpCAM and to CD151 which explains the increase in MagLev platform sensitivity. Overall Ab -antigen interactions were successfully visualized with an increased sensitivity and lower detection limit in case of molecules with smaller molecular masses (<40kDa).

For further investigation statistical analyses were carried out. Table 11 shows the results descriptive statistical analyses. These findings suggest that there are indeed significant differences in means among the samples with concentrations greater than 0.5 nM.

Table 11. Descriptive statistics and Kolmogorov-Smirnov normality test results of CD151 determination study via MagLev sensor platform.

Concentration (*nM)*	Mean levitation height	*Standard Deviation*	*Median*	Variance	p-Value
Control	361.081	32.04	421.601	1026.531	0.602
0.1	360.186	42.17	416.548	1532.260	0.612

0.5	320.300	52.76	436.146	2783.427	0.191
1	280.635	64.49	362.053	2389.860	0.747
2.5	209.385	72.06	349.002	4737.551	0.593
5	153.940	76.81	284.076	5050.910	0.537
10	102.373	49.32	179.108	1541.44	0.881
50	84.215	40.13	164.234	1610.658	1
100	56.768	24.90	130.270	620.060	0.633

Each sample showed a normal distribution as demonstrated in Table 13. One way ANOVA results showed that the population means are significantly different [F (8, 371) = 310.4] at the 0.05 level. Also, Tukey post-hoc tests were run and Tukey's Honest Significant Difference (HSD) showed that there is a significant difference of means between all consecutive pairwise comparisons at the 0.05 level, except for 0.1 and 0.5 nM.

CD81 protein detection was carried out next, as an exosome marker for this purpose PSMs were functionalized with CD81 Ab and CD81 protein solutions with concentrations between the ranges of 1-100nM were used. Figure 77 comprises the microscopy images and it shows that there was a visible decrease in PSM magnetic levitation height with increasing protein concentration in samples.

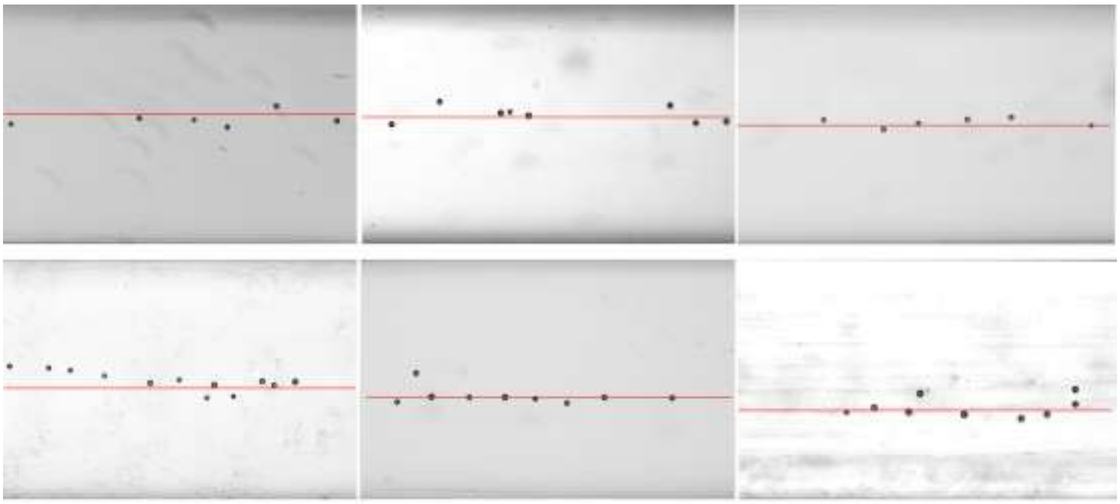

Figure 77. Studied sample concentrations of CD81 protein was as follows; Top row from left to right: Control, 1 nM, 5 nM; bottom row from left to right: 10 nM, 50 nM, and 100 nM. Red line indicates the mean value of PSMs.

In Figure 78 are the related distribution trends for CD81 sample results via MagLev sensor platform. The figure suggests that after 10 nM CD81 concentration there is a significant difference in magnetic levitation height when compared to functionalized PSMs. This significant decrease carries on up to the greatest studied concentration, which is 100nM. It is evident that the sensor platform was able to detect CD81 protein down to 10 nM concentration and quantification was possible up to 100 nM which gave a linear working range between 5 nM-100 nM.

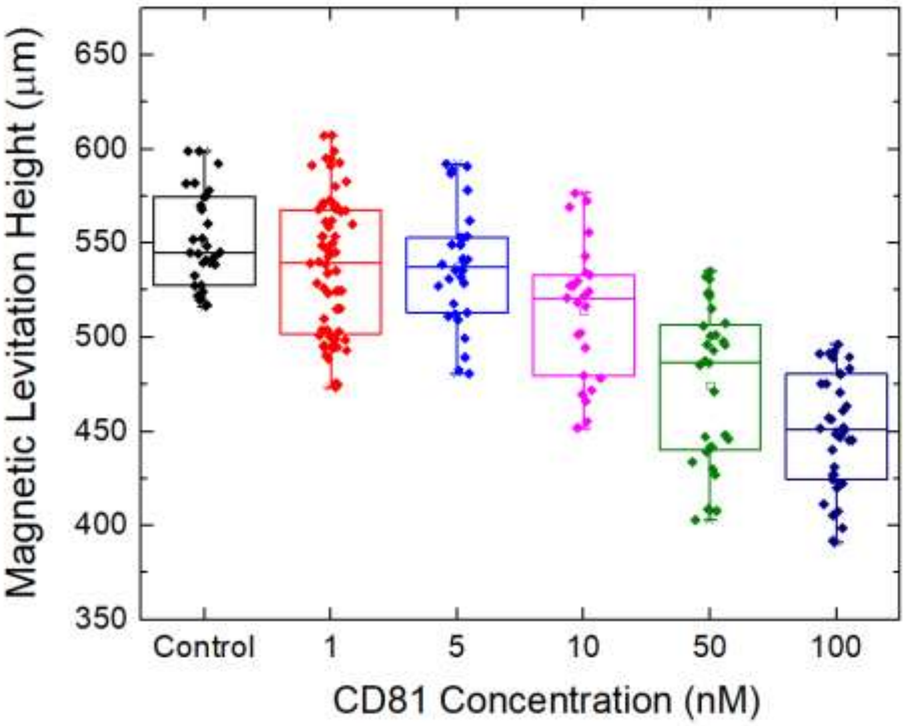

Figure 78. Magnetic levitation heights of PSMs in CD81 protein samples, mean values, standard deviations, and medians.

The related calibration curve, which was prepared utilizing the data in Figure 78 can be seen in Figure 79. As Figure 79 suggests, there is a linear relation between magnetic levitation height difference and target protein concentration in the range between 10-100 nM CD81 concentrations. The LoD value of the sensor platform was calculated to be 3.99 nM, and the LoQ to be 11.98 nM. Statistical analyses were carried out for further investigation of the developed MagLev sensor platform, in context of detecting CD81 exosomal marker protein.

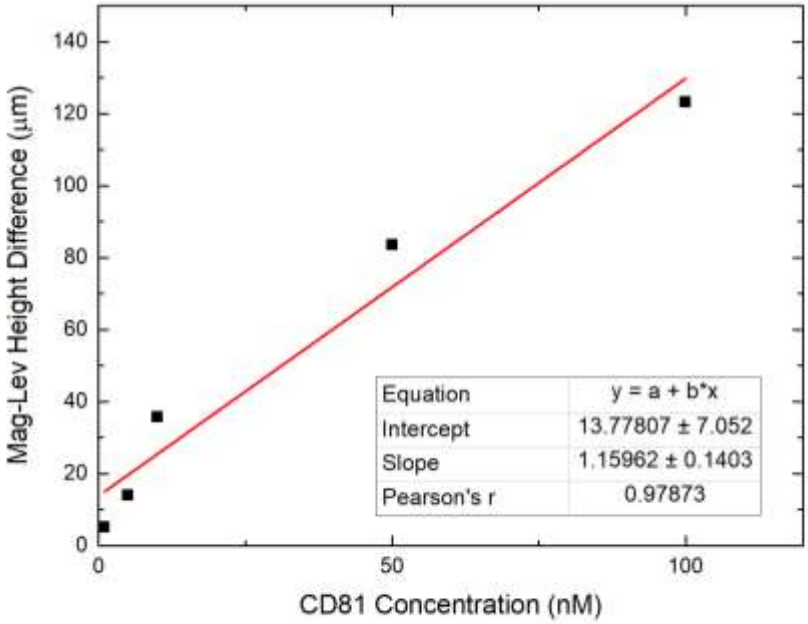

Figure 79. Calibration curve prepared by the linear fitting of CD81 detection MagLev results.

Following statistical results were acquired by processing the data that were drawn from the images. All samples showed normal distribution and ANOVA results showed that means of populations are significantly different. As normal distribution was achieved descriptive statistics were carried out and Table 12 summarizes the descriptive statistical analyses and normality test results.

Table 12. Descriptive statistics and Kolmogorov-Smirnov normality test results of CD81 determination study via MagLev sensor platform.

Concentration (nM)	Mean	Standard Deviation	Median	Variance	p-value
Control	551.783	27.391	544.870	625.401	0.514
1	547.372	53.927	549.750	1324.138	0.924
5	542.042	57.880	550.55922	950.414	0.310
10	538.826	50.113	541.289	1295.500	0.734
50	499.986	57.690	511.210	1750.685	0.237
100	497.241	46.216	500.851	992.020	0.820

In the experiment mean and median values of magnetic levitation heights decreased with increasing protein concentration. One way ANOVA results showed that the population means are significantly different [F (5, 258) = 10.07] at the 0.05 level. Also, Tukey post-hoc tests were run and Tukey's Honest Significant Difference (HSD) showed that there is a significant difference of means between all consecutive pairwise comparisons at the 0.05 level, except for 1 and 5 nM. These findings suggest that there are indeed significant differences in means among the samples with concentrations greater than 5 nM.

Overall, MagLev sensor platform development was completed through optimization of PSM size and concentration optimization, followed by Ab functionalization optimization. Ab concentration was determined by determining the required Ab to saturate PSM surface. Then, optimized sensor platform was verified by utilizing it to detect a model protein, BSA. Also this model protein study was used to incestigate the sensory characteristics of MagLev sensor platform for soluble proteins. Lastly, the MagLev sensor platform was used for detection of exosomal membrane proteins EpCAM, CD151, and CD81. Results were promising and satisfactory for each of the studied exosomal membrane proteins; in terms of sensory characteristics such as detection limit, sensitivity, and resolution for. Next, the developed sensor platform was utilized for isolated exosome detection, and the ability of distinguishing cancerous and healthy exosomes were tested.

3.4 Utilization of Developed Biosensor Platforms for *in-vitro* Exosome Detection

Detection of exosomes that were isolated from cell culture supernatants was carried out next. For this purpose, developed LSPR and MagLev platforms were utilized in optimized sensing conditions. The isolated exosome samples were diluted to investigate correlation of the signals with exosome concentration in samples. Exosome detection was performed using both sensor platforms, utilizing isolates obtained from the A549 (non-small cell lung cancer) and MRC5 (healthy lung fibroblast) cell lines. Each experimental set was conducted in triplicates.

3.4.1 Exosome Detection via Developed LSPR Biosensor Platform

Herein, the optimized core-shell NPs were used for detection of ExoMPs and ExoMP containing exosome detection was to detect exosomes; and 1:2, 1:4, and 1:8 dilution rates (0.5, 0.25, and 0.125 dilution factors) were used for *in-vitro* exosomes. First, anti-EpCAM Ab functionalized NPs were utilized for both A549 (cancerous) and MRC5 (healthy) cell line derived exosome detection. The procedures that were used for ExoMP detection was repeated for exosome samples. Figure 80 is composed of single detection results that demonstrate the average shift of triplicate experiments for EpCAM where core-shell NPs were used as an experimental platform.

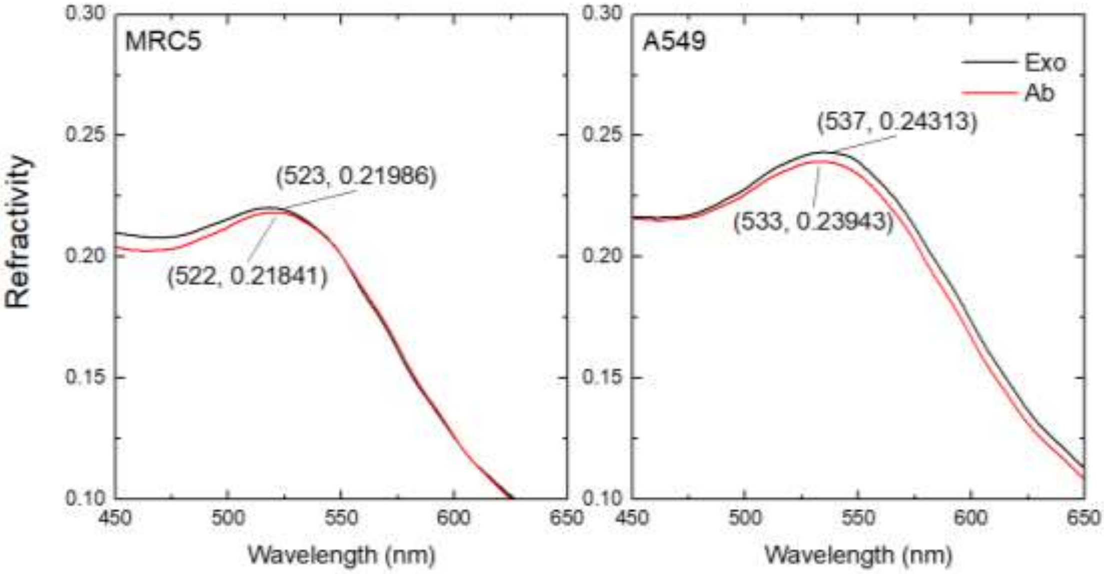

Figure 80. Exosome detection via anti-EpCAM Ab functionalized core-shell NPs with through LSPR sensor platform, for 0.5 dilution factor.

As seen in the figure, a three-fold greater wavelength shift was observed for A549 cell derived exosomes. Since A549 is a cancerous cell line, samples from A549 CCS were expected to contain a higher concentration of EpCAM and EpCAM containing exosomes. Figure 81 shows the comparison of two cell lines with various dilution factors.

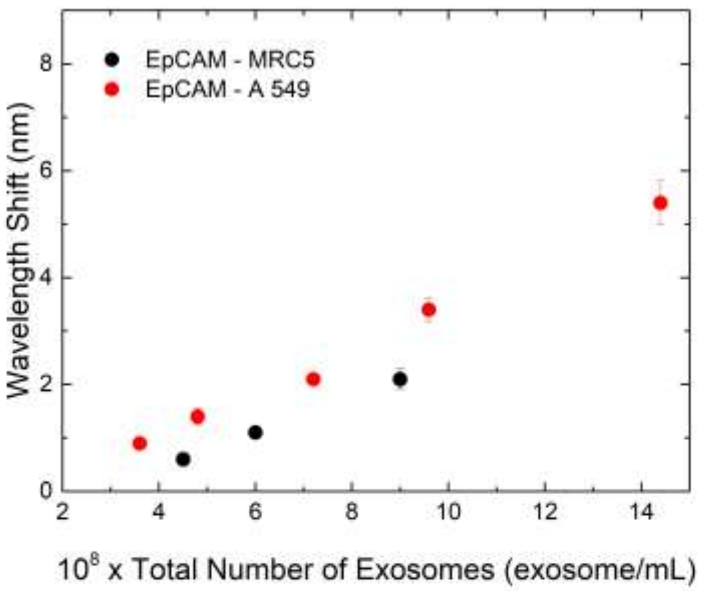

Figure 81. Comparison of A549 derived *in-vitro* exosomes with MRC5 derived *in-vitro* exosomes in terms of wavelength shift signal acquired via anti-EpCAM functionalized LSPR sensor platform (n=3).

Samples from both cell lines exhibited a clear and consistent decreasing trend in signal intensity with decreasing dilution factors. This observation strongly indicates a linear relationship between exosome concentration and the acquired signals. This finding aligns well with previous studies conducted on exosomal membrane proteins, reinforcing the robustness of the detection method employed in this research. The linear relationship not only corroborates earlier findings but also underscores the potential of this approach for precise quantification of exosomes in various samples. Further investigations were carried out utilizing NPs that are functionalized with anti-CD81 Figure 81 provides a detailed depiction of the wavelength shifts induced by the interaction between exosomes and the anti-CD81 Ab-functionalized NPs. The samples tested had a 0.5 dilution factor, which was chosen to represent a moderate concentration of exosomes.

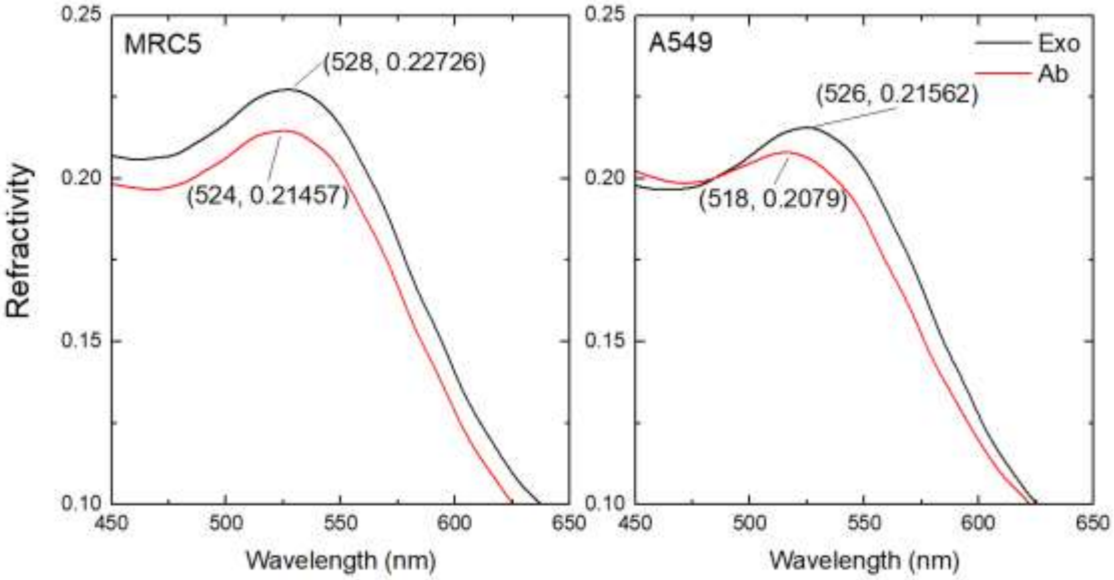

Figure 82. Exosome detection via anti-CD81 Ab functionalized core-shell NPs with through LSPR sensor platform, for 0.5 dilution factor.

As shown in Figure 82 there is a three-fold increase in wavelength shift when cancerous cell line derived exosomes are introduced into the sensor platform. As described in the literature cancer cells tend to generate more exosomes compared to healthy cell lines, which supports the results acquired here (Whiteside 2016). Figure 88 demonstrates the results with various dilution rates from both healthy and cancerous cell lines.

Figure 83 shows a linear relation between A549 derived exosome concentration and wavelength shifts. The same was not true for MRC5 derived exosomes, as in the previous graph healthy cell line derived exosomes caused a much lower wavelength shift. Though a semi-linear relation might be funded between healthy cell line derived exosomes it would have a much lower slope compared to cancerous cell line derived exosomes.

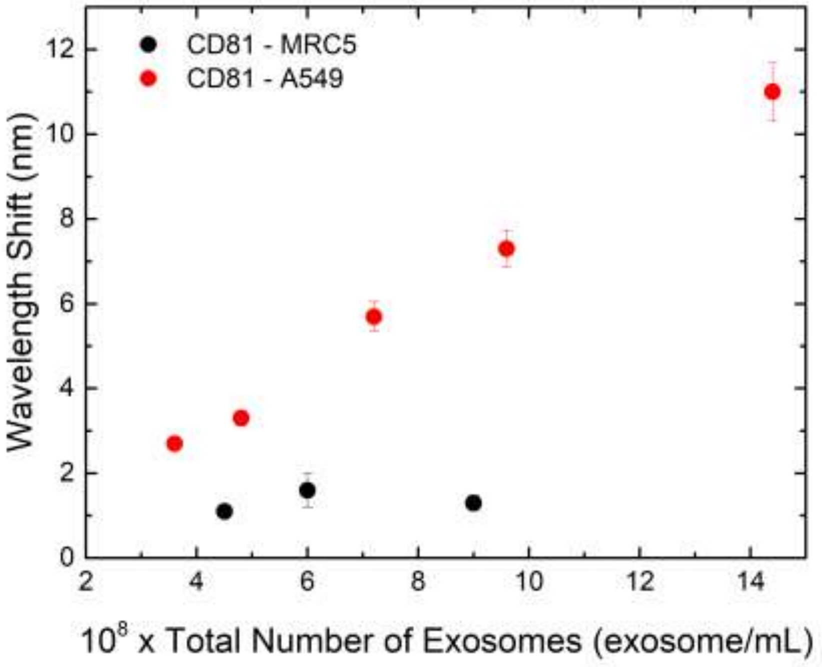

Figure 83. Comparison of A549 derived *in-vitro* exosomes with MRC5 derived *in-vitro* exosomes in terms of wavelength shift signal acquired via anti-CD81 functionalized LSPR sensor platform (n=3).

Lastly, anti-CD151 functionalized NPs were used for cell derived exosome detection. Figure 84 contains the data acquired by 0.5 dilution rate. As with the previous exosome detection studies here, A549 derived samples showed a five-fold greater wavelength shift compared to MRC5 derived ones. These wavelength shifts are critical indicators of the sensor's performance. A clear and distinct shift signifies a strong and specific interaction between the exosomes and the anti-CD151 Ab-functionalized NPs, highlighting the sensor's capability to accurately detect and quantify exosomes even at relatively low concentrations. As CD151 is considered to be a exosomal cancer biomarker for NSCLC and A549 is a NSCLC fibroblast cell line this results were most expected and welcomed.

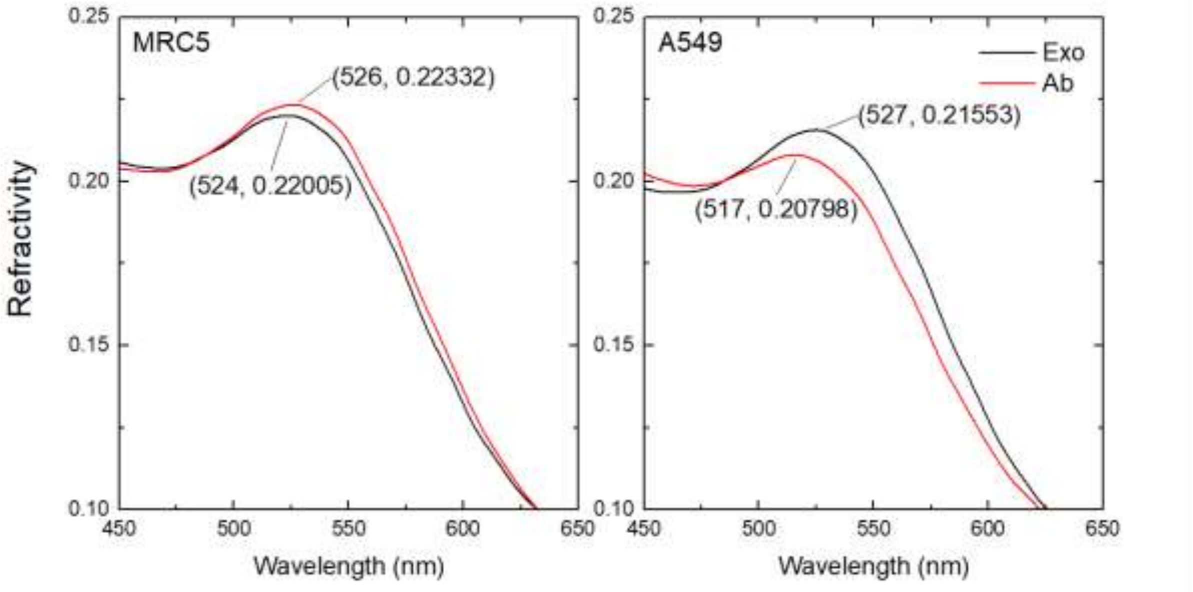

Figure 84. Exosome detection via anti-CD151 Ab functionalized core-shell NPs with through LSPR sensor platform, for 0.5 dilution factor.

In literature, it was previously shown that A549 cell line synthesizes exosomes that contain CD151 protein (J. Zhu et al. 2021), hence the initial expectation here was met; results indicated that both healthy and cancerous cell line derived isolates contained exosomes and NSCLC derived exosomes contained greater concentration of CD151 protein. The sensor platform, prepared utilizing developed sensitivity enhancement methodology, was able to distinguish CD151 containing exosomes and provide statistically significant signals (.05>p) compared to healthy cell line derived exosomes. Moreover, NSCLC marker CD151 showed a significant shift only for A549 derived exosomes, where MRC5 derived exosomes showed no significant shift. On the other hand, cancer cell line derived isolates contain much greater concentration of CD151 NSCLC marker comprised exosomes. In conclusion, the data from both cell line samples and the anti-CD151 Ab-functionalized NP experiments collectively demonstrate the efficacy and precision of the sensor platform.

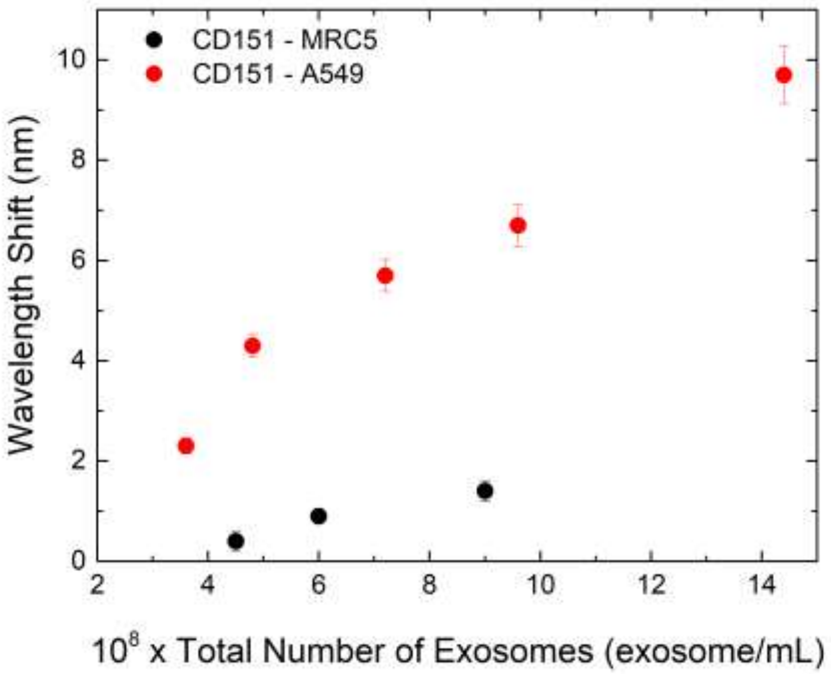

Figure 85. Comparison of A549 derived *in-vitro* exosomes with MRC5 derived *in-vitro* exosomes in terms of wavelength shift signal acquired via anti-CD151 functionalized LSPR sensor platform (n=3).

Figure 85 illustrates the increase in wavelength shifts with increasing dilution factors, providing a clear visual representation of the sensor's response to varying concentrations of exosomes. As seen in the figure slope of A549 results show a decrease around a dilution factor of 0.33 which indicates the saturation of LSPR sensor platform surface with exosomes, indicating a much higher number of exosomes compared to healthy cell line derived samples. This phenomenon is critical as it highlights the sensor's binding capacity and the point at which additional exosomes no longer contribute to an increased signal. The observed saturation at a dilution factor of 0.33 specifically for the A549 cell line indicates that these cancer-derived samples contain a significantly higher number of exosomes that contain CD151compared to those derived from healthy cell line.

3.4.2 Exosome Detection via Developed MagLev Biosensor Platform

Detection via MagLev sensor platform of exosomes that were isolated from cell culture supernatants were carried out next. For this purpose PSMs were functionalized with anti-EpCAM Ab first and 1:2, 1:4, and 1:8 dilution rates (0.5, 0.25, and 0.125 dilution factors) were used for *in-vitro* exosomes. Following results were acquired for EpCAM containing exosomes. Figure 86 shows the results of detection for A549 NSCLC cell line derived exosomes in comparison to MRC5 as a healthy control.

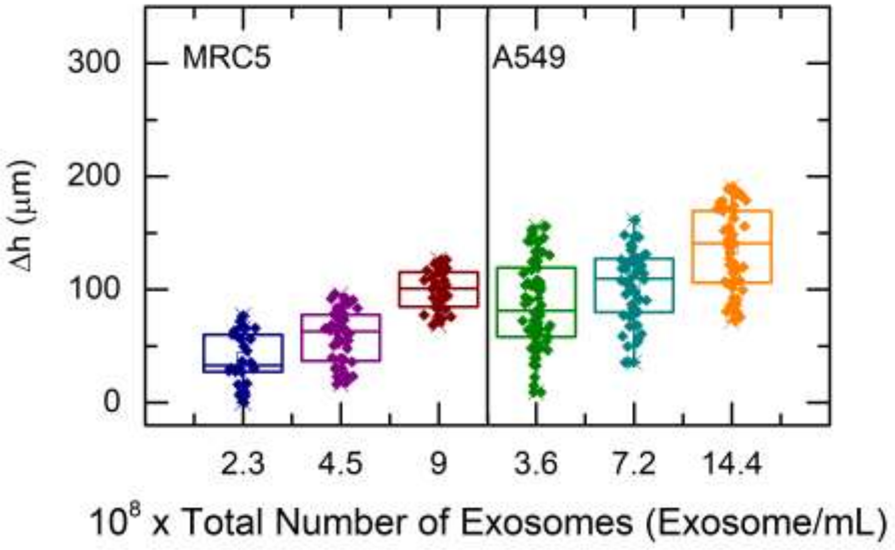

Figure 86. Exosome detection via anti-EpCAM Ab functionalized PSMs with through MagLev sensor platform.

Both cell line derived exosomes caused a significant decrease in Δh values, and A549 derived exosomes caused a higher decrease. Moreover, there was a significant increase in standard deviation of beads when exosome samples were introduced, and this suggests that exosome-bead interaction might not be homogenous. Increase in the deviation might be investigated and possibly correlated with decrease in sample concentration. Next, descriptive statistics and normality tests were carried out for the acquired data. Table 13 summarizes the relevant results.

Table 13. Exosome detection via anti-EpCAM functionalized PSMs, mean value and standard deviation of magnetic levitation heights and Kolmogorov-Smirnov normality test results.

	MRC5				A549		
Exo Number (x 10^9)	Mean	Std. Dev.	p-value	Exo Number (x 10^9)	Mean	Std. Dev.	p-value
Control	428.320	24.803	0.685	Control	492.242	30.844	0.684
0.90	396.124	30.341	0.109	1.44	392.098	29.631	0.731
0.45	405.062	35.141	0.547	0.72	411.350	29.631	0.326
0.23	451.148	20.154	0.106	0.36	428.323	45.926	0.310

As the table suggests each exosome derived cell line sample showed a normal distribution. One-way ANOVA analyses were carried out next with the Tukey post-hoc test for multiple comparisons. One way ANOVA results showed that the population means are significantly different [F (5, 301) = 57.41] at the 0.05 level. Tukey post-hoc tests were run, and Tukey's Honest Significant Difference (HSD) showed that there is a significant difference of means between all consecutive pairwise comparisons at the 0.05 level, and also comparison of same dilution factor for different cell line derived exosomes. This shows that the developed platform showed successful performance both in distinguishing cancerous and healthy cell line derived exosomes and distinguishing exosome samples with different concentrations.

Next, MagLev sensor platform was utilized to detect CD81 protein containing exosomes. For this purpose, PSMs were functionalized with anti-CD81 Ab and 0.5, 0.25, and 0.125 dilution factors were used for *in-vitro* exosomes, as previously done. Figure 87 shows the results of detection for A549 NSCLC cell line derived exosomes in comparison to MRC5 as a healthy control.

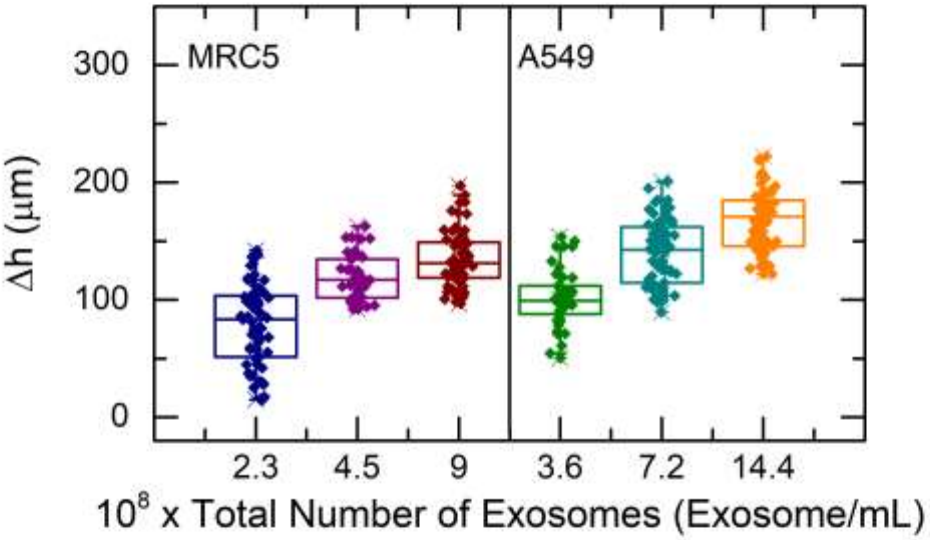

Figure 87. Exosome detection via anti-CD81 Ab functionalized PSMs with through MagLev sensor platform.

Both cell line derived exosomes caused a significant decrease in Δh values, and A549 derived exosomes caused a greater decrease in magnetic levitation height of PSMs. Comparing to the EpCAM results the difference between cell lines was smaller. Since, CD81 is an exosomal biomarker as opposed to EpCAM being a cancerous exosomal biomarker it was expected to see a higher decrease in MagLev height in healthy cell line derived exosomes here (Halvaei et al. 2018). Moreover, there was a significant increase in standard deviation of PSMs when exosome samples as were in EpCAM results.

Next, descriptive statistics and normality tests were carried out for the acquired data. Table 14 summarizes the relevant results for both cell lines A549 and MRC5. As the table shows, the increase in the standard deviation was similar to previous detection study. Each sample showed normal distribution and results indicate that for both cell lines there is a significant amount of exosome synthesis.

Table 14. Exosome detection via anti-CD81 functionalized PSMs, mean value and standard deviation of magnetic levitation heights and Kolmogorov-Smirnov normality test results.

	MRC5				A549		
Exo Number (x 10^9)	Mean	Std. Dev.	p-value	Exo Number (x 10^9)	Mean	Std. Dev.	p-value
Control	485.749	35.781	0.118	Control	542.263	71.111	0.726
0.90	377.600	22.496	0.571	1.44	473.419	38.191	0.932
0.45	387.838	21.064	0.985	0.72	514.252	45.381	0.641
0.23	433.029	37.736	0.972	0.36	517.118	78.160	0.631

Compared to A549 cell line, assuming each cell lines' exosomes contain similar amount of CD81 protein, MRC5 cell line synthesized a lower number of exosomes, which was in correlation with exosome characterization study that was carried on in this study previously. One way ANOVA results showed that the population means are significantly different [F (5, 308) = 80.06] at the 0.05 level. Tukey post-hoc tests were run, and Tukey's Honest Significant Difference (HSD) showed that there is a significant difference of means between all comparisons of same dilution factor for different cell line derived exosomes.

MagLev experiments were then conducted using CD151 Ab functionalized PSMs and acquired results can be seen in Figure 88. Literature reported that blood samples obtained from NSCLC patients showed a significant increase in expression of CD151 in their exosomes (Sandfeld-Paulsen, Jakobsen, et al. 2016; Sandfeld-Paulsen, Aggerholm-Pedersen, et al. 2016). Hence, CD151 was targeted as a cancer biomarker in this study. The highest Δh value was obtained from A549 cell line derived exosomes, whereas no significant Δh difference was encountered when samples isolated from MRC5 analyzed, since those are healthy cell lines. The acquired outcome was in parallel with clinical studies in literature; a greater amount of CD151 was observed in exosomes generated by NSCLC cell line A549 compared to healthy cell lines; this was also validated via immunostaining previously.

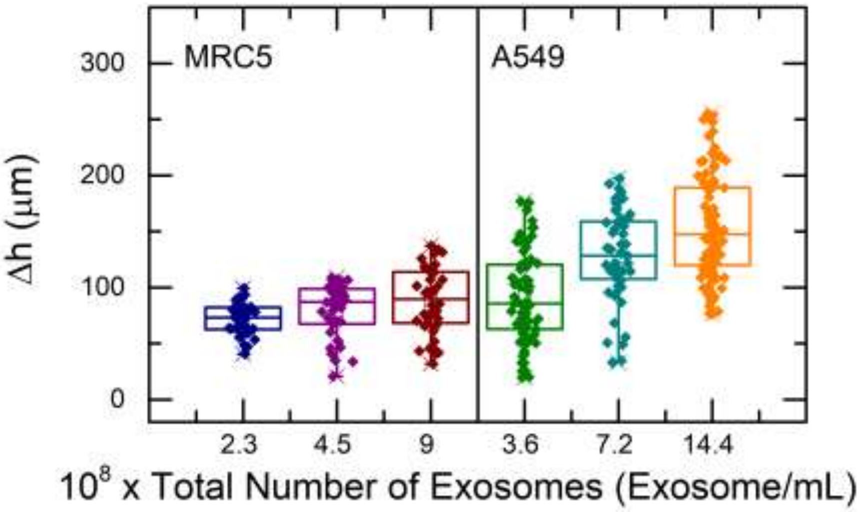

Figure 88. Exosome detection via anti-CD151 Ab functionalized PSMs with through MagLev sensor platform.

Lastly, descriptive statistical analyses and normality test were run for samples and Table 15 includes the descriptive statistical analyses and normality test results for CD151 containing exosome detection in both cancerous and healthy cell line derived exosomes. As seen in the table all data sets showed normal distribution for Kolmogorov-Smirnov normality test. Then, one-way ANOVA was applied to further investigate the difference of the means of samples. One way ANOVA results showed that the population means are indeed significantly different [F (5, 327) = 45.39] at the 0.05 level. Tukey post-hoc tests were run and Tukey post-hoc tests were run, and Tukey's Honest Significant Difference (HSD) showed that there is a significant difference of means between all comparisons of same dilution factor for different cell line derived exosomes. Also, there was no significant difference encountered between MRC5 dilution rates, indicating a much lower number of exosomes that include CD151 membrane protein compared to A549 cell line derived samples. Consequently, the analyses showed that it was possible to distinguish exosomes gathered from A549 cell line and MRC5 cell line utilizing anti-CD151 functionalized PSMs.

Table 15. Exosome detection via anti-CD151 functionalized PSMs, mean value and standard deviation of magnetic levitation heights and Kolmogorov-Smirnov normality test results.

	MRC5				A549		
Exo Number (x 10^9)	Mean	Std. Dev.	p-value	Exo Number (x 10^9)	Mean	Std. Dev.	p-value
Control	406.855	43.305	1	Control	540.001	13.410	0.422
0.90	372.406	51.119	1	1.44	411.145	49.898	1
0.45	394.714	23.666	0.244	0.72	427.370	51.415	0.824
0.23	397.660	17.887	0.456	0.36	464.930	54.750	0.744

Overall, the results obtained functionalized PSMs were used as capturing agents. All data collected from the experiment showed a normal distribution and ANOVA analysis that were performed revealed statistically significant differences between the populations in terms of their means ($p < .05$). As shown in the figure, A549 had the a much greater expression of CD81 protein which was in correlation with immunostaining results. Also, as described in the literature, cancerous cells generate a greater number of exosomes compared to healthy ones, as encountered in this study (L. Zhang and Yu 2019).EpCAM detection in samples were also concluded in similar results, with A549 having a greater Δh value, indicating a higher number of EpCAM containing exosome secretion in cancerous cell line.

Lastly, an immunostaining study was carried out directly on utilized PSMs as described previously with the same Ab combination on PSMs after exosome capturing end detection was concluded. Figure 89 shows the acquired results.

Immunostaining was carried out to determine the proteins utilizing the same Abs that were used during the study for functionalizing both LSPR and MagLev biosensor platforms. CD81 and CD151, red color indicates stained exosomes, and it is evident that PSMs capture more exosomes when samples from A549 cell line were utilized for detection studies. This verifies the results acquired so far with both LSPR and MagLev sensor platforms.

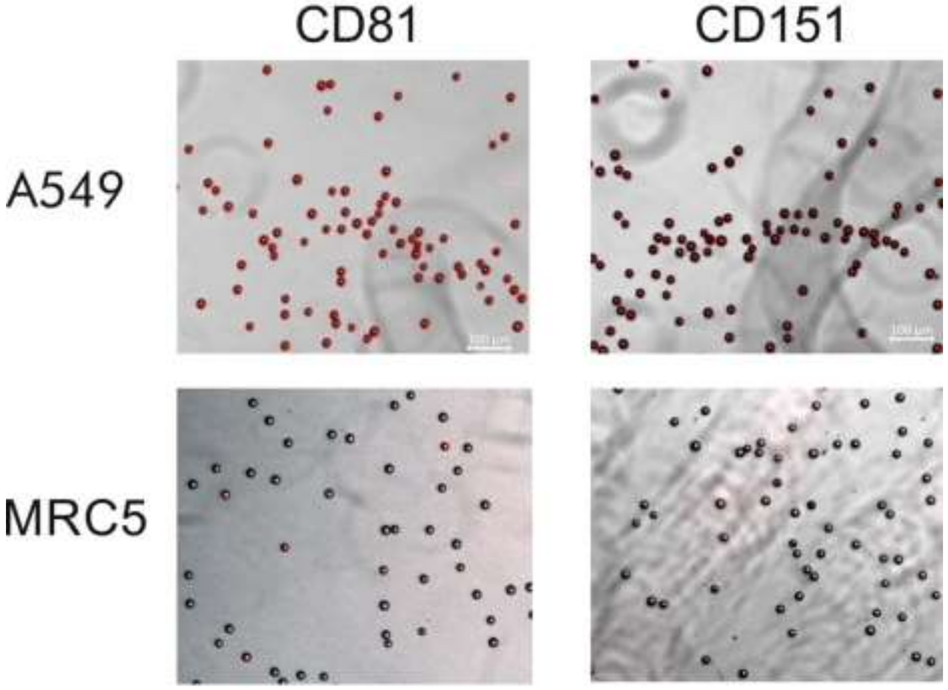

Figure 89. Microscopy images of immunostained exosomes attached to PSMs that were used to capture said exosomes.

Literature reported that blood samples obtained from NSCLC patients showed a significant increase in expression of CD151 in their exosomes (J. Zhu et al. 2021; Sandfeld-Paulsen, Aggerholm-Pedersen, et al. 2016; Jakobsen et al. 2015; Pérez-Callejo et al. 2016)Hence, CD151 was targeted as a cancer biomarker in this study. The highest Δh value was obtained from A549 cell line derived exosomes, whereas no significant Δh difference was encountered when samples isolated from MRC5 were analyzed. The acquired outcome was in parallel with clinical studies in the literature; a greater amount of CD151 was observed in exosomes generated by NSCLC cell line A549 compared to healthy cell line; this was also validated via immunostaining.

CHAPTER 4

CONCLUSION

The main goal of the thesis was to develop alternative optical biosensor platforms for prognosis, diagnosis, and monitoring of cancer targeting exosomal membrane proteins as biomarkers in the context of future liquid biopsy applications. The main cause of this motivation is that the current technologies to prognose, diagnose or monitor cancer are not effective at early-stages of cancer; they are either not reliable, or too invasive for casual check-up procedures. These obstacles hinder the early-diagnosis possibility of cancer, which leads to lack or delay of treatment. For this purpose, Non-Small Cell Lung Cancer (NSCLC) is selected as a model, due to the lack of early diagnosis with current methodologies. Also, it has a well-defined membrane protein profile in the current literature which can act as a robust starting point.

The detection procedures were planned to be carried out via Localized Surface Plasmon Resonance (LSPR) and Magnetic Levitation (MagLev) methodologies. The prior utilizes the ability of gold nanoparticles (GNPs) to resonate with an incident light when certain pre-requirements are met; such as light polarization and resonance angle, which brings particles to be fine sensors of local refractive index. The latter exploits fine density differences between particles for detection assays. The fundamental of the method involves employing microspheres of established densities and assessing their levitation heights within the MagLev sensor platform. Subsequently, a calibration curve is constructed using the acquired data, with density plotted on the Y-axis and height or vertical position on the X-axis. Finally, the analyte under analysis is introduced into the system and levitated, and its levitation height is compared against the calibration curve to ascertain its density, utilizing the pre-existing data obtained from the standard PSMs.

Overall, two optical biosensor platforms with separate detection principles were developed, optimized, characterized, and utilized for exosome detection with the aim of reaching a promising applicability for future liquid biopsy applications. After the optimization steps were carried out both platforms proved effective in detecting and quantifying specific exosomal membrane proteins; CD81, EpCAM, and CD151, and exosomes containing those proteins which were isolated from cancerous and healthy cell lines.

The development of LSPR based biosensor platform started with BSA detection as a model protein and immobilized GNPs (*i*-GNPs) as transducers. Whereas its initial sensitivity and working range appeared unsatisfactory, so that optimization procedures were followed, this started with optimization of GNP synthesis and immobilization. Afterwards, syntheses of various NP properties were carried out via well-established, modified, and novel methods for tuning of NPs during the study. The synthesized NPs were characterized via SEM imaging, EDX analyses, UV-Vis spectrum and DLS measurements and optimization was done with reaction time, reactant concentration and ratios as parameters. Effectivity of the sensitivity enhancement was then tested via a model protein detection assay. Synthesized NPs were then immobilized into well plates separately for biosensor applications to increase sensitivity, reusability, stability and reduced background signals. Moreover, various tuning applications were carried out for several NPs such as in-situ size growth and coating for further tuning. Afterwards, NPs were functionalized with anti-BSA protein and protein detection was observed via the shift in λ_{max} measured. The highest sensitivity was observed in core-shell gold-silver NPs, λ_{max} shift increased more than ten-fold compared to conventionally utilized LSPR techniques. The highest sensitivity among core-shell NPs was encountered when 65% gold to silver ratio was used for the synthesis; Limit of Detection (LoD) value of 27.5 nM and a dynamic linear working range between 62.5 - 1000 nM was calculated. Detection of target membrane proteins were then carried out. The detection procedure was followed for EpCAM, CD81, and CD151 and LoD values were calculated 0.43 nM and LoQ to be 1.32 nM, respectively.

The development of MagLev based biosensor platform started with determination of microsphere (PSM) size and dilution rate; and concentration optimization of Ab functionalization. Conclusively, it was determined that PSMs with a diameter of 20 μm at a concentration of 0.005% (W/V), functionalized with anti-BSA antibodies at a concentration of 25 μg/mL, exhibited superior resolution and sensitivity. These parameters were consequently employed for the remainder of this study to ensure enhanced reliability and reproducibility. Utilizing the developed system, density-based detection and quantification of BSA was successfully carried out as a model protein, achieving a dynamic range of 100 nM to 1 mM, with a LoD value of 62.04 nM. The magnetic levitation-based biosensor platform demonstrated good potential for protein detection and quantification, offering simple, rapid, cost-effective, and highly sensitive results of significant importance. Density-based detection and quantification of target membrane proteins were conducted using the developed biosensor platform, revealing a dynamic range of 1 – 100 nM with Limit of Detection (LoD) values of 1.324, 0.638, and 0.722 nM for EpCAM, CD81, and CD151, respectively.

Lastly, both biosensor platforms were utilized for detection of *in-vitro* exosomes isolated from MRC5 healthy lung fibroblast cells and A549 NSCLC cell line. Isolated exosomes were diluted serially, and detection procedures were carried out. It was evident that both sensor platforms were able to differentiate between cancerous and healthy cell lines down to $2*10^8$ particles/mL. All data acquires throughout exosome detection study were subjected to ANOVA and post-hoc tests which supported the results. A549 had the highest expression of EpCAM, CD81, and CD151 which was in correlation with immunostaining results. Also, as described in the literature, cancerous cells generate a greater number of exosomes compared to healthy ones, as encountered in this study.

Overall, two optical biosensor platforms were developed and were utilized for detection of exosomes with specific membrane proteins. Throughout the study, fabrication and optimization of said platforms were carried out utilizing several approaches and these applications were verified via characterization of sensor platforms using various assays, devices, and procedures. Thus, it was possible to exhibit current state of the biosensor platform, which promises further applications in the field, and both platforms promise; with further investigation, development, and labor, they one day may pave the road for a sensitive, feasible, applicable, and easily accessible liquid biopsy methodology for cancer prognosis, diagnosis, and monitoring.

REFERENCES

Amendola, Vincenzo, and Moreno Meneghetti. **2009**. “Size Evaluation of Gold Nanoparticles by UV-Vis Spectroscopy.” *Journal of Physical Chemistry C 113* (11): 4277–85. https://doi.org/10.1021/JP8082425

Amin, Reza, Stephanie Knowlton, Bekir Yenilmez, Alexander Hart, Ashwini Joshi, and Savas Tasoglu. **2016**. “Smart-Phone Attachable, Flow-Assisted Magnetic Focusing Device.” *RSC Advances 6* (96): 93922–31. https://doi.org/10.1039/c6ra19483d.

Ashkarran, Ali Akbar, and Morteza Mahmoudi. **2021**. “Magnetic Levitation Systems for Disease Diagnostics.” *Trends in Biotechnology 39* (3): 311–21. https://doi.org/10.1016/j.tibtech.2020.07.010.

Bastos, N, C F Ruivo, S da Silva, and S A Melo. **2018**. “Exosomes in Cancer: Use Them or Target Them?” *Semin Cell Dev Biol 9* (78):13–21. https://doi.org/10.1016/j.semcdb.2017.08.009.

Bingham, Julia M, W Paige Hall, and Richard P Van Duyne. **2012**. “Exploring the Unique Characteristics of LSPR Biosensing.” In *Nanoplasmonic Sensors, 2,* pp 29–58. https://doi.org/10.1007/978-1-4614-3933-2_2.

BioTek Instruments, Inc., ed. **2021**. “Protein Analysis Using Microplate-Based Quantification Methods.” *BioTek Instruments, Inc.* www.agilent.com/lifesciences/biotek.

Bloxham, William H, Jonathan W Hennek, Ashok A Kumar, and George M Whitesides. **2015**. “Fractionating Polymer Microspheres as Highly Accurate Density Standards.” *Anal. Chem. 87* (14): 7485–7491. https://doi.org/10.1021/acs.analchem.5b01932

Borah, Rituraj, and Sammy W. Verbruggen. **2020**. “Silver-Gold Bimetallic Alloy versus Core-Shell Nanoparticles: Implications for Plasmonic Enhancement and Photothermal Applications.” *Journal of Physical Chemistry C 124* (22): 12081–94. https://doi.org/10.1021/

Bray, F, J Ferlay, I Soerjomataram, R L Siegel, L A Torre, and A Jemal. **2018**. “Global Cancer Statistics 2018: GLOBOCAN Estimates of Incidence and Mortality

Worldwide for 36 Cancers in 185 Countries.” *CA Cancer J Clin 68* (6): 394–424. https://doi.org/10.3322/caac.21492.

Brown, Kenneth R., L. Andrew Lyon, Audrey P. Fox, Brian D. Reiss, and Michael J. Natan. **2000**. “Hydroxylamine Seeding of Colloidal Au Nanoparticles. 3. Controlled Formation of Conductive Au Films.” *Chemistry of Materials 12* (2): 314–23. https://doi.org/10.1021/CM980066H.

Brown, Kenneth R., and Michael J. Natan. **1998**. “Hydroxylamine Seeding of Colloidal Au Nanoparticles in Solution and on Surfaces.” *Langmuir 14* (4): 726–28. https://doi.org/10.1021/LA970982U.

Brown, Kenneth R., Daniel G. Walter, and Michael J. Natan. **2000**. “Seeding of Colloidal Au Nanoparticle Solutions. 2. Improved Control of Particle Size and Shape.” *Chemistry of Materials 12* (2): 306–13. https://doi.org/10.1021/CM980065P.

Campbell, J M, J B Balhoff, G M Landwehr, S M Rahman, M Vaithiyanathan, and A T Melvin. **2018**. “Microfluidic and Paper-Based Devices for Disease Detection and Diagnostic Research.” *Int J Mol Sci 19* (9): 2731 https://doi.org/10.3390/ijms19092731.

Cataldi, Ugo, Roberto Caputo, Yuriy Kurylyak, Gérard Klein, Mahshid Chekini, Cesare Umeton, and Thomas Bürgi. **2014**. “Growing Gold Nanoparticles on a Flexible Substrate to Enable Simple Mechanical Control of Their Plasmonic Coupling.” *Journal of Materials Chemistry C 2* (37): 7927–33. https://doi.org/10.1039/C4TC01607F.

Chang, Chiao-Yun, Hsiang-Ting Lin, Ming-Sheng Lai, Teng-Yi Shieh, Chien-Chung Peng, Min-Hsiung Shih, and Yi-Chung Tung. **2018**. “Flexible Localized Surface Plasmon Resonance Sensor with Metal–Insulator–Metal Nanodisks on PDMS Substrate.” *Scientific Reports 8* (1): 11812. https://doi.org/10.1038/s41598-018-30180-8.

Cheng, N, D Du, X Wang, D Liu, W Xu, Y Luo, and Y Lin. **2019**. “Recent Advances in Biosensors for Detecting Cancer-Derived Exosomes.” *Trends Biotechnol. 37* (11): 1236 – 1254, https://doi.org/10.1016/j.tibtech.2019.04.008.

Cheol Kim, Sung, Navneet Dogra, Benjamin H Wunsch, Joshua T Smith, Stacey M Gifford, Gustavo Stolovitzky, Huan Hu, and Pablo Meyer. **2017**. “On-Chip Liquid Biopsy: Progress in Isolation of Exosomes for Early Diagnosis of

Cancer." *Biophysical Journal 112* (3): 461 . https://doi.org/10.1016/j.bpj.2016.11.2470.

Cocucci, E, and J Meldolesi. **2015**. "Ectosomes and Exosomes: Shedding the Confusion between Extracellular Vesicles." *Trends Cell Biol 25* (6): 364–72. https://doi.org/10.1016/j.tcb.2015.01.004.

Devhare, P B, and R B Ray. **2018**. "Extracellular Vesicles: Novel Mediator for Cell to Cell Communications in Liver Pathogenesis." *Mol Aspects Med 11* (60):115–22. https://doi.org/10.1016/j.mam.2017.11.001.

Dikkumbura, Asela S, Prakash Hamal, Min Chen, Daniel A Babayode, Jeewan C Ranasinghe, Kenneth Lopata, and Louis H Haber. **2021**. "Growth Dynamics of Colloidal Silver−Gold Core−Shell Nanoparticles Studied by In Situ Second Harmonic Generation and Extinction Spectroscopy." *J. Phys. Chem. C 46* (125):31. https://doi.org/10.1021/acs.jpcc.1c06094.

Durmus, N G, H C Tekin, S Guven, K Sridhar, A Arslan Yildiz, G Calibasi, I Ghiran, R W Davis, L M Steinmetz, and U Demirci. **2015**. "Magnetic Levitation of Single Cells." *Proc Natl Acad Sci U S A 112* (28): E3661-8. https://doi.org/10.1073/pnas.1509250112.

Dušek, František, Jiří Tuček, Aleš Novotný, and Daniel Honc. **2023**. "Generalized First-Principle Model of Magnetic Levitation." *Journal of Magnetism and Magnetic Materials 1* (587):171330. https://doi.org/10.1016/j.jmmm.2023.171330.

Elveren, Beste, and Ahu Arslan Yıldız. "Green Synthesis Of Metal Nanoparticles And Their Applications As Plasmonic Substrates." MSc Dissertation, Izmir Institute of Technology, İzmir, **2018**, https://hdl.handle.net/11147/7014

Englebienne, Patrick. **1998**. "Use of Colloidal Gold Surface Plasmon Resonance Peak Shift to Infer Affinity Constants from the Interactions between Protein Antigens and Antibodies Specific for Single or Multiple Epitopes." *Analyst 123* (7): 1599-1603 10.1039/a804010i.

Eskiköy Bayraktepe, Dilek, Ceren Yıldız, and Zehra Yazan. **2023**. "The Development of Electrochemical DNA Biosensor Based on Poly-L-Methionine and Bimetallic AuPt Nanoparticles Coating: Picomolar Detection of Imatinib and Erlotinib." *Talanta 257* (15): 124361. https://doi.org/10.1016/J.TALANTA.2023.124361.

Farooqi, A A, N N Desai, M Z Qureshi, D R N Librelotto, M L Gasparri, A Bishayee, S M Nabavi, V Curti, and M Daglia. **2018**. “Exosome Biogenesis, Bioactivities and Functions as New Delivery Systems of Natural Compounds.” *Biotechnol Adv 36* (1): 328–34. https://doi.org/10.1016/j.biotechadv.2017.12.010.

Fischer, H, I Polikarpov, and A F Craievich. **2004**. “Average Protein Density Is a Molecular-Weight-Dependent Function.” *Protein Sci 13* (10): 2825–28. https://doi.org/10.1110/ps.04688204.

Gholizadeh, S, M Shehata Draz, M Zarghooni, A Sanati-Nezhad, S Ghavami, H Shafiee, and M Akbari. **2017**. “Microfluidic Approaches for Isolation, Detection, and Characterization of Extracellular Vesicles: Current Status and Future Directions.” *Biosens Bioelectron 1* (91): 588–605. https://doi.org/10.1016/j.bios.2016.12.062.

Greening, D W, R Xu, H Ji, B J Tauro, and R J Simpson. **2015**. “A Protocol for Exosome Isolation and Characterization: Evaluation of Ultracentrifugation, Density-Gradient Separation, and Immunoaffinity Capture Methods.” *Methods Mol Biol 15* (1295): 179–209. https://doi.org/10.1007/978-1-4939-2550-6_15.

Halvaei, S, S Daryani, S Z Eslami, T Samadi, N Jafarbeik-Iravani, T O Bakhshayesh, A K Majidzadeh, and R Esmaeili. **2018**. “Exosomes in Cancer Liquid Biopsy: A Focus on Breast Cancer.” *Mol Ther Nucleic Acids 1* (10):131–41. https://doi.org/10.1016/j.omtn.2017.11.014.

Hamidi-Asl, Ezat, Freddy Dardenne, Sanaz Pilehvar, Ronny Blust, and Karolien De Wael. **2016**. “Unique Properties of Core Shell Ag@Au Nanoparticles for the Aptasensing of Bacterial Cells.” *Chemosensors 4 (*3): 16. https://doi.org/10.3390/CHEMOSENSORS4030016.

Haq, Isma, Alvaro Garcia Cruz, Sabrina Di Masi, Todd Cowen, Natalie S. Allcock, Cosimino Malitesta, Adnan Mujahid, Tajamal Hussain, Elena Piletska, and Sergey A. Piletsky. **2023**. “Smart Nano-Actuators for Electrochemical Sensing of Metformin in Human Plasma.” *Sensors and Actuators B: Chemical 376* (B): 132928 https://doi.org/10.1016/J.SNB.2022.132928.

Haxha, Shyqyri, Ahmed Teyeb, Fathi Abdel Malek, Emmanuel Kofi Akowuah, and Iyad Dayoub. **2015**. “Design of Environmental Biosensor Based on Photonic Crystal Fiber with Bends Using Finite Element Method.” *Optics and Photonics Journal 5* (03): 69–78. https://doi.org/10.4236/opj.2015.53006.

He, Jun, Zihan Wu, and Ming Sun. **2019**. “Using Gold Nanoparticles with Spectroscopic and Analytical Models for Rapid Colorimetric Detection of

Mercury Ions in Aqueous Media.” *Medziagotyra 25* (2): 121–28. https://doi.org/10.5755/j01.ms.25.2.19140.

He, M, and Y Zeng. **2016**. “Microfluidic Exosome Analysis toward Liquid Biopsy for Cancer.” *J Lab Autom 21* (4): 599–608. https://doi.org/10.1177/2211068216651035.

He, Mei, Jennifer Crow, Marc Roth, Yong Zeng, and Andrew K. Godwin. **2014**. “Integrated Immunoisolation and Protein Analysis of Circulating Exosomes Using Microfluidic Technology.” *Lab on a Chip 14* (19): 3773–80. https://doi.org/10.1039/c4lc00662c.

Hemler, M E. **2005**. “Tetraspanin Functions and Associated Microdomains.” *Nat Rev Mol Cell Biol 6* (10): 801–11. https://doi.org/10.1038/nrm1736.

Huang, L, W Ma, Y Ma, D Feng, H Chen, and B Cai. **2015**. “Exosomes in Mesenchymal Stem Cells, a New Therapeutic Strategy for Cardiovascular Diseases?” *Int J Biol Sci 11* (2): 238–45. https://doi.org/10.7150/ijbs.10725.

Huang, S H, Y Li, J Zhang, J Rong, and S Ye. **2013**. “Epidermal Growth Factor Receptor-Containing Exosomes Induce Tumor-Specific Regulatory T Cells.” *Cancer Invest 31* (5): 330–35. https://doi.org/10.3109/07357907.2013.789905

.

Im, H, H Shao, Y I Park, V M Peterson, C M Castro, R Weissleder, and H Lee. **2014**. “Label-Free Detection and Molecular Profiling of Exosomes with a Nano-Plasmonic Sensor.” *Nat Biotechnol 32* (5): 490–95. https://doi.org/10.1038/nbt.2886.

Im, H, H Shao, R Weissleder, C M Castro, and H Lee. **2015**. “Nano-Plasmonic Exosome Diagnostics.” *Expert Rev Mol Diagn 15* (6): 725–33. https://doi.org/10.1586/14737159.2015.1041378.

Jakobsen, K R, B S Paulsen, R Baek, K Varming, B S Sorensen, and M M Jorgensen. **2015**. “Exosomal Proteins as Potential Diagnostic Markers in Advanced Non-Small Cell Lung Carcinoma.” *J Extracell Vesicles 1* (4):26659. https://doi.org/10.3402/jev.v4.26659.

Jalalian, Seyed Hamid, Mohammad Ramezani, Seyed Ali Jalalian, Khalil Abnous, and Seyed Mohammad Taghdisi. **2019**. “Exosomes, New Biomarkers in Early Cancer Detection.” *Analytical Biochemistry 1* (571):1–13. https://doi.org/10.1016/j.ab.2019.02.013.

Jorgensen, M, R Baek, S Pedersen, E K Sondergaard, S R Kristensen, and K Varming. **2013**. “Extracellular Vesicle (EV) Array: Microarray Capturing of Exosomes and Other Extracellular Vesicles for Multiplexed Phenotyping.” *J Extracell Vesicles 1* (2): 20920 https://doi.org/10.3402/jev.v2i0.20920.

Kanwar, S S, C J Dunlay, D M Simeone, and S Nagrath. **2014**. “Microfluidic Device (ExoChip) for on-Chip Isolation, Quantification and Characterization of Circulating Exosomes.” *Lab Chip 14* (11): 1891–1900. https://doi.org/10.1039/c4lc00136b.

Khamehchian, S, R Madani, F Golchinfar, and M Taghavian. **2008**. “Development of a Sandwich Enzyme-Linked Immunosorbent Assay (ELISA) for Determining of Bovine Serum Albumin (BSA) in Trivalent Measles-Mump-Rubella (MMR) Vaccines.” *Hum Vaccin 4* (5): 375–78. https://doi.org/10.4161/hv.4.5.6009.

Kimling, J, M Maier, B Okenve, V Kotaidis, H Ballot, and A Plech. **2006**. “Turkevich Method for Gold Nanoparticle Synthesis Revisited.” *J Phys Chem B 110* (32): 15700–707. https://doi.org/10.1021/jp061667w.

Kumar, Sanjeev, K. S. Gandhi, and R. Kumar. **2007**. “Modeling of Formation of Gold Nanoparticles by Citrate Method.” *Industrial and Engineering Chemistry Research 46* (10): 3128–36. https://doi.org/10.1021/IE060672J.

Laithwaite, Eric R. **1975**. “Linear Electric Machines- A Personal View.” *Proceedings Of The IEEE,* 63

Li, W, C Li, T Zhou, X Liu, X Liu, X Li, and D Chen. **2017**. “Role of Exosomal Proteins in Cancer Diagnosis.” *Mol Cancer 16* (1): 145. https://doi.org/10.1186/s12943-017-0706-8

Li, X, M Ye, W Zhang, D Tan, N Jaffrezic-Renault, X Yang, and Z Guo. **2019a**. “Liquid Biopsy of Circulating Tumor DNA and Biosensor Applications.” *Biosens Bioelectron 12* (126):596–607. https://doi.org/10.1016/j.bios.2018.11.037

Liang, Yansheng, Shaohui Yan, Zhaojun Wang, Baoli Yao, and Ming Lei. **2021**. “Off-Axis Optical Levitation and Transverse Spinning of Metallic Microparticles.” *Photonics Research 9* (11): 2144-2151. https://doi.org/10.1364/prj.431413

Liu, Linlin, Abhimanyu Thakur, Wing Kar Li, Guangyu Qiu, Tian Yang, Bing He, Youngjin Lee, and Chi Man Lawrence Wu. **2022**. “Site Specific Biotinylated Antibody Functionalized Ag@AuNIs LSPR Biosensor for the Ultrasensitive Detection of Exosomal MCT4, a Glioblastoma Progression Biomarker.” *Chemical Engineering Journal 446* (1): 137383. https://doi.org/10.1016/J.CEJ.2022.137383

Loiseau, Alexis, Lu Zhang, David Hu, Michèle Salmain, Yacine Mazouzi, Raphaël Flack, Bo Liedberg, and Souhir Boujday. **2019**. “Silver Nanoparticles for Localized Surface Plasmon Resonance-Based Naked-Eye Toxin Biosensing.” *ACS Ap-Plied Materials & Interfaces 11* (50): 27513 https://doi.org/10.1021/acsami.9b14980ï

Lu, Lu, Gwendolyn Burkey, Ionel Halaciuga, and Dan V. Goia. **2013**. “Core–Shell Gold/Silver Nanoparticles: Synthesis and Optical Properties.” *Journal of Colloid and Interface Science 392* (1): 90–95. https://doi.org/10.1016/J.JCIS.2012.09.057.

Lyu, Chenxin, Daofan Tang, Chengqian Zhang, Jun Xie, Qingyan Zhang, Jing Nie, Yong He, Jianzhong Fu, Jingdai Wang, and Peng Zhao. **2023**. “Magnetic Levitation for Non-Contact Manipulation and Measurement of Cells.” *1* (385): 133692 https://doi.org/10.1016/j.snb.2023.133692.

Magnusson, B, and U Örnemark. “Eurachem Guide: The Fitness for Purpose of Analytical Methods - A Laboratory Guide to Method Validation Related Topics.” Eurachem. **2014**, pp 13-47. https://www.eurachem.org/images/stories/Guides/pdf/MV_guide_2nd_ed_EN.pdf

Malassis, Ludivine, Rémi Dreyfus, Ryan J. Murphy, Lawrence A. Hough, Bertrand Donnio, and Christopher B. Murray. **2016**. “One-Step Green Synthesis of Gold and Silver Nanoparticles with Ascorbic Acid and Their Versatile Surface Post-Functionalization.” *RSC Advances 6* (39): 33092–100. https://doi.org/10.1039/C6RA00194G.

Mayer, K M, and J H Hafner. **2011**. “Localized Surface Plasmon Resonance Sensors.” *Chem Rev 111* (6): 3828–57. https://doi.org/10.1021/cr100313v.

Mehdiani, A, A Maier, A Pinto, M Barth, P Akhyari, and A Lichtenberg. **2015**. “An Innovative Method for Exosome Quantification and Size Measurement.” *Journal of Visualized Experiments : JoVE, 2* (95), 50974. https://doi.org/10.3791/50974.

Mignot, G, S Roux, C Thery, E Ségura, and L Zitvogel. **2006**. “Prospects for Exosomes in Immunotherapy of Cancer.” *J. Cell. Mol. Med. 10* (2): 376–88. doi: 10.1111/j.1582-4934.2006.tb00406.x.

Mirica, K A, S T Phillips, C R Mace, and G M Whitesides. **2010**. “Magnetic Levitation in the Analysis of Foods and Water.” *J Agric Food Chem 58* (11): 6565–69. https://doi.org/10.1021/jf100377n.

Mirica, Katherine A, Scott T Phillips, Sergey S Shevkoplyas, and George M Whitesides. **2008**. “Using Magnetic Levitation To Distinguish Atomic-Level Differences in Chemical Composition of Polymers, and To Monitor Chemical Reactions on Solid Supports.” *J. AM. CHEM. SOC. 130* (52): 17678 https://doi.org/10.1021/ja8074727

Mirica, Katherine A, Sergey S Shevkoplyas, Scott T Phillips, Malancha Gupta, and George M Whitesides. **2009**. “Measuring Densities of Solids and Liquids Using Magnetic Levitation: Fundamentals.” *J. AM. CHEM. SOC. 131* (29): 10049 https://doi.org/10.1021/ja900920s

Mozafari, M R, E Mazaheri, and K Dormiani. **2021**. “Simple Equations Pertaining to the Particle Number and Surface Area of Metallic, Polymeric, Lipidic and Vesicular Nanocarriers.” *Scientia Pharmaceutica 89* (2): 15 https://doi.org/10.3390/scipharm89020015

Nemiroski, A, A A Kumar, S Soh, D V Harburg, H D Yu, and G M Whitesides. **2016**. “High-Sensitivity Measurement of Density by Magnetic Levitation.” *Anal Chem 88* (5): 2666–74. https://doi.org/10.1021/acs.analchem.5b03918

Ong, Sandy Gim Ming, Mallikarjun Chitneni, Kah Seng Lee, Long Chiau Ming, and Kah Hay Yuen. **2016**. “Evaluation of Extrusion Technique for Nanosizing Liposomes.” *Pharmaceutics 8* (4): 36 https://doi.org/10.3390/PHARMACEUTICS8040036

Otto, Andreas. **1968**. “Excitation of Nonradiative Surface Plasma Waves in Silver by the Method of Frustrated Total Reflection.” *Zeitschrift Ffir Physik 1* (216):398–410 https://doi.org/10.1007/BF01391532

Ozefe, F, and A Arslan Yildiz. **2020**. “Smartphone-Assisted Hepatitis C Detection Assay Based on Magnetic Levitation.” *Analyst 145* (17): 5816–25. https://doi.org/10.1039/d0an01111h

Palmirotta, R, D Lovero, P Cafforio, C Felici, F Mannavola, E Pelle, D Quaresmini, M Tucci, and F Silvestris. **2018**. “Liquid Biopsy of Cancer: A Multimodal

Diagnostic Tool in Clinical Oncology.” *Ther Adv Med Oncol*. *10* (1): 1 https://doi.org/10.1177/1758835918794630

Pavlova, Galina Dimitrova. **2016**. “Isolation and Characterization of Cancer-Derived Exosomes.” *Department of Biosciences 13* (152): 1-24 https://doi.org/10.1186/s13045-020-00987-y

Perez-Callejo, D, A Romero, M Provencio, and M Torrente. **2016**. “Liquid Biopsy Based Biomarkers in Non-Small Cell Lung Cancer for Diagnosis and Treatment Monitoring.” *Transl Lung Cancer Res 5* (5): 455–65. https://doi.org/10.21037/tlcr.2016.10.07

Pérez-Callejo, David, Atocha Romero, Mariano Provencio, and María Torrente. **2016**. “Liquid Biopsy Based Biomarkers in Non-Small Cell Lung Cancer for Diagnosis and Treatment Monitoring.” *Translational Lung Cancer Research*. AME Publishing Company. *5* (5): 2226 https://doi.org/10.21037/tlcr.2016.10.07

Petryayeva, E, and U J Krull. **2011**. “Localized Surface Plasmon Resonance: Nanostructures, Bioassays and Biosensing--a Review.” *Anal Chim Acta 706* (1): 8–24. https://doi.org/10.1016/j.aca.2011.08.020.

Pol, E van der, A N Boing, P Harrison, A Sturk, and R Nieuwland. **2012**. “Classification, Functions, and Clinical Relevance of Extracellular Vesicles.” *Pharmacol Rev 64* (3): 676–705. https://doi.org/10.1124/pr.112.005983.

Prasad, Paras N. *Introduction to Biophotonics*. 1st ed. Wiley-Interscience **2003**.

Raether, H. “Surface Plasmons on Smooth Surfaces. In: Surface Plasmons on Smooth and Rough Surfaces and on Gratings.” *Springer Tracts in Modern Physics* 111. **1988**.

Raghu, D, J A Christodoulides, M Christophersen, J L Liu, G P Anderson, M Robitaille, J M Byers, and M P Raphael. **2018**. “Nanoplasmonic Pillars Engineered for Single Exosome Detection.” *PLoS One 13* (8): e0202773. https://doi.org/10.1371/journal.pone.0202773.

Roy, Alok, and Bidhan Mohanta. **2019**. “Green Synthesis of Gold-Silver Core-Shell Nanoparticles and Its Characterizations.” *Dae Solid State Physics Symposium 2018* (2112): 030181 https://doi.org/10.1063/1.5113020.

Sandfeld-Paulsen, B, N Aggerholm-Pedersen, R Baek, K R Jakobsen, P Meldgaard, B H Folkersen, T R Rasmussen, K Varming, M M Jorgensen, and B S Sorensen. **2016**. “Exosomal Proteins as Prognostic Biomarkers in Non-Small Cell Lung Cancer.” *Mol Oncol 10* (10): 1595–1602. https://doi.org/10.1016/j.molonc.2016.10.003.

Sandfeld-Paulsen, B, K R Jakobsen, R Baek, B H Folkersen, T R Rasmussen, P Meldgaard, K Varming, M M Jorgensen, and B S Sorensen. **2016**. “Exosomal Proteins as Diagnostic Biomarkers in Lung Cancer.” *J Thorac Oncol 11* (10): 1701–10. https://doi.org/10.1016/j.jtho.2016.05.034

Sau, Tapan K., Andrey L. Rogach, Markus Döblinger, and Jochen Feldmann. **2011**. “One-Step High-Yield Aqueous Synthesis of Size-Tunable Multispiked Gold Nanoparticles.” *Small 7* (15): 2188–94. https://doi.org/10.1002/smll.201100365.

Schasfoort, Richard B. M. *Schasfoort, Richard B. M. Handbook of Surface Plasmon Resonance*. 2nd ed, Royal Society of Chemistry. https://doi.org/10.1039/9781788010283-fp001. **2017**.

Selvakannan, P. R., Anita Swami, D. Srisathiyanarayanan, Pravin S. Shirude, Renu Pasricha, Anandrao B. Mandale, and Murali Sastry. **2004**. “Synthesis of Aqueous Au Core-Ag Shell Nanoparticles Using Tyrosine as a PH-Dependent Reducing Agent and Assembling Phase-Transferred Silver Nanoparticles at the Air-Water Interface.” *Langmuir 20* (18): 7825–7836 https://doi.org/10.1021/la049258j

Shandilya, Ruchita, Arpit Bhargava, Neha Bunkar, Rajnarayan Tiwari, Irina Yu Goryacheva, and Pradyumna Kumar Mishra. **2019**. “Nanobiosensors: Point-of-Care Approaches for Cancer Diagnostics.” *Biosensors and Bioelectronics*. *130* (1): 147-165 https://doi.org/10.1016/j.bios.2019.01.034

Shen, B, N Wu, J M Yang, and S J Gould. **2011**. “Protein Targeting to Exosomes/Microvesicles by Plasma Membrane Anchors.” *J Biol Chem 286* (16): 14383–14395. https://doi.org/10.1074/jbc.M110.208660.

Singh, Shefali, Abhishek Pathak, Sachin Kumar, Prabhat Singh Malik, and Ravikrishnan Elangovan. **2022**. “Rapid Immunomagnetic Co-Capture Assay for Quantification of Lung Cancer Associated Exosomes.” *Journal of Immunological Methods 508* (2): 113324. https://doi.org/10.1016/j.jim.2022.113324

Sood, Ankur, Varun Arora, Jyoti Shah, R K Kotnala, and Tapan K Jain. **2016**. “Ascorbic Acid-Mediated Synthesis and Characterisation of Iron Oxide/Gold Core-Shell Nanoparticles.) Ascorbic Acid-Mediated Synthesis and Characterisation of Iron Oxide/Gold Core-Shell Nanoparticles Ascorbic Acid-Mediated Synthesis and Characterisation of Iron Oxide/Gold CoreÀshell Nanoparticles.” *Journal of Experimental Nanoscience 11* (5): 370–82. https://doi.org/10.1080/17458080.2015.1066514

Sözmen, A. Baran, Beste Elveren, Duygu Erdogan, Bahadır Mezgil, Yalın Bastanlar, U. Hakan Yildiz, and Ahu Arslan Yildiz. **2024**. “Development of Chrono-Spectral Gold Nanoparticle Growth Based Plasmonic Biosensor Platform.” *Biosensors and Bioelectronics: X 16* (2): 100439. https://doi.org/10.1016/J.BIOSX.2024.100439

Steinbrück, Andrea, Ondrej Stranik, Andrea Csaki, and Wolfgang Fritzsche. **2011**. “Sensoric Potential of Gold-Silver Core-Shell Nanoparticles.” *Anal Bioanal Chem. 401* (1): 1241-1249 https://doi.org/10.1007/s00216-011-5177-y

Strimbu, K, and J A Tavel. **2010**. “What Are Biomarkers?” *Curr Opin HIV AIDS 5* (6): 463–66. https://doi.org/10.1097/COH.0b013e32833ed177.

Sudjarwo, W A A, M T Dobler, and P A Lieberzeit. **2021**. “QCM-Based Assay Designs for Human Serum Albumin.” *Anal Bioanal Chem. 414* (1): 731-741 https://doi.org/10.1007/s00216-021-03771-0

Suto, S, K D Tsuei, E W Plummer, and E Burstein. **1989**. “Surface-Plasmon Energy and Dispersion on Ag Single Crystals.” *Physical Review Letters 63* (23): 2590–93. https://doi.org/10.1103/PhysRevLett.63.2590

Tajfirooz, S, J G Meijer, R A Dellaert, A M Meulenbroek, J C H Zeegers, and J G M Kuerten. **2021**. “Direct Numerical Simulation of Magneto-Archimedes Separation of Spherical Particles.” *Journal of Fluid Mechanics 910*. (A52): 1-35 https://doi.org/10.1017/jfm.2020.1001

Tamura, R, and H Yin. **2017**. “Rationally Designed Peptide Probes for Extracellular Vesicles.” *Adv Clin Chem 1* (79): 25–41. https://doi.org/10.1016/bs.acc.2016.09.001

Taverna, S, M Giallombardo, I Gil-Bazo, A P Carreca, M Castiglia, J Chacartegui, A Araujo, et al. **2016**. “Exosomes Isolation and Characterization in Serum Is Feasible in Non-Small Cell Lung Cancer Patients: Critical Analysis of Evidence and Potential Role in Clinical Practice." *Oncotarget 7* (19): 28748–60. https://doi.org/10.18632/oncotarget.7638

Taylor, D D, and C Gercel-Taylor. **2008**. "MicroRNA Signatures of Tumor-Derived Exosomes as Diagnostic Biomarkers of Ovarian Cancer." *Gynecol Oncol 110* (1): 13–21. https://doi.org/10.1016/j.ygyno.2008.04.033

Thakur, Abhimanyu, Chen Xu, Wing Kar Li, Guangyu Qiu, Bing He, Siu Pang Ng, Chi Man Lawrence Wu, and Youngjin Lee. **2021**. "In Vivo Liquid Biopsy for Glioblastoma Malignancy by the AFM and LSPR Based Sensing of Exosomal CD44 and CD133 in a Mouse Model." *Biosensors and Bioelectronics 191* (1):113476. https://doi.org/10.1016/J.BIOS.2021.113476

Thompson, Marc T. **2000**. "Eddy Current Magnetic Levitation." *IEEE POTENTIALS. 19* (1): 40-44 https://doi.org/10.1109/45.825642

Tilley, D R. **1983**. "Surface Polaritons: Electromagnetic Waves at Surfaces and Interfaces." *Optica Acta: International Journal of Optics 30* (11): 1501. https://doi.org/10.1080/713821096

Turker, Esra, and Ahu Arslan-Yildiz. **2018**. "Recent Advances in Magnetic Levitation: A Biological Approach from Diagnostics to Tissue Engineering." *ACS Biomaterials Science & Engineering S* (3): 787–99. https://doi.org/10.1021/acsbiomaterials.7b00700

Turkevich, John, Peter Cooper Stevenson, and James Hillier. **1951**. "A Study of the Nucleation and Growth Processes in the Synthesis of Colloidal Gold." *Discussions of the Faraday Society 11* (0): 55–75. https://doi.org/10.1039/DF9511100055

Ueda, K, N Ishikawa, A Tatsuguchi, N Saichi, R Fujii, and H Nakagawa. **2014**. "Antibody-Coupled Monolithic Silica Microtips for Highthroughput Molecular Profiling of Circulating Exosomes." *Sci Rep 14* (4): 6232. https://doi.org/10.1038/srep06232

Unser, S, I Bruzas, J He, and L Sagle. **2015**. "Localized Surface Plasmon Resonance Biosensing: Current Challenges and Approaches." *Sensors (Basel)* 15 (7): 15684–716. https://doi.org/10.3390/s150715684

Valkonen, S, E van der Pol, A Boing, Y Yuana, M Yliperttula, R Nieuwland, S Laitinen, and P R Siljander. **2017**. "Biological Reference Materials for

Extracellular Vesicle Studies.” *Eur J Pharm Sci 1* (98) :4–16. https://doi.org/10.1016/j.ejps.2016.09.008

Wang, Qing, Liyuan Zou, Xiaohai Yang, Xiaofeng Liu, Wenyan Nie, Yan Zheng, Quan Cheng, and Kemin Wang. **2019**. “Direct Quantification of Cancerous Exosomes via Surface Plasmon Resonance with Dual Gold Nanoparticle-Assisted Signal Amplification.” *Biosensors and Bioelectronics 135* (1): 129-136 https://doi.org/10.1016/j.bios.2019.04.013

Whiteside, Theresa L. **2016**. “Tumor-Derived Exosomes and Their Role in Cancer Progression.” In *Advances in Clinical Chemistry, 16* (74):103–41. Academic Press Inc. https://doi.org/10.1016/bs.acc.2015.12.005.

Willets, Katherine A., and Richard P. Van Duyne. **2007**. “Localized Surface Plasmon Resonance Spectroscopy and Sensing.” *Annual Review of Physical Chemistry 17* (58):267–97. https://doi.org/10.1146/annurev.physchem.58.032806.104607

Wood, R W. **1902**. “XLII. On a Remarkable Case of Uneven Distribution of Light in a Diffraction Grating Spectrum.” *The London, Edinburgh, and Dublin Philosophical Magazine and Journal of Science 4* (21): 396–402. https://doi.org/10.1080/14786440209462857

Xiao, Y, Y Li, Y Yuan, B Liu, S Pan, Q Liu, X Qi, H Zhou, W Dong, and L Jia. **2019**. “The Potential of Exosomes Derived from Colorectal Cancer as a Biomarker.” *Clin Chim Acta 16* (490):186–93. https://doi.org/10.1016/j.cca.2018.09.007

Xu, R, A Rai, M Chen, W Suwakulsiri, D W Greening, and R J Simpson. **2018**. “Extracellular Vesicles in Cancer - Implications for Future Improvements in Cancer Care.” *Nat Rev Clin Oncol 15* (10): 617–38. https://doi.org/10.1038/s41571-018-0036-9

Yoon, Soon Joon, and Donghyun Kim. **2008**. “Target Dependence of the Sensitivity in Periodic Nanowire-Based Localized Surface Plasmon Resonance Biosensors.” *J. Opt. Soc. Am. A 25* (3): 725-735 https://doi.org/10.1364/JOSAA.25.000725

Yoshioka, Y, N Kosaka, Y Konishi, H Ohta, H Okamoto, H Sonoda, R Nonaka, et al. **2014**. “Ultra-Sensitive Liquid Biopsy of Circulating Extracellular Vesicles Using ExoScreen.” *Nat Commun 14* (5):3591. https://doi.org/10.1038/ncomms4591

Yuki Konakade Takeshi Yanagida Noritada Kaji Yong He Masaki Kanai Kazuki Nagashima Hiroshi Yukaw Tomoji Kawai Yoshinobu Baba, Takao Yasui. **2014**. “Exosomal Membrane Protein Detection by Nanowire Device.” *18th International Conference on Miniaturized Systems for Chemistry and Life Sciences*. San Antonio, Texas, USA

Zarei, M. **2017**. “Advances in Point-of-Care Technologies for Molecular Diagnostics.” *Biosens Bioelectron 9* (98):494–506. https://doi.org/10.1016/j.bios.2017.07.024

Zhang, C, P Zhao, F Gu, X Zhang, J Xie, Y He, H Zhou, J Fu, and L S Turng. **2020**. “Axial-Circular Magnetic Levitation: A Three-Dimensional Density Measurement and Manipulation Approach.” *Anal Chem 92* (10): 6925–31. https://doi.org/10.1021/acs.analchem.9b05606

Zhang, Chengqian, Peng Zhao, Wen Wen, Jun Xie, Neng Xia, and Jianzhong Fu. **2018**. “Density Measurement via Magnetic Levitation: Linear Relationship Investigation.” *Polymer Testing 12* (70):520–25. https://doi.org/10.1016/j.polymertesting.2018.08.010

Zhang, Lin, and Dihua Yu. **2019**. “Exosomes in Cancer Development, Metastasis, and Immunity.” *Biochimica et Biophysica Acta. Reviews on Cancer 1871* (2): 455. https://doi.org/10.1016/J.BBCAN.2019.04.004.

Zhang, P, M He, and Y Zeng. **2016**. “Ultrasensitive Microfluidic Analysis of Circulating Exosomes Using a Nanostructured Graphene Oxide/Polydopamine Coating.” *Lab Chip 16* (16): 3033–42. https://doi.org/10.1039/c6lc00279j.

Zhao, Pengxiang, Na Li, and Didier Astruc. **2013**. “State of the Art in Gold Nanoparticle Synthesis.” *Coordination Chemistry Reviews 257* (4): 638–65. https://doi.org/10.1016/j.ccr.2012.09.002.

Zhao, Siqi, Jingwen Huang, Dingsong Li, and Li Yang. **2022**. “Aptamer-Based Chemiluminescent Optical Fiber Immunosensor with Enhanced Signal Amplification for Ultrasensitive Detection of Tumor Biomarkers.” *Biosensors and Bioelectronics 214* (4): 114505. https://doi.org/10.1016/J.BIOS.2022.114505.

Zhao, Z, Y Yang, Y Zeng, and M He. **2016**. “A Microfluidic ExoSearch Chip for Multiplexed Exosome Detection towards Blood-Based Ovarian Cancer Diagnosis.” *Lab Chip 16* (3): 489–96. https://doi.org/10.1039/c5lc01117e.

Zhu, Jianjie, Tingting Cai, Jieqi Zhou, Wenwen Du, Yuanyuan Zeng, Ting Liu, Yulong Fu, et al. **2021**. “CD151 Drives Cancer Progression Depending on Integrin A3β1 through EGFR Signaling in Non-Small Cell Lung Cancer.” *Journal of Experimental and Clinical Cancer Research 40* (1): 192. https://doi.org/10.1186/s13046-021-01998-4

Zhu, L, K Wang, J Cui, H Liu, X Bu, H Ma, W Wang, et al. **2014**. “Label-Free Quantitative Detection of Tumor-Derived Exosomes through Surface Plasmon Resonance Imaging.” *Anal Chem 86* (17): 8857–64. https://doi.org/10.1021/ac5023056

Zhu, T, R Cheng, S A Lee, E Rajaraman, M A Eiteman, T D Querec, E R Unger, and L Mao. **2012**. “Continuous-Flow Ferrohydrodynamic Sorting of Particles and Cells in Microfluidic Devices.” *Microfluid Nanofluidics 13* (4): 645–54. https://doi.org/10.1007/s10404-012-1004-9

VITA

Alper Baran SÖZMEN

Education:

Ph.D. Bioengineering | Izmir Institute of Technology | İzmir, Türkiye - 2024

M.Sc. Chemical Engineering | Ege University | İzmir, Türkiye - 2017

B.Sc. Bioengineering | Ege University | İzmir, Türkiye – 2016

B.Sc. Chemical Engineering | Ege University | İzmir, Türkiye – 2015

Fellowships and Projects:

- Council of Higher Education 100/2000PhD Scholarship in Biotechnology (2018-2022)

- The Scientific and Technological Research Council of Turkey, Directorate of Scientist Support Program, TUBITAK-2211/A (2019-2023)

- The Scientific and Technological Research Council of Turkey, Short term Support Module, TUBITAK-1002 (Principal Investigator) (2021-2023)

- Izmir Institute of Technology, Scientific Research Project, 2020IYTE10064

Selected Publications:

- **Sözmen, A. B.** and Arslan-Yildiz, A. 2022, Sensitive and rapid protein assay via magnetic levitation, Biosensors and Bioelectronics: X, 10, 100137.
- **Sözmen A. B.**, Elveren B., Erdogan D. Mezgil B., Bastanlar Y., Yildiz U. H., and Arslan-Yildiz H. 2024, Development of chrono-spectral gold nanoparticle growth based plasmonic biosensor platform, Biosensors and Bioelectronics: X, 16, 100439,
- **Sözmen, A. B.** and Arslan-Yildiz, A. 2024, Protein quantification via LSPR-based biosensor platform utilizing chrono-growth for enhanced sensitivity, Materials Letters, 136782.
- **Sözmen, A. B.** and Arslan-Yildiz, A. 2024, Utilizing magnetic levitation to detect lung cancer-associated exosomes, ACS sensors, 9, 4, 2043—2049.